

Design and Utilization of a Top Hat Analyzer for Hall Thruster Plume Diagnostics

by

Allen Leoraj Victor

A dissertation submitted in partial fulfillment
of the requirements for the degree of
Doctor of Philosophy
(Aerospace Engineering)
in The University of Michigan
2006

Doctoral Committee:

Arthur F. Thurnau Professor Alec D. Gallimore, Co-Chair
Professor Thomas H. Zurbuchen, Co-Chair
Professor Brian E. Gilchrist
Assistant Professor Patrick L. Koehn, Eastern Michigan University

“If I have seen further, it is by standing on the shoulders of giants.”

- Isaac Newton, Letter to Robert Hooke, February 5, 1675

© Allen Leoraj Victor

All Rights Reserved
2006

DEDICATION

To my parents whose unconditional encouragement, love, and support for the pursuit of my dreams were essential for the completion of this thesis.

ACKNOWLEDGMENTS

If monkeys were the size of atoms, and we were to fill the entire observable universe up with them randomly typing at atomic typewriters, it is likely that only the first twelve words of this thesis would have been typed even if they had started since the dawn of time. This leads me to the conclusion that this thesis is more than a collection of random characters typed out by monkeys.¹

On the other hand, if I had been charged to write this thesis from inside a cage without the guidance of my advisors, help from my colleagues, or support from my family members and friends, perhaps only the first twelve words could have been written on the first page. Therefore, I can deduce that this thesis is the product of my association with a number of people, and I cannot accept the full credit of its composition.

Foremost, I would like to thank my advisors, Professor Alec Gallimore and Professor Thomas Zurbuchen for their inexhaustible assistance and encouragement in completing this project. Ever since I first saw the blue haze of an ion thruster plume at Jet Propulsion Laboratory six years ago, I dreamed of contributing to humanity's exploration of the planets through the research and development of propulsion systems for spacecraft. I believe that Professor Gallimore saw this dream and took me under his wing, not

¹ For an example of what my thesis might have looked like if monkeys had been given the opportunity to write it, visit: <http://www.vivaria.net/experiments/notes/publication/>

because I was capable of completing a Ph.D., but because he saw the opportunity of fostering my first (and possibly most important) step in achieving my lifetime goals. For this, I am truly thankful for his patience and commitment to seeing me through the journey of graduate school.

I grant a large portion of credit to one person for the conception of my thesis topic, Professor Thomas Zurbuchen. From my first summer in Ann Arbor of trying to understand how a top hat analyzer works, to the design, fabrication, characterization, and testing of the instrument, Professor Zurbuchen laid down the bridge for me to cross many obstacles encountered along my journey. I am humbled by his expertise in space plasma diagnostics, and I am grateful for allowing me to introduce this technology into the electric propulsion community.

Professor Patrick Koehn was the witness to the most exciting moment of research in the testing of my instrument – the first detection of an ion in his lab – demonstrating the instrument’s successful operation. The many hours of help in and outside of the Mass Spectrometry Laboratory allowed Professor Koehn to be privy to this landmark achievement in my research. I am happy to have shared it with him.

I am also happy to have included Professor Brian Gilchrist on my thesis committee for a fresh perspective of my thesis work.

Another scientist who has been *instrumental* in the design and testing of TOPAZ is Robert Lundgren. I thank him for his many hours of explaining how to run computational simulations in SIMION and diagnose problems that arose during the instrument’s testing. Charles Navarre and Robb Gillespie did an outstanding job maintaining the tolerances required to fabricate TOPAZ, and Dr. Stefan Scherer’s lease

of the ion accelerator and vacuum chamber were vital for the instrument's characterization.

Outside of the technical assistance I received, the staff and administration at the University of Michigan's Department of Aerospace Engineering provided me with a compass to navigate the sea of higher education. Special thanks go to Margaret Fillion for her extremely calm and friendly nature when handling administrative situations such as a missed paycheck or a form that needed to be signed. Denise Phelps has also held my hand through the formalities of submitting this thesis document.

It has been an honor to have associated with the brightest graduate students in the country who have matriculated and graduated from the Plasmadynamics and Electric Propulsion Laboratory (PEPL). Thanks to the alumni who were always available to share their experiences and knowledge of electric propulsion devices: Dr. Timothy Smith, Dr. Richard Hofer, Dr. Brian Beal, Dr. Mitchell Walker, Dr. Daniel Herman, and Dr. Joshua Rovey. And thanks go to the current PEPL members who I have worked with many hours in the vacuum chamber and look forward to seeing in the electric propulsion community: Jesse Linnell, David Kirtley, Kristina Lemmer, Robert Lobbia, Daniel Brown, Thomas Liu, Bryan Reid, Bailo Ngom, Sonca Nguyen, and Rohit Shastry.

Last but not least, I would like to thank my family, for it is their love and support which have provided the fuel to complete my journey. Thank you Dalton Victor for being a role model and making engineering, physics, and math interesting to me. Thank you, Andrew Victor for being my inspiration in striving to be a unique individual who could achieve my goals. My parents provided me with the drive and determination to achieve

my best for the past 27 years. I hope the completion of this thesis can partially make up for the past 5 years, for which I have been 2,360 miles away from my family.

If you, the reader, have made it this far, I am thankful you have decided to take a look at my research.

Allen L. Victor
January 2006

TABLE OF CONTENTS

DEDICATION.....	ii
ACKNOWLEDGEMENTS	iii
LIST OF FIGURES	xi
LIST OF TABLES	xvi
LIST OF SYMBOLS	xvii
ABSTRACT.....	xxi
CHAPTER 1: INTRODUCTION.....	1
1.1 Spacecraft Propulsion Concepts	1
1.1.1 Specific Impulse.....	3
1.1.2 Methods of Propulsion.....	4
1.2 Electric Propulsion Overview	7
1.2.1 Power Supply Considerations	9
1.3 The Three Flavors of Electric Propulsion.....	11
1.3.1 Electrothermal Propulsion	12
1.3.2 Electromagnetic Propulsion	14
1.3.3 Electrostatic Propulsion	17
1.3.4 A Summary of Electric Propulsion Systems.....	24
1.4 The Importance of Plasma Thruster Plume Diagnostics	26
1.4.1 Inference of Thruster Performance via Plume Properties.....	27
1.4.2 Plume Impingement on Spacecraft Components.....	27
1.5 The Future of Hall Thruster Design.....	28
1.5.1 A Historical Perspective	29
1.5.2 Recent Trends in Hall thruster and Ion Engine Design	30
1.6 Research Aim and Contribution	30
1.6.1 The Top Hat Analyzer	30
1.6.2 Motivation for a Top Hat Analyzer for Plume Diagnostics.....	32
1.6.3 Focus of Research	33
1.7 Thesis Roadmap.....	34
CHAPTER 2: PLUME DIAGNOSTICS AND THE TOP HAT ANALYZER.....	36

2.1 The Drive for Plume Characterization.....	36
2.2 A Survey of Plume Diagnostics Instruments.....	37
2.2.1 Direct-Contact Probes.....	37
2.2.2 Remote Sensing Techniques.....	40
2.2.3 Particle Filtering Techniques.....	41
2.2.4 A Summary of Plume Diagnostics Instruments.....	47
2.3 Top Hat Analyzer Capabilities.....	49
2.3.1 The Evolution of the Top Hat Analyzer.....	49
2.4 Summary.....	51
CHAPTER 3: DESIGN AND THEORETICAL CHARACTERIZATION OF	
TOPAZ.....	52
3.1 Design Requirements.....	52
3.1.1 Energy Range Requirements.....	53
3.1.2 Angular Resolution Requirements.....	54
3.1.3 Plasma Property Considerations.....	54
3.1.4 Arcing Considerations.....	56
3.1.5 Summary of Design Requirements.....	57
3.2 Theory of Operation.....	58
3.2.1 Analyzer Constant.....	60
3.2.2 Guiding Plate Design.....	61
3.2.3 Aperture Size.....	62
3.2.4 Geometric Factor.....	63
3.3 Design of TOPAZ through SIMION.....	65
3.3.1 Description of the Model.....	65
3.3.2 Energy Resolution.....	66
3.3.3 Top Hat Design.....	69
3.3.4 Guiding Plate Design.....	72
3.3.5 Grounded Cover Plate and Outer Shell.....	72
3.3.6 Summary of Physical Characteristics of TOPAZ.....	73
3.4 Pro/ENGINEER Model of TOPAZ.....	73
3.5 TOPAZ Performance Characterization through SIMION.....	75
3.5.1 Geometric Factor.....	76
3.5.2 Energy Correlation and Resolution.....	78
3.5.3 Elevation Angle Correlation and Resolution.....	79
3.5.4 Estimation of Azimuthal Resolution.....	84
3.5.5 Effective Collection Area.....	86
3.5.6 Footprint of Detected Ions.....	87
3.5.7 Top Hat Plate Effects.....	89
3.6 Summary of SIMION-Determined Performance Characteristics.....	92
3.6.1 Theoretical Performance of TOPAZ.....	92
3.6.2 Characterization Curves.....	93
3.6.3 Limits of SIMION.....	94
CHAPTER 4: EXPERIMENTAL CHARACTERIZATION OF TOPAZ.....	95

4.1 Construction of TOPAZ.....	96
4.2 Experimental Apparatus	97
4.2.1 Ion-Beam Accelerator System	97
4.2.2 Channel Electron Multiplier	98
4.2.3 Power Supplies.....	99
4.3 Gap Uniformity.....	99
4.4 Plate Voltage Characterization	101
4.4.1 Energy and Optimum Transmission Correlations.....	101
4.4.2 Elevation Angle Correlation	105
4.4.3 Resolution Measurements.....	107
4.4.4 Azimuthal Resolution	110
4.5 Summary of Experimental Characterization of TOPAZ	110
4.5.1 Performance Parameters	110
4.5.2 Characterization Curves.....	112
CHAPTER 5: MEASUREMENTS ON THE P5 HALL THRUSTER AND BHT-600	
CLUSTER.....	114
5.1 Measurements on the P5 Hall Thruster.....	114
5.1.1 Experimental Setup.....	115
5.1.2 Ion Detection and External Hardware.....	117
5.1.3 AFRL/UM P5 Hall Thruster	117
5.1.4 Measurements	118
5.1.5 Thermal Load on TOPAZ.....	119
5.1.6 Remachining of the Base Plate	120
5.1.7 Conclusions on the Preliminary P5 Hall Thruster Measurement.....	121
5.2 Measurements on the BHT-600 Hall Thruster Cluster.....	121
5.2.1 BHT-600 Cluster.....	122
5.2.2 Experimental Setup.....	122
5.2.3 Experimental Results and Discussion.....	124
5.2.4 Conclusions on the BHT-600 Cluster Measurements with TOPAZ.....	135
5.2.5 Conclusions on the Operation of TOPAZ with the BHT-600 Cluster.....	137
5.3 Capabilities and Improvements on TOPAZ.....	138
CHAPTER 6: THE ADDITION OF A MASS ANALYZER FOR TOPAZ	139
6.1 Mass Analyzer Selection	140
6.1.1 Quadrupole Analyzer	140
6.1.2 Magnetic Sector	140
6.1.3 Harmonic Oscillator.....	141
6.1.4 Time-of-Flight.....	142
6.1.5 Summary of Considered Techniques	143
6.2 Time-Of-Flight Principles.....	144
6.2.1 Theory of Operation.....	144
6.2.2 Pulse Length.....	145
6.2.3 Relation to the Ideal Top Hat and Mass Resolution	146
6.3 Experimental Characterization of the Mass Analyzer	148
6.3.1 Experimental Setup.....	149

6.3.2 Experimental Procedure.....	150
6.3.3 Discussion.....	158
6.3.4 Conclusions on the Time-Of-Flight Characterization of TOPAZ.....	160
6.4 Time-Of-Flight Measurements on the BHT-600 Cluster.....	162
6.4.1 Experimental Setup.....	162
6.4.2 Experimental Procedure.....	164
6.4.3 Experimental Results and Discussion.....	166
6.4.4 Conclusions on the Time-Of-Flight Measurements of the BHT-600 Cluster.....	183
6.5 Conclusions on the Operation of TOPAZ.....	184
CHAPTER 7: CONCLUSIONS.....	186
7.1 Design of the Analyzer for Plume Diagnostics.....	187
7.1.1 Choice of the Analyzer Constant.....	187
7.1.2 Choice of Materials.....	189
7.1.3 Use of the Azimuthal Angle.....	190
7.2 Measurement Capabilities.....	191
7.2.1 Energy-Angle Measurements.....	191
7.2.2 Energy-Mass Measurements.....	191
7.2.3 Mass-Angle Measurements.....	192
7.2.4 Ion Species Fractions and Velocity Distributions.....	193
7.3 Suggestions for Future Work.....	193
REFERENCES.....	195

LIST OF FIGURES

Figure 1-1: Specific impulse as a function of thrust-to-weight ratios for selected flight-proven and in-development propulsion systems. ³	6
Figure 1-2: Delta-V capability as a function of specific impulse and spacecraft propellant mass to dry mass ratio. Typical delta-V requirements are shown for impulsive missions with elliptical trajectories.....	8
Figure 1-3: The physical process of an electromagnetic accelerator utilizing electron collisions to impart energy to the propellant (adapted from Jahn ²).	15
Figure 1-4: The main components of an ion engine and the 30 cm Functional Model Thruster (FMT).	20
Figure 1-5: Schematic of a Hall thruster and a studio portrait of the NASA-173Mv1 thruster.	22
Figure 1-6: The major components and a typical ion trajectory for a top hat electrostatic analyzer.	31
Figure 1-7: Number density and energy of typical space, laboratory, and electric propulsion plasmas.....	32
Figure 2-1: A schematic and plot of the potential for the retarding potential analyzer. ⁷⁰	44
Figure 2-2: A schematic of the parallel plate analyzer. ⁷¹	46
Figure 2-3: The evolution of the geometry for the top hat analyzer. ^{72,77}	50
Figure 3-1: Energy-per-charge distribution one meter down the centerline of the P5 Hall thruster operating at 500 V 10 A. ⁸⁰	53
Figure 3-2: A cut-away view of the major components of the top hat analyzer with a typical ion trajectory.	58
Figure 3-3: Principle design parameters for a top hat analyzer.	59
Figure 3-4: A comparison of the initial and final designs of TOPAZ in SIMION.....	66

Figure 3-5: Energy Resolution as a function of the analyzer constant for multiple TOPAZ designs.....	67
Figure 3-6: A graph of the design space for TOPAZ which satisfies the design constraints.	69
Figure 3-7: Top hat region detail, and electric potential lines for a typical operating condition of TOPAZ detecting 275 eV ions from 10° below the horizontal plane. .	71
Figure 3-8: Design process (from left to right) of TOPAZ.....	74
Figure 3-9: Bottom view showing base plate detail of the Pro/ENGINEER model of TOPAZ with a quarter cut-away section.	75
Figure 3-10: Energy distribution for $V_D = -300$ V and $V_G = 0$ V. Note: x -axis has been enlarged to show distribution detail.....	79
Figure 3-11: Correlation between the average elevation angle and the normalized guiding-plate voltage for TOPAZ.....	80
Figure 3-12: Elevation angle distribution for $V_D = -300$ V and $V_G = 0$ V.	81
Figure 3-13: Elevation Angle-Energy relationship for a -300V deflection plate and grounded guiding plate setting.....	82
Figure 3-14: Average energy of detected ions as a function of the normalized guiding-plate voltage.....	83
Figure 3-15: Geometric factor as a function of the normalized guiding-plate voltage.....	84
Figure 3-16: Profile of azimuthal landing angle of detected ions for $V_D = -300$ V and $V_G = 0$ V.....	85
Figure 3-17: Entrance-positional distribution of detected ions for TOPAZ. The distribution is shown with respect to the Pro/ENGINEER model of TOPAZ (left) on the vertical plane tangent to the front surface of the instrument. The distribution is enlarged (right), and the origin of the axes is centered on the front-bottom edge of the instrument. The full-area half-maximum contour is highlighted in black.	86
Figure 3-18: Landing distribution of ions at the exit of the channel. The FAHM contour is outlined in black, and the channel centerline is shown as a dashed curve.....	88
Figure 3-19: Distribution of the z (radial) position as a function of energy for detected ions at the exit of the channel.	89
Figure 3-20: Geometric factor variation with the normalized-top hat voltage.	90
Figure 3-21: The effect of the top hat voltage (normalized) on the average elevation angle with a grounded guiding plate.....	91

Figure 4-1: Construction of TOPAZ on the Romi M17 CNC Lathe and drill press.	96
Figure 4-2: Final Construction of TOPAZ.....	97
Figure 4-3: Vacuum chamber (left) with ion-accelerator beam system (right).	98
Figure 4-4: Normalized counts versus the azimuthal angle for a 1 keV ion beam.	100
Figure 4-5: Optimum deflection plate and top hat voltages as a function of beam energy for TOPAZ.	102
Figure 4-6: Counts measured against the normalized top-hat voltage. The geometric factor plot from Figure 3-20 is normalized here for comparison.....	104
Figure 4-7: Guiding-plate test setup inside the vacuum chamber.....	105
Figure 4-8: Optimum normalized guiding-plate voltage as a function of elevation angle for a 5 keV ion beam.....	106
Figure 4-9: Energy distributions for a 3 keV deflection plate setting as compared with SIMION.	107
Figure 4-10: Elevation angle distributions for a 1 keV and 2 keV deflection plate setting as compared with SIMION.	109
Figure 5-1: Schematic of the Large Vacuum Test Facility (LVTF).	115
Figure 5-2: Location of thermocouple for the monitoring of temperature of TOPAZ... ..	116
Figure 5-3: Energy-to-charge profile measured by TOPAZ for the P5 Hall thruster operating at 300 V and 5 A.	118
Figure 5-4: Temperature of TOPAZ one meter downstream the P5 Hall thruster as a function of time.....	119
Figure 5-5: The 4×600 W BHT-600 Hall thruster cluster.	122
Figure 5-6: Setup of TOPAZ for measurements on the BHT-600 Cluster inside the LVTF. On the left, TOPAZ is moved to multiple angles with respect to the cluster, while the setup on the right, the cluster is moved with respect to the stationary TOPAZ.....	123
Figure 5-7: Energy-to-charge profile for the BHT-600 cluster along the centerline from 1 m downstream.....	125
Figure 5-8: Azimuthal profile of 275 eV ions for the top two thrusters in the BHT-600 cluster.....	126
Figure 5-9: Current as a function of azimuthal angle and energy-to-charge for the BHT-600 cluster. The color coding is exponential to enhance low current features.	128

Figure 5-10: Elevation angle and energy-to-charge relationship for the bottom-left BHT-600 thruster at a 0° cluster plume angle.....	130
Figure 5-11: Current as a function of azimuthal angle and energy-to-charge ratio for single BHT-600 thruster operation along the cluster centerline.	131
Figure 5-12: An image of 275 eV/q ions emanating from the bottom-left BHT-600 thruster. An approximate projection of the thruster dimensions (with the operating-thruster cathode) over the angles is drawn.....	134
Figure 6-1: Integration of a magnetic sector-type filter for TOPAZ.	141
Figure 6-2: Electrical schematic of controlling electronics and data system for the time-of-flight mass spectrometer for TOPAZ.....	149
Figure 6-3: Detection of ions for a varying top hat voltage with a 1 keV beam.	151
Figure 6-4: Sample voltage-time profile for a 1 keV krypton ion beam.	152
Figure 6-5: Mass-per-charge profile depicting singly- and doubly-charged krypton for various beam energies.....	154
Figure 6-6: Mass-per-charge profile depicting multiply-charged krypton ions and lighter elements for various beam energies.....	155
Figure 6-7: Mass-per-charge profile depicting singly- and doubly-charged xenon for various beam energies.....	156
Figure 6-8: Mass-per-charge profile depicting multiply-charged xenon ions.	157
Figure 6-9: Mass-per-charge profile for air displaying nitrogen and oxygen ions at various beam energies.....	158
Figure 6-10: Schematic of electrical components utilized for time-of-flight measurements in the LVTF on the BHT-600 cluster.....	163
Figure 6-11: Burle 5901 Magnum Electron Multiplier with grounded enclosure.....	164
Figure 6-12: Operation of BHT-600 cluster with TOPAZ placed one meter downstream inside the Large Vacuum Test Facility (LVTF).....	165
Figure 6-13: Energy-to-charge as a function of mass-per-charge for the cluster at a 0° plume angle.	167
Figure 6-14: Energy-to-charge as a function of mass-per-charge for the cluster at a 10° plume angle.....	168
Figure 6-15: Energy-to-charge as a function of mass-per-charge for the cluster at a 20° plume angle.....	169

Figure 6-16: Energy-to-charge as a function of mass-per-charge for the single bottom-left thruster at a 0° plume angle.	170
Figure 6-17: Energy-to-charge as a function of mass-per-charge for the single bottom-left thruster at a 10° plume angle.	171
Figure 6-18: Mass-to-charge as a function of azimuthal angle for the cluster at a 0° plume angle. The cluster is pictured for azimuthal-angle reference.	173
Figure 6-19: Mass-to-charge as a function of azimuthal angle for the cluster at a 10° plume angle. The cluster is pictured (and scaled for a 10° viewpoint) for azimuthal-angle reference.	174
Figure 6-20: Mass-to-charge as a function of azimuthal angle for the cluster at a 20° plume angle. The cluster is pictured at a 20° for azimuthal-angle reference.	176
Figure 6-21: Mass-to-charge as a function of azimuthal angle for the bottom-left thruster at 0° (left) and 10° (right) plume angles. Note: Colors are respect to individual thruster condition.	177
Figure 6-22: Guiding plate voltage as a function of mass-to-charge ratio for the cluster operation at a 10° plume angle.	178
Figure 6-23: Species fraction as a function of azimuthal angle for the cluster operation at a 0° plume angle.	179
Figure 6-24: Species fraction as a function of azimuthal angle for the cluster operation at a 10° plume angle.	180
Figure 6-25: Radial velocity distribution of Xe ⁺ , Xe ²⁺ , and Xe ³⁺ from the 0° plume angle for the cluster operating condition.	181
Figure 6-26: Axial velocity distribution of Xe ⁺ , Xe ²⁺ , and Xe ³⁺ from the 0° plume angle for the cluster operating condition.	182
Figure 7-1: Major components of an electric sector with similar capabilities as TOPAZ.	190

LIST OF TABLES

Table 1-1: Performance parameters of the major types of available electric propulsion systems. ^{3,7,18,31,34,35}	25
Table 2-1: A summary of direct contact methods for plasma thruster plume characterization.	47
Table 2-2: A summary of remote sensing methods for plasma thruster plume characterization.	48
Table 2-3: A summary of particle filtering methods for plasma thruster plume characterization.	48
Table 3-1: Plasma conditions one meter downstream the P5 Hall thruster operating at 300 V, 5.3 A. ⁸⁰	55
Table 3-2: The design parameters and requirements for TOPAZ and the motivation for each.	57
Table 3-3: Physical characteristics of the SIMION model of TOPAZ.	73
Table 3-4: Summary of SIMION-predicted performance marks as compared with the design requirements for TOPAZ.	92
Table 4-1: A comparison of the design requirements and the predicted and measured performance parameters for TOPAZ.	111
Table 6-1: Mass-Analyzer options for TOPAZ.	143

LIST OF SYMBOLS

<u>Parameter</u>	<u>Description</u>	<u>Value / Units (SI)</u>
Constants		
e	Euler's Number	(2.718282...)
e_c	Electron charge	$(1.602 \times 10^{-19} \text{ C})$
g_0	Gravitational Acceleration at Earth's Surface	(9.81 m/s^2)
k	Boltzmann Constant	$(8.617 \times 10^{-5} \text{ eV/K})$
Variables		
A	Probe Area	(m^2)
B	Magnetic Field	(T)
d	Distance Between Parallel Plates	(m)
d_{gate}	Gating Distance	(m)
d_{tof}	Time-of-Flight Distance	(m)
E	Electric Field	(V/m)
E_i	Ion Energy	(eV)
$G(E)$	"Energy" Geometric Factor	$(\text{cm}^2 \text{ sr eV/eV})$
$G(v)$	"Velocity" Geometric Factor	$(\text{cm}^2 \text{ sr})$
I	Current	(A)
I_{tot}	Total Mission Impulse	(N-s)

I_{sp}	Specific Impulse	(s)
$I_{sp,opt}$	Optimum Specific Impulse	(s)
j	Current Density	(A/m ²)
j_e	Mean Electron Current Density	(A/m ²)
K	Analyzer Constant	(-)
K_{45}	Parallel Plate Analyzer Constant	(-)
L	Distance Between Slits	(m)
m	Mass	(kg)
m_i	Ion Mass	(amu)
m_l	Payload Mass	(kg)
m_p	Total Propellant Mass	(kg)
\dot{m}_p	Propellant Mass Flow Rate	(kg/s)
m_{prop}	Loaded Propulsion System Mass	(kg)
m_{ps}	Power Supply mass	(kg)
M	Spacecraft Instantaneous Mass	(kg)
M_0	Initial Spacecraft Mass	(kg)
M_f	Final Spacecraft Mass	(kg)
n	Plasma density	(m ⁻³)
n_e	Electron density	(m ⁻³)
n_i	Ion density	(m ⁻³)
p	Momentum	(kg-m/s)
P_b	Base Pressure	(Torr)
P_c	Corrected Pressure	(Torr)

P_{chem}	Chemical Propulsion Exhaust Power	(W)
P_e	Electrical Power	(W)
P_i	Indicated Pressure	(Torr)
P_{jet}	Jet Power (Exhaust Power)	(W)
q	Charge State	(e_c)
Q_R	Heat of Combustion	(J/kg)
R_1	Inner Channel Radius	(cm)
R_2	Outer Channel Radius	(cm)
R_3	Top Hat Radius	(cm)
R_C	Channel Centerline Radius	(cm)
R_G	Guiding Plate Radius	(cm)
R_p	Particle Radius of Motion Over Aperture	(cm)
s	Aperture Radius	(cm)
t_0	Starting Mission Time	(s)
t_f	Ending Mission Time	(s)
t_{gate}	Time-of-Flight Across the Gate	(sec)
t_{TOF}	Time-of-Flight	(sec)
T	Thrust	(N)
T_e	Electron Temperature	(eV)
u_e	Exhaust Velocity	(m/s)
v	Velocity	(m/s)
V_a	Applied Potential	(V)
V_D	Deflection Plate Voltage	(V)

V_f	Floating Potential	(V)
V_{grid}	RPA Ion Retarding Grid Voltage	(V)
V_G	Guiding Plate Potential	(V)
V_p	Plasma Potential	(V)
V_{TH}	Top Hat Plate Potential	(V)
x	Horizontal Position from Centerline of Analyzer	(m)
y	Vertical Position of Ion From Base of Analyzer	(m)
z	Distance from Axis-of-Symmetry of Analyzer	(m)
α_{ps}	Specific Power Plant Mass	(W/kg)
α	Elevation Angle	(degrees)
α_{max}	Maximum Elevation Angle	(degrees)
β	Azimuthal Angle	(degrees)
β_H	Hall Parameter	(S/m)
ΔV	Delta- V , Change in Spacecraft Velocity	(km/s)
Δt	Mission Burn Time	(s)
η	Electrical to Jet Power System Efficiency	(-)
θ	Aperture Angle	(rad)
λ_D	Debye Length	(cm)
σ_e	Free Electron Conductivity	(S/m)
σ	Truncation Angle	(rad)
ϕ	Electric Potential	(V)
χ	Gate Length to Time-of-Flight Length Ratio	(d_{gate}/d_{TOF})

ABSTRACT

Electric propulsion offers new capabilities for ambitious space missions of the future. However, coating, uneven heating, and the charging of spacecraft components have impeded the integration of Hall thrusters for space missions and encouraged plume diagnostics of the thruster plasma environment. Plume diagnostics are also important for the inference of thruster performance through plume properties downstream of the engine.

While the top hat analyzer has been available for low-density space plasma diagnostics for over twenty years, the use of this instrument for plasma thruster plume diagnostics has been nonexistent. This thesis describes the development of a new diagnostics tool, the Top Hat Electric Propulsion Plume Analyzer (TOPAZ), which provides unprecedented insight into the physical mechanisms that govern the performance of Hall thrusters. Novel measurements conducted by TOPAZ on the BHT-600 Hall thruster cluster yielded interesting and undocumented phenomena in the far-field plume.

SIMION, a commercial ion optics program, was used to design TOPAZ and estimate the energy and angular resolutions as well as the instrument's sensitivity and plate-voltage relationships. TOPAZ was experimentally characterized through an ion beam facility operating on air, xenon, and krypton gases.

Measurements on the BHT-600 cluster indicated lower-energy ions emanated from positions closer to the cathode while higher-energy ions were measured from along the discharge channel centerlines. Low-energy ions were also measured from behind the cathodes only during cluster operation. Charge-exchange and ionization outside the primary acceleration region are believed to be the cause of the variance in the energy distributions. Cross pollination of the cathode plume with the opposite thruster is argued to create low-energy ions which emanate from behind the cathode.

Time-of-flight measurements through TOPAZ allowed for charge-state and species fraction discriminations as functions of emanation points from the cluster. Multiply-charged ions (~5%) were measured from regions near the discharge channels and only for plume angles less than 20 degrees. Calculations of the axial and radial velocity distributions for the first three charge-states downstream of the cluster centerline revealed a symmetric triple-peak structure in the radial velocity distributions and a double-peak profile in the axial velocity distribution of the first charge-state of xenon.

CHAPTER 1:

INTRODUCTION

In this chapter, the basic concepts of propulsion systems for spacecraft are presented. The suitability of electric propulsion systems for future ambitious space missions is discussed, and the working principles of the three types of electric propulsion systems are described. The need for ground-testing and diagnostics tools for electric propulsion systems is then presented, and recent trends in Hall thruster development are described. The top hat analyzer, a type of electrostatic analyzer utilized for space plasma diagnostics, is proposed for plume characterization of high-power/high-specific impulse Hall thrusters being developed for ambitious missions of the future.

1.1 Spacecraft Propulsion Concepts

Spacecraft and artificial satellites require a means of acceleration to travel from Earth's surface to a desired trajectory or orbit. Propulsion systems are designed to create a change in velocity, ΔV (delta-V), of the spacecraft to achieve this goal. Rocket engines, for example, generate this force by accelerating exhaust gasses in the opposite direction of the desired delta-V. Newton's third law of motion states: "All forces occur in pairs, and these two forces are equal in magnitude and opposite in direction."¹ The forces exerted on the propellant are coupled with the force applied to the spacecraft in the opposite direction.

Newton's third law of motion is a specific case for the conservation of linear momentum within a closed system. Momentum, \vec{p} , is defined as the product of the mass, m , and velocity, \vec{v} , of an object:

$$\vec{p} = m\vec{v} \quad \text{Eqn. 1-1}$$

A spacecraft's flight can be described by applying Newton's second law: "An applied force is equal to the rate of change of momentum." In the absence of any external forces (e.g., gravity and atmospheric drag), the thrust imparted on the spacecraft is directly proportional to the rate of change of spacecraft mass and the exhaust velocity of the propellant with respect to the spacecraft, \vec{u}_e . The propellant flow rate, \dot{m}_p , is equivalent to the rate of change of spacecraft mass and defined to be positive in value. Equation 1-2 displays the simple relationship between propellant flow rate, exhaust velocity, and thrust \vec{T} :

$$\vec{T} = -\dot{m}_p \vec{u}_e \quad \text{Eqn. 1-2}$$

The exhaust velocity of the propellant must be in the opposite direction to yield a positive thrust in the desired direction. Integration over the lifetime (from time t_0 to t_f) of a mission yields the total impulse \vec{I}_{tot} :

$$\vec{I}_{tot} = \int_{t_0}^{t_f} \vec{T} dt \quad \text{Eqn. 1-3}$$

Equations 1-2 and 1-3 prove that a maximized product of propellant flow rate and exhaust velocity results in a maximum of the total impulse for a mission. Since increasing the propellant flow rate requires more propellant and hence a higher initial propellant mass, it is desirable to increase the exhaust velocity instead.

In the absence of external forces on the spacecraft (e.g., atmospheric drag and gravitational force), the change in spacecraft mass can be determined for a given ΔV requirement and exhaust velocity of propellant. The thrust is directly proportional to the product of the spacecraft's instantaneous mass, M , and rate of change of velocity (i.e., acceleration) via Newton's second law. Rewriting the relationship in differential form with scalar values yields the following:

$$Mdv = u_e dM \quad \text{Eqn. 1-4}$$

Through separation of variables, Eqn. 1-4 is easily integrated from the initial to the final spacecraft conditions to yield Tsiolkovsky's celebrated rocket equation:

$$\frac{M_f}{M_0} = e^{\frac{-\Delta V}{u_e}} \quad \text{Eqn. 1-5}$$

The initial and final masses of the spacecraft are represented with M_0 and M_f , respectively. As the delta-V of a maneuver or mission increases, the spacecraft final mass must be a smaller fraction than the initial mass. This is equivalent to stating that the propellant mass becomes a larger fraction of the spacecraft's initial mass, as the delta-V requirement increases. The propellant exhaust velocity dictates the fuel required for the maneuver. The exhaust velocity for a spacecraft must be a significant fraction of the total ΔV mission requirement, if a significant fraction of the spacecraft's original mass is to be brought to the final velocity.²

1.1.1 Specific Impulse

The measure of the total impulse produced from a unit weight of propellant by a spacecraft engine is the specific impulse I_{sp} . This performance factor can be used to compare spacecraft engines; in a similar fashion "miles-per-gallons" are used to compare

automobiles. However, it is the *change* (in either direction or speed), and not the maintenance, of velocity that requires propellant usage in the absence of external forces on the spacecraft. The formal definition for the specific impulse is a time-average to account for varying rocket thrust and propellant flow rates.³

$$I_{sp} = \frac{\int_{t_0}^{t_f} T dt}{g_0 \int_{t_0}^{t_f} \dot{m} dt} \quad \text{Eqn. 1-6}$$

The specific impulse is simply the total impulse produced divided by the total weight of propellant consumed where g_0 is the Earth acceleration of gravity at sea level (9.8066 m/s²). In physical terms, and as an example, a specific impulse of 350 seconds equates to levitating the initial mass of propellant for 350 seconds. For example, one kilogram of propellant with a specific impulse of 350 seconds provides enough impulse to levitate one kilogram of mass for almost 6 minutes. For constant exhaust velocity systems, the specific impulse is simply the product of the exit velocity and the constant g_0 .

1.1.2 Methods of Propulsion

Many techniques are available to store and retrieve the energy required to accelerate propellant away from the spacecraft to generate thrust. Currently operating spacecraft include cold gas, chemical, and electric propulsion (EP) engines. Exotic methods of propulsion in development include utilizing nuclear fission or fusion power and matter-antimatter reactions to provide thrust. Propellantless types of spacecraft propulsion systems are being developed as well. This includes, but is not limited to, solar

sail (utilizing solar pressure),⁴ beamed energy,⁵ and space tether⁶ methods. These spacecraft propulsion techniques are beyond the scope of this thesis.

Cold gas propulsion systems simply store energy through highly pressurized gas, which is expanded through a nozzle to generate thrust. In chemical rockets, propellant particles are thermally excited through combustion and excreted through a nozzle which converts a majority of the particle's thermal energy into kinetic energy. Chemical rockets are typically divided into three basic categories: liquid, solid, and hybrid.⁷ Electric propulsion (EP) devices use externally provided electric power to accelerate the propellant to produce thrust. EP systems are generally classified into three categories: electrothermal, electromagnetic, and electrostatic propulsion.

Another important performance parameter for spacecraft propulsion systems is the thrust-to-weight ratio. This is defined as the ratio of thrust force and full propulsion sea level weight (with propellants, but without payload). The thrust-to-weight ratio is equivalent to the acceleration provided by the propulsion system on its own mass in multiples of earth's gravitational acceleration at sea level (i.e., the number of g_0 's). Figure 1-1 describes the specific impulse and thrust-to-weight ratio ranges for several propulsion systems. Electric propulsion systems are shown in blue, and chemical systems are shown in pink.

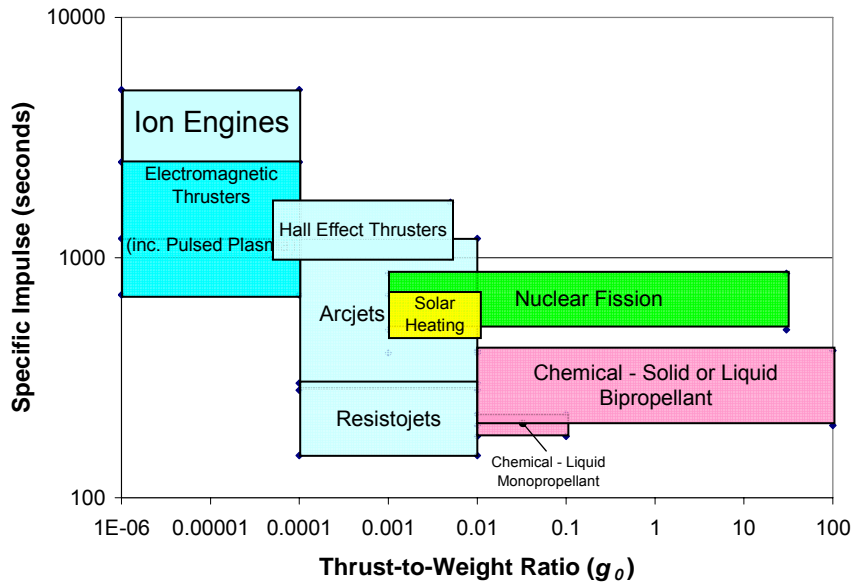


Figure 1-1: Specific impulse as a function of thrust-to-weight ratios for selected flight-proven and in-development propulsion systems.³

A general trend is noticed for propulsion systems – an inverse relationship exists between the specific impulse capability and the thrust-to-weight ratio. Electric propulsion systems tend to offer a high specific impulse with a low thrust-to-weight ratio. On the other hand, chemical systems offer high thrust-to-weight ratios but lack high specific impulses. Several propulsion systems in development, such as nuclear fission devices, are attempting to offer high specific impulses, while providing significant thrust-to-weight ratios; however, prohibitive power requirements and efficient energy conversion present a significant barrier for the near-term development of these types of engines for ambitious deep space and manned missions of the future.

The product of specific impulse and thrust-to-weight ratio reveals another important performance parameter for spacecraft propulsion engines – the specific power. This is equivalent to the jet power (or exhaust power), P_{jet} , divided by the loaded propulsion system mass, m_{prop} .

$$\frac{P_{jet}}{m_{prop}} = \frac{1}{2} (I_{sp}) \left(\frac{T}{m_{prop} g_0} \right) \quad \text{Eqn. 1-7}$$

Two types of energy conversion processes occur for any propulsion system, the generation (or retrieval) of stored energy and its conversion into reaction thrust. The jet power is the rate of expenditure of propulsion energy. For chemical propulsion systems, this energy is released from chemical bonds through the combustion process. The maximum jet power for these engines is therefore fundamentally limited by the heat of combustion reaction Q_R released per chemical reaction to products:

$$P_{chem} = \dot{m} Q_R \quad \text{Eqn. 1-8}$$

For electric and nuclear propulsion systems, the energy transmitted to exhaust particles is not restricted by heat of reaction through combustion. Electric propulsion systems utilize an external power supply which is then converted into exhaust power. This allows for a much higher kinetic energy to be inputted into each propellant exhaust particle, and therefore, the exhaust velocity is not limited by the chemical bond energy as in chemical propulsion systems. The remainder of this thesis will concern electric propulsion systems and their diagnostics.

1.2 Electric Propulsion Overview

The first unpublished conception of utilizing electrical power for propulsion is credited to Robert Goddard on September 6th, 1906, through an inscription in his notebook of his thoughts on the acceleration of electrons through an electrostatic field.⁸ The enormous velocities achieved with these particles inside cathode ray tubes, hinted towards the prospect of designing a highly efficient propulsion system. High propellant-exhaust velocities (and hence specific impulses) are the defining characteristic of electric

propulsion systems. The importance of specific impulse is illustrated via the rocket equation in Figure 1-2.

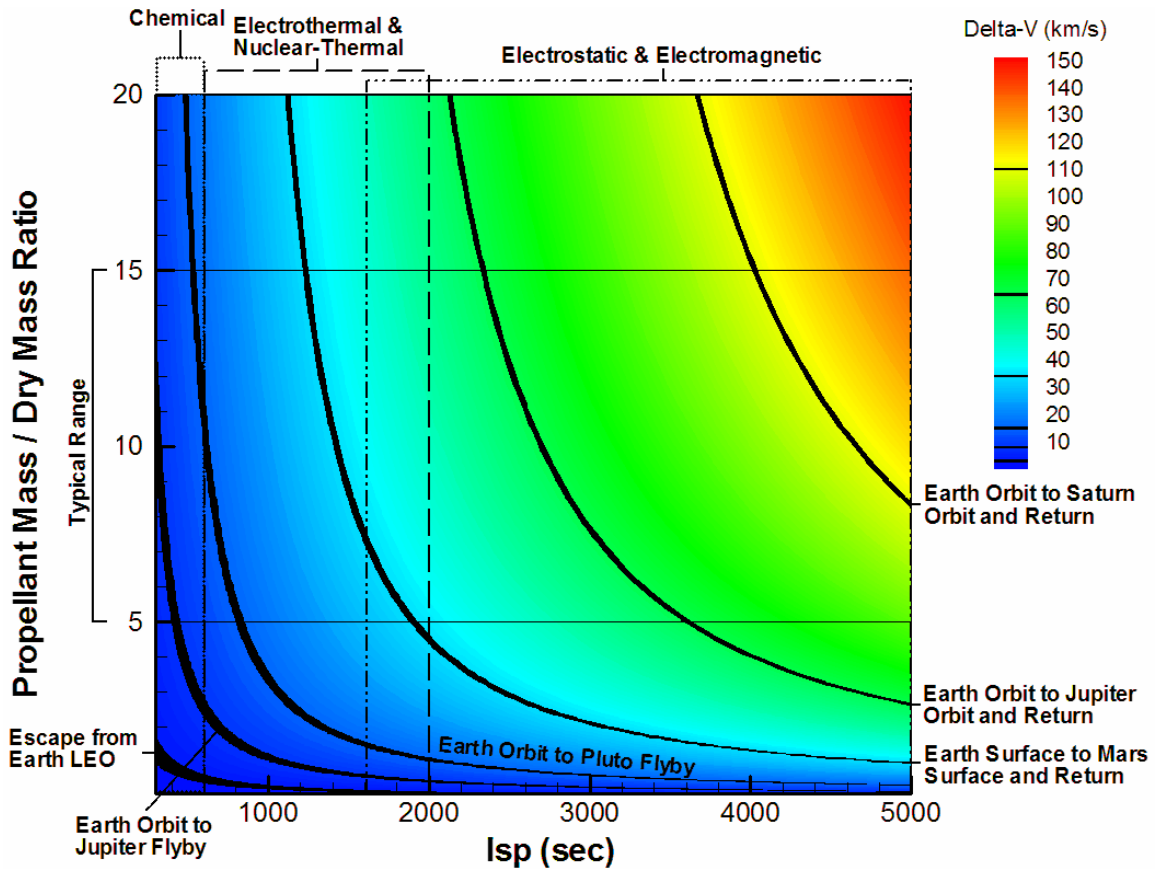


Figure 1-2: Delta-V capability as a function of specific impulse and spacecraft propellant mass to dry mass ratio. Typical delta-V requirements are shown for impulsive missions with elliptical trajectories.

Typical propellant-mass to dry-mass ratio are on the order of 10, and range from 5 to 15. This ratio is the fuel mass in terms of the payload and structure mass (the dry mass of the spacecraft, i.e., everything but the fuel). For higher specific impulses, higher delta-V capability exists for the same propellant-mass to dry-mass ratio. Chemical propulsion systems generally have specific impulses below 450 seconds, however the theoretical possibility of these systems having I_{sp} 's up to 700 seconds and higher is being investigated.⁹ Electric propulsion systems have specific impulse limits approximately an

order of magnitude higher. This allows for more ambitious mission capability, explaining the currently highly-active research being conducted in the field. Missions, such as sample returns from the outer planets, require either highly efficient propulsion systems or uniquely-tailored gravity assist trajectories coupled with auspicious planetary alignment.

1.2.1 Power Supply Considerations

Since the electrical input power for EP systems is not limited by the heat of combustion reaction, the output jet power capability is high; however, practical upper limits exist due to power supply considerations. The electrical energy which is to be converted into thrust energy must be provided by a power supply. The power supply mass increases with higher current and voltage requirements which are required for higher specific impulse EP devices. As the specific impulse is increased, the power supply mass eventually curtails the overall mass savings generated with a more fuel-efficient propulsion system. This generates an optimum specific impulse for which the mass of the propulsion system is minimized.

A power supply's output can be expressed in terms of the output electrical power P_e per unit mass of the power supply m_{ps} :

$$\alpha_{ps} = \frac{P_e}{m_{ps}} \quad \text{Eqn. 1-9}$$

The ratio α is known as the specific power plant mass. Ideally, a very high specific power plant mass is desired, however, this is often an unalterable design specification based on the required power output and current power processing unit

(PPU) and power supply design technology. The system efficiency η of the conversion of electrical power to jet power is defined by the ratio of the two:

$$\eta = \frac{P_{jet}}{P_e} \quad \text{Eqn. 1-10}$$

The mass of the power system m_{ps} can be represented in terms of the specific impulse, the specific power plant mass, the propellant flow rate \dot{m} , and the system efficiency.

$$m_{ps} = \frac{\dot{m}_p (I_{sp} g_0)^2}{2\alpha_{ps}\eta} \quad \text{Eqn. 1-11}$$

By breaking down a spacecraft's total mass M_0 into the payload mass m_l , propellant mass, and power supply mass, the effect of the power supply mass can be determined on the rest of the spacecraft.

$$M_0 = m_l + m_p + m_{ps} \quad \text{Eqn. 1-12}$$

By rewriting equation 1-10 with utilization of the rocket equation and equation 1-11, the effect of specific impulse on the total spacecraft mass is deduced. The relationship is normalized by the payload mass m_l .

$$\frac{M_0}{m_l} = 1 + \frac{\dot{m}_p (I_{sp} g_0)^2}{2\alpha_{ps}\eta m_l} + e^{-\left(\frac{\Delta V}{I_{sp} g}\right)} \quad \text{Eqn. 1-13}$$

The second term on the right hand side of the equation describes the increasing power supply mass penalty for higher specific impulses. The last term corresponds with the propellant mass which decreases for higher specific impulses. Therefore, a balance for these opposing mass contributors exists, such that a minimum initial total mass is

reached when the optimum specific impulse is chosen. This specific impulse is related to the total mission burn time Δt , the specific power plant mass, and the system efficiency:¹⁰

$$I_{sp,opt} = \frac{1}{g_0} \sqrt{\frac{2\eta\Delta t}{\alpha_{ps}}} \quad \text{Eqn. 1-14}$$

Although the previous analysis assumes constant spacecraft parameters, the existence of an optimum specific impulse is attributed to the correlation between the mass of the power supply and the output power. The specific impulse should be maximized to have the most fuel efficient system. However, the power supply mass prevents the fuel savings from minimizing the overall system mass, and an optimum specific impulse is reached with a balance of the competing factors. The issue becomes more complicated when parameters are allowed to vary, and other factors such as the trajectory, overall mission length, and gravity-assist capability is added. Solar arrays can also be utilized to provide electrical power to the propulsion system as well; however, for deep space missions (i.e., missions to and beyond Jupiter) the solar energy output is prohibitively low. The optimization problem of maximizing payload fractions is currently an active field of research.¹¹

1.3 The Three Flavors of Electric Propulsion

A definition of electric propulsion provided by Jahn is “the acceleration of gases for propulsion by electrical heating and/or by electrical and magnetic body forces.”² This definition is usually subdivided into three categories: electrothermal, electromagnetic, and electrostatic propulsion. Each of these methods of propulsion is capable of providing significantly higher specific impulses than chemical rockets. The three subdivisions arise

from the intermediate medium of energy storage between electrical energy and the directed kinetic energy (resulting in thrust).

In electrothermal propulsion systems, heat energy is converted into kinetic energy. For electromagnetic systems, energy is stored in a combination of electric and magnetic potential energy. Electrostatic propulsion utilizes primarily static electric fields to store potential energy which is converted into thrust energy. Magnetic fields can be utilized to increase efficiency in electrostatic propulsion systems, resulting in a somewhat amorphous boundary between electrostatic and electromagnetic categorization for some propulsion systems. A description of each type of system is presented, which leads to the impetus for electric propulsion plume diagnostics and specifically the need to create diagnostic tools which follow the trends of EP thruster design.

1.3.1 Electrothermal Propulsion

Electrothermal propulsion systems are possibly the simplest electric propulsion systems to fabricate and utilize. These propulsion systems utilize heat energy as the intermediary form of energy storage before it is converted to directed-kinetic energy. Currently, two types of electrothermal propulsion systems exist today: the resistojet and the arcjet. The resistojet converts electrical energy into heat energy. High electrical resistance dissipates power which is conducted to the propellant mostly through convection. Arcjets flow current directly through the propellant through an arc discharge (i.e., an electrical spark).

1.3.1.1 Resistojets

The resistojet is considered the simplest electric propulsion system in terms of operating principles. Propellant flows over an ohmically heated surface, and heat energy is conducted to the propellant through convection. The thermal energy is converted into thrust through a nozzle. The maximum specific impulse is usually limited to about 300 seconds due to operating temperature constraints on the material. Hydrogen provides the highest specific impulse, since the molecular weight of the propellant is lowest. The velocities for a given temperature are maximized for the lowest weight propellant. Although resistojets do not provide the high-specific impulses that other EP systems can deliver, they offer simplicity and virtually any propellant choice is appropriate.³ Hydrazine, for example, is a common choice for resistojets, since it is easy to store and handle, and the propellant can be used for the attitude and control system (ACS) of the spacecraft as well.

Resistojets have been considered for a wide variety of missions. Since resistojets have a wide propellant capability, manned spacecraft missions with human waste products (e.g., water and carbon dioxide) could be utilized as propellant.¹² Several missions, including the Iridium spacecraft, Intelsat V, and GOMS satellites, have recently employed resistojets. Resistojets provide a high thrust-to-weight ratio, and therefore thrusting times are low as compared to other EP systems. Therefore, resistojets are an excellent choice for missions with low to modest delta-V requirements but rely on thruster “burn” times, power limits, and plume effects as mission drivers.³

1.3.1.2 Arcjets

As with the resistojet, arcjets thermally heat propellant which is then expanded through a nozzle. However the method of heating is through an electrical discharge between a cathode and an anode. The electric arc can heat propellant to approximately 15,000 K.³ The hot gas is expanded through a nozzle. Since the propellant temperatures are much higher for arcjets, they tend to have much higher specific impulses.

Several propellants have been utilized for arcjets including nitrogen, helium, hydrogen, neon, hydrazine, and argon.³ Specific impulses for hydrogen range from 1200 to 1500 seconds. Most arcjets, however, have low efficiencies at around 30-40%. The largest loss is due to residual internal energy and ionization costs. The low efficiency results in a significant decrease of thrust-to-power ratio when compared to resistojets. However, arcjets benefit from scalability into large thrust levels as compared with other EP systems. Arcjets are also relatively simple to integrate, and are the least costly of any plasma propulsion device.⁷

Several satellites have incorporated arcjets for north-south station-keeping (NSSK), east-west station-keeping and orbit relocation. As of 2004, Lockheed Martin had a total of 24 operational spacecraft utilizing arcjets. Aerojet sells arcjet systems internationally, with successful flights on the MR-509 and Japanese DRTS spacecraft systems.¹³

1.3.2 Electromagnetic Propulsion

Electromagnetic propulsion systems incorporate a magnetic field (either self-induced or externally applied) to accelerate ionized gas flows to produce thrust. In general, these types of propulsion systems are the most phenomenologically complex and

utilize a combination of electrostatic and magnetic fields. Electromagnetic acceleration is illustrated through a generalized Ohm's law¹⁴ for free electrons:

$$\vec{j}_e = \sigma \left(\vec{E} + \vec{v} \times \vec{B} - \left(\frac{\beta_H}{\sigma B} \right) (\vec{j}_e \times \vec{B}) \right) \quad \text{Eqn. 1-15}$$

The electric field is represented by \vec{E} and the magnetic field by \vec{B} . The current density \vec{j} is induced by the combination of these two fields in a plasma flowing with velocity \vec{v} with a free electron conductivity σ and a mean electron current density \vec{j}_e . The Hall parameter β_H represents the degree of momentum transmitted from electrons to the heavy particles (propellant) through collisions or microscopic polarization fields. The third term on the right hand side of Equation 1-15 describes the loss in electron current due to momentum-exchange collisions with the heavy propellant particles producing thrust. Figure 1-3 describes the directions of the electric and magnetic fields inside a simple electromagnetic thruster.

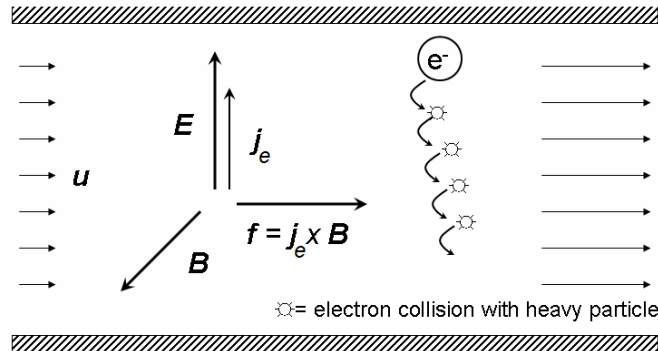


Figure 1-3: The physical process of an electromagnetic accelerator utilizing electron collisions to impart energy to the propellant (adapted from Jahn²).

In the above example, the combination of electric and magnetic fields is used to transfer kinetic energy to the propellant particles. The two main types of electromagnetic thrusters are magnetoplasmadynamic (MPD) and pulsed-plasma thrusters (PPT). MPD

thrusters utilize a steady flow, whereas the PPT incorporates an unsteady electromagnetic acceleration. A brief description of each of these thrusters is presented followed by discussion of the final type of electric propulsion systems, electrostatic propulsion.

1.3.2.1 Magnetoplasmadynamic (MPD) Arcjet Thrusters

MPD arcjets, also known as Lorentz Force Accelerators, come in two flavors: applied-field and self-field thrusters. Applied-field MPD thrusters utilize either permanent or electromagnets surrounding the exhaust chamber to help stabilize and accelerate the plasma discharge. Self-field MPD thrusters contain a cathode which extends through the middle of the chamber. A radial discharge from the cathode produces an azimuthal magnetic field, which interacts with flowing plasma to generate thrust in the axial (thrusting) direction. For low power levels, self-field MPD thrusters are unable to produce the required magnetic field, and the applied-field configuration is necessary.

MPD thrusters theoretically have the highest specific impulse *and* thrust capability; however, due to their extreme power requirements (on the order of megawatts) and the degradation of the cathode surface, they have never been used as a primary propulsion system. In a Japanese MPD test in 1996, the EPEX (Electric Propulsion EXperiment), an MPD arcjet was tested successfully on the STS-72 shuttle mission.¹⁵

1.3.2.2 Pulsed Plasma Thrusters (PPT)

While MPD electromagnetic thrusters have a large thrust capability, pulsed plasma thrusters (PPTs) are proficient at providing minute amounts of thrust, and are therefore excellent for station-keeping and other small delta-V maneuvers. PPTs were the

first type of electric propulsion systems to be flown in space by the Russians on the Zond-2 and Zond-3 spacecraft in 1964 and 1965, respectively.¹⁶

PPTs utilize a self-induced magnetic field and a plasma arc to accelerate propellant gas along parallel anode and cathode rails. Teflon is generally the propellant of choice, as it is suitable for space storage, easy to handle, and ablates with insignificant charring.³ A Teflon bar is pushed between the rails, and the Teflon is ablated by rechargeable capacitor discharges across the surface. The ionized vapor is accelerated down the rails due to the combination of the electric field between the anode and cathode and an orthogonal self-induced magnetic field generated from the current between the rails.

PPTs generally have low efficiencies (<10%) due to energy loss in capacitor resistance, ablation, dissociation, ionization, and plasma and electrode heating. However, these thrusters are well suited for fulfilling small delta-V maneuvers (such as NSSK) and, as recently demonstrated on the EO-1 spacecraft,¹⁷ attitude control requirements on small spacecraft with a surplus of electric energy.

1.3.3 Electrostatic Propulsion

The third type of electric thruster is electrostatic propulsion. Electrostatic thrusters convert electric potential energy stored in the propellant to kinetic energy to generate thrust. In general, these thrusters ionize propellant, accelerate the ions created, and neutralize the exhaust plume. Field emission electric propulsion (FEED), colloid

thrusters, ion thrusters², and Hall effect thrusters (HETs or just Hall thrusters) are electrostatic thrusters. Ion and Hall thrusters are currently being developed for a wide-variety of missions from north-south station-keeping to primary propulsion systems for ambitious deep-space applications.

Efforts to scale both Hall thrusters and ion engines into the upper and lower ends of the power and size spectrums are active areas of research in the electric propulsion community. Particularly, the interaction of the plume from engines with high specific impulse and power levels with spacecraft components is a primary concern for thruster integration.

Each of the types of electrostatic ion propulsion systems will be described with emphasis on Hall thrusters. The trend in Hall thruster research and issues of their integration with spacecraft systems is then described leading to the impetus of the contribution to research for this thesis.

1.3.3.1 Field emission electric propulsion (FEEP)

FEEP thrusters utilize a liquid metal as propellant (such as indium or cesium) and draw ions from the liquid surface through a slit by use of a strong electric field (10^3 kV/mm). Atoms are spontaneously ionized at the surface and an ion jet is extracted by the electric field.¹⁸ The ions are accelerated at high velocities to yield very high specific impulses ($> 10,000$ sec). However, the mass flow rates of these devices are very low, and

² The phrase “ion engine/thruster” can either refer to specifically electrostatic ion thrusters or plasma thrusters in general. In the context of this thesis, ion thrusters will refer to electrostatic ion thrusters only.

the overall thrust ranges from the micronewton to the millinewton range. A neutralizer balances the overall charge of the propulsion system to prevent charge build-up.

Due to the very low thrust generated, FEEP thrusters are well-suited for minute attitude control of spacecraft on drag-free missions. An indium FEEP thruster has been space-tested,¹⁹ and these types of thrusters are being considered for a wide variety of missions in the US and Europe which require ultra-precise attitude control.

1.3.3.2 Colloid Thrusters

As with FEEP thrusters, colloid thrusters draw charged particles from a fluid through use of a very strong electric field. However, instead of individual ions, tiny droplets of propellant (either positive or negative) are drawn from the surface through a capillary. The specific impulses of colloid thrusters are generally lower than FEEP thrusters (up to 3000 seconds), however, the thrust capability is significantly greater by over an order of magnitude, and they are not limited by use of metallic propellants. Colloid thrusters are relatively easily miniaturized, and are applicable for primary and attitude control propulsion systems for microsatellites.

1.3.3.3 Ion Engines

The first ion thruster was built in 1959 by Dr. Harold Kaufman,²⁰ and since then ion engines have enjoyed considerable development in the United States. Throughout the 1960s and 1970s, mercury and cesium were utilized as propellants. To reduce contamination of spacecraft and ground testing surfaces, xenon was implemented, and today it is the most widely used propellant for ion thrusters. Figure 1-4 displays a schematic of an ion thruster.

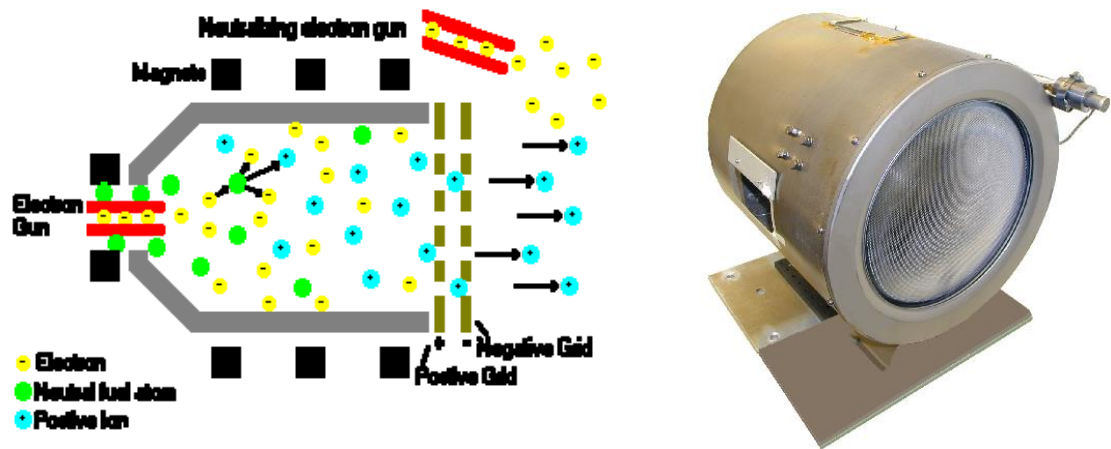


Figure 1-4: The main components of an ion engine and the 30 cm Functional Model Thruster (FMT).

An electron source, such as a hollow cathode, and propellant are fed into a chamber which is biased to a positive voltage to function as an anode. Ions are generated inside a discharge chamber through collisions of electrons and neutral propellant particles. A magnetic field increases the collision frequency of electrons with neutral propellant particles, increasing the ionization efficiency and therefore, the efficiency of the thruster. The ions are hence “born” at a high potential. The ions diffuse through the chamber and are accelerated through positively and negatively charged grids (usually two or three), which converts the stored electric potential energy into kinetic energy through columbic forces exerted by the electric field. The upstream grid (the screen grid) can be biased to several thousands of volts, while the downstream grid (the accelerator grid) is usually negatively biased to a few hundred volts with respect to the spacecraft “ground” to prevent electron back streaming from the plume. A neutralizer placed outside of the discharge chamber emits electrons to maintain charge neutrality between the propulsion system (and spacecraft) and its environment. Ion engines provide specific impulses from

1600 seconds²¹ to nearly 10,000 seconds,²² and have overall engine efficiencies ranging 50-80%. The lifetime-limiting mechanisms include discharge cathode and neutralizer failure and grid erosion and shorting.

Ion thrusters have been employed as propulsion systems for NSSK, most notably through the Boeing XIPS series of thrusters on Boeing 601/702 spacecraft, for nearly a decade. The thruster discharge chamber size for the Boeing 601 and Boeing 702 spacecraft is 13 cm and 25 cm, respectively. Recently, NSTAR, with a 30 cm discharge chamber ion engine, was utilized as the primary propulsion system for NASA's Deep Space 1 mission, rendezvousing with asteroid Braille and comet Borrelly. Wear tests on a 40 cm NEXT ion engine have been conducted at NASA Glenn Research Center.²³ This engine is being tested for possible future ambitious interplanetary missions with high delta-V requirements.

Ion engines have enjoyed possibly the most "Hollywood press" of EP devices, being featured as part of the Twin Ion Engine (TIE) Fighter propulsion system in the Star Wars series of movies.

The main competitor for propulsion systems requiring specific impulses between 2000-4000 seconds is the Hall thruster.

1.3.3.4 Hall thrusters (HETs)

The Hall thrusters similarly apply an electrostatic field downstream of the anode where the propellant is injected and ionized to produce thrust. However, the geometry, ionization scheme, and electric field generation differs from the ion engine. Figure 1-5 displays the working principles of the Hall thruster and the NASA-173Mv1 thruster.

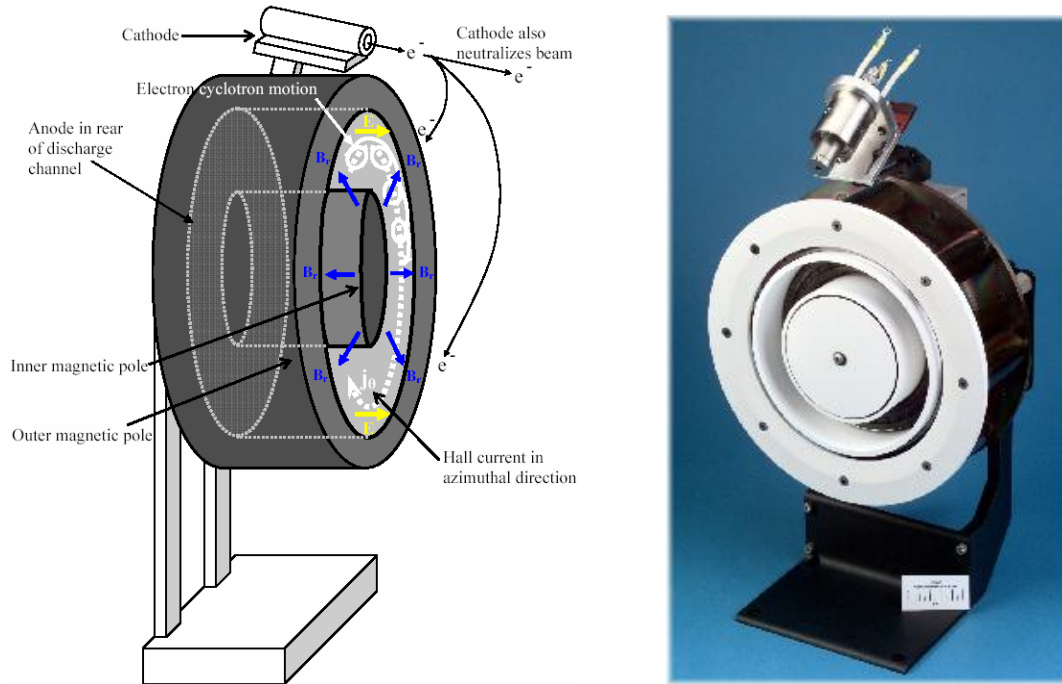


Figure 1-5: Schematic of a Hall thruster and a studio portrait of the NASA-173Mv1 thruster.

Most Hall thrusters have an annular geometry, however, racetrack, linear, and cylindrical geometries have been also tested.²⁴⁻²⁶ Propellant is ejected from an annular plate, which acts as a gas distributor, through holes or slits evenly spaced azimuthally throughout the annulus. The neutral propellant particles diffuse downstream towards the discharge channel exit. Ionization arises from collisions between electrons and propellant particles. The plate is biased to a large positive voltage to function as the anode for the thruster. A hollow cathode produces electrons outside the discharge channel for which a majority migrate towards the positively-charged anode. Some of the electrons neutralize the plume and prevent charge build-up, similar in function to the neutralizer on the ion engine.

The “Hall effect” portion of the thruster arises from radial magnetic fields which are generated by solenoids placed on the exterior of the annulus. Ferromagnetic pole

pieces guide the magnetic field lines in the radial direction. The magnetic field strength is set such that the electrons experience an $\mathbf{E} \times \mathbf{B}$ drift, while the effect on ions is negligible. This is due to the mass dependence of a magnetic field's force on a charged particle - propellant ions are generally over a hundred thousand times more massive than the light electrons.

The electrons are guided in the azimuthal direction around the annular discharge channel by the combination of the electric field and applied magnetic field. This is called the Hall current, from which the propulsion system derives its name. The electron current through the discharge channel induces a lower potential near the channel exit due to the high density of negatively charged particles. The ions are accelerated away from anode and through the lower-potential "virtual grid" of electrons to produce thrust, hence, Hall thrusters are sometimes referred to as gridless ion thrusters. The electrons slowly migrate towards and are collected by the anode through collisions (which ionize the propellant) and plasma turbulence. Although Hall thrusters utilize a magnetic field for operation, they are still considered electrostatic ion thrusters, since the magnetic field is not directly involved in the thrust producing mechanism.

Since the majority electron motion is kept within the thruster confines, the Hall thruster is often referred to as a closed drift thruster (CDT). Two types of Hall thrusters have been developed, the anode layer thruster (TAL) and the stationary plasma thruster (SPT or magnetic layer thruster). The TAL utilizes short metallic discharge channel walls (e.g., stainless steel), while the SPT incorporates a ceramic wall (e.g., boron nitride) and longer discharge channel. The secondary electron emission characteristics of the

discharge channel wall material is the primary distinction between these two types of thrusters.²⁷

Hall thrusters have been employed for a variety of Russian (and USSR) space missions since the late 1950s. It is interesting to note that during much of the duration of the Cold War, the United States focused on ion engine technology, while Hall thrusters were developed by the Russians and former Soviet Union. The SPT-100 were first studied in the early 1990s by the US for spacecraft integration,²⁸ and over the past three decades over 100 spacecraft (mostly Russian) have flown utilizing Hall thrusters.²⁹

Hall thrusters have slightly lower efficiencies than ion engines, due to beam divergence, and magnetic field optimization at lower voltages which do not extend to higher specific impulse operation. However, unlike ion engines, Hall thrusters are not limited by space-charge buildup since they utilize a quasi-neutral plasma. This allows higher currents and thrust densities to be achieved.³⁰ The specific impulse of Hall thrusters has been demonstrated from 1200 to 5000 seconds, with efficiencies ranging 40% - 72%³¹, however, the primary operating range for Hall thrusters is 1600 - 2500 seconds. The major lifetime-limiting phenomenon for Hall thrusters is erosion of the discharge channel, and its prediction and prevention are active areas of research in both experimentation³² and modeling³³ efforts.

1.3.4 A Summary of Electric Propulsion Systems

A summary of the different types of electric propulsion systems, operating conditions, and their uses is presented in Table 1-1.

Propulsion System	Electric Propulsion Type	I_{sp} (seconds)	Thrust (mN)	Efficiency (%)	Suitable Mission Applications
Resistojet	Electrothermal	150-350	5-300	65-90	<ul style="list-style-type: none"> • ACS • Station Keeping • Small ΔV • Orbit Relocation
Arcjet	Electrothermal	400-1500	200-1000	30-40	<ul style="list-style-type: none"> • Station Keeping • Orbit Relocation
MPD	Electromagnetic	2000-5000	0.001-2000	30-50	<ul style="list-style-type: none"> • Deep Space Propulsion • Large ΔV • Impulsive Maneuvers
PPT	Electromagnetic	600-2000	0.05-10	10	<ul style="list-style-type: none"> • ACS • Station Keeping
FEEP	Electrostatic	10,000	0.001-1	Nearly 100%	<ul style="list-style-type: none"> • Ultra-precise ACS
Colloid	Electrostatic	400-3000	0.05-5	70-80	<ul style="list-style-type: none"> • ACS • Primary Prop. for Microsats
Ion Engine	Electrostatic	1500-5000	0.01-200	60-80	<ul style="list-style-type: none"> • Station Keeping • Orbit Relocation • Deep Space Propulsion
Hall Effect Thruster	Electrostatic	1600-2500	0.01-3000	40-70	<ul style="list-style-type: none"> • Station Keeping • Orbit Relocation • Deep Space Propulsion

Table 1-1: Performance parameters of the major types of available electric propulsion systems.^{3,7,18,31,34,35}

As Table 1-1 shows, there are several kinds of electric propulsion systems to fulfill a wide variety of mission requirements. Most notably electric propulsion systems provide high specific impulse and low thrust capabilities.

Industry and governmental institutions around the world are interested in developing electric propulsion systems to satisfy the requirements of more ambitious missions in the future. For example, Hall thrusters and ion engines are being considered by NASA for a mission to Jupiter to tour the major Jovian satellites.³⁶ Therefore, it is imperative that the engine operation and plume interaction of electric propulsion systems with other spacecraft components is understood before they are employed for these ambitious missions.

An introduction to the relevant issues of Hall thruster integration with spacecraft is presented followed by a description of the recent trend in Hall thruster design into the high- I_{sp} / high-power regime. The need for the development of instrumentation to fulfill plume diagnostic requirements for these engines is claimed, and the “top hat” analyzer is proposed as a plume characterization tool to fulfill this necessity.

1.4 The Importance of Plasma Thruster Plume Diagnostics

Ground testing of electric propulsion systems is critical for characterizing and developing thruster performance parameters (e.g., specific impulse, thrust, input power, efficiency, etc.) that suit mission requirements. Another aspect of plasma thruster testing which must be studied is the propulsion system interaction on spacecraft components. Propellant emanating from the thruster has two properties which interfere with other parts of the spacecraft: propellant particles are highly energetic and are charged.

1.4.1 Inference of Thruster Performance via Plume Properties

For plasma thrusters in general, the highest efficiency is achieved when the cost of ion production (in terms of input energy) is minimized and input power converted to directed-kinetic energy is maximized. The efficiency of this process for ion engines and Hall thrusters in particular can be inferred by measurements of the ionic charge states and energy distribution of the propellant in the plume. Ideally, since the ionization energy per unit charge is lowest for the first charge-state, the number of singly-charged ions should be maximized, and any presence of multiply-charged ions indicates a loss in efficiency, thrust, and mass utilization.³⁷ The energy distribution for an ideal thruster would exhibit the form of a Dirac Delta function, with a peak at the anode voltage, signifying the propellant ions converted the full potential energy created between the anode and spacecraft ground into kinetic energy. Unfortunately this is not the case, as measurements on Hall thruster plume yield multiply-charged ions with peaks in multiples and fractions of a value slightly below the discharge voltage.³⁸ Plume diagnostics can quantify the performance of the thruster during operation through energy distribution and charge-state measurements.

1.4.2 Plume Impingement on Spacecraft Components

Since electric propulsion systems accelerate ions to tens of kilometers per second, the impact energy of propellant particles can damage other spacecraft components. Multiply-charged ions are accelerated to much higher energies than singly-charged ions thereby exhibiting a significantly higher threat to spacecraft components. Low-energy ions, which can be created through ion collisions with neutral particles, are easily affected by electric fields and can exit the thruster at large plume divergence angles. Due

to the charge of the propellant, parts of the spacecraft in contact with plume particles can buildup uneven charge.

Another example of the negative effect of plume particles on spacecraft hardware has been demonstrated with the presence of solar arrays. Laboratory tests on the SPT-100 Hall thruster yielded slight erosion of the antireflective solar cell cover glass coatings from a distance of one meter downstream due to sputtering. The measurements predicted a possible one percent degradation in the power system over the course of a typical communications satellite with a lifespan of 15 years.³⁹ For many electric propulsion systems in use today, solar arrays are utilized as the primary power source. Therefore the interaction of plume particles with solar arrays can even affect the propulsion system itself, by decreasing the available electric power to the propulsion system.

In addition to erosion/contamination effects, the accelerated ions can generate a force and thermal load on spacecraft components exposed to the plume. An accommodation coefficient of 0.6 has been measured for ions with energies in the range typical for Hall thruster plume.²⁸ This indicates most of the ion energy impinging on a spacecraft surface is transferred, rather than retained by the impact particle. Thermal and pressure stresses can result in uneven heating and attitude disturbances to the spacecraft.

1.5 The Future of Hall Thruster Design

The design of an effective plume diagnostic tool is dependent on the type of thrusters being developed. Instrumentation utilized for plume interrogation must be capable of fully characterizing the plume properties of engines in development for forthcoming space missions.

The past development of Hall thrusters for early missions utilizing electric propulsion is acknowledged, and the recent trends in development are discussed.

1.5.1 A Historical Perspective

Hall thrusters began development in the United States in the 1960s. Initially, engineers were interested in developing thrusters capable of specific impulses between 5000 and 10,000 seconds. It was widely believed that light-weight power sources would be available in the near future (relative to the 1960s) for developing EP systems for interplanetary missions. Due to unacceptably low efficiencies achieved when operating these thrusters at high specific impulses, this early work on Hall thrusters ceased in the early 1970s for over a decade. The low efficiencies were due to electron backflow which caused difficulties in ion production.⁴⁰

In 1985 Ford Aerospace (now Space Systems/Loral) and NASA Lewis Research Center (now NASA Glenn Research Center) unsuccessfully researched the possibility of utilizing Hall thrusters for NSSK. The program was abandoned in 1990.⁴¹

On the other hand, the Soviet Union successfully tested a Hall thruster in space in 1971,⁴² and has since utilized more than a hundred Hall thrusters for space operations. During the early 1990s, Hall thrusters became and remained attractive in the United States for near-Earth missions such as low-earth to geosynchronous orbit (LEO to GEO).⁴³ The specific impulse range for Hall thrusters developed from these programs was 1600 - 2000 seconds.

1.5.2 Recent Trends in Hall thruster and Ion Engine Design

An increase in electrical power availability coupled with growing mission requirements has resulted with the expansion of the power range in operation of Hall thrusters. Recent trends in Hall thruster research by the USAF and US industry have included the high-power (> 20 kW) regime.⁴⁴ NASA is sponsoring high-power / high- I_{sp} (10 kW / ≥ 2000 second) Hall thruster technology through NASA Glenn Research Center (GRC).⁴⁵ The NASA-457 Hall Thruster developed at GRC produced the highest power level and thrust (75 kW and 2.9 N) achieved by any xenon-propellant Hall thruster.⁴⁶ High I_{sp} anode layer type thrusters have achieved specific impulses above 4100 seconds at this center as well.⁴⁷ The trends indicate the expansion of the operating envelope to higher specific impulses and powers for Hall thrusters.

1.6 Research Aim and Contribution

For these high-power / high- I_{sp} engines and future even more powerful thrusters being developed, plume characterization is imperative for determining their effect on spacecraft systems. Plasma transport properties, charge state, and ion energy distributions are also important for understanding how Hall thrusters work and achieving the ultimate goal of improving their importance.⁴⁸ The top hat analyzer is first described, and the central endeavor of developing and utilizing a top hat analyzer for plume diagnostics is then presented.

1.6.1 The Top Hat Analyzer

One technique for determining the energy-to-charge (E/q) distribution of plasma is to use an electrostatic analyzer. A specific geometry for the electrostatic analyzer,

which allows for angular measurements in a wide field-of-view, is the top hat analyzer. This electrostatic analyzer consists of two concentric hemispheres, with an aperture at the apex of the outer hemisphere. Figure 1-6 illustrates the main components of the top hat analyzer.

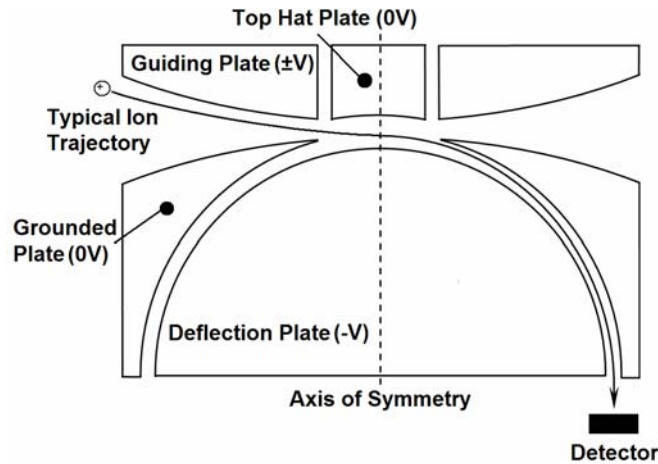


Figure 1-6: The major components and a typical ion trajectory for a top hat electrostatic analyzer.

The inner hemisphere is biased to a negative voltage while the outer hemisphere is grounded. The electric field created between the plates allows for particles within a specific energy range (corresponding to the inner plate voltage) to pass through the aperture and through the gap between the plates. By virtue of its geometry, the top hat analyzer is capable of having a nearly 360-degree azimuthal (horizontal angle) field-of-view. Steering electric fields allow for a field-of-view in the vertical direction as well. Through the electrostatics and geometry of the top hat analyzer, the energy-per-charge, azimuthal angle, and elevation angle of incoming ions is measured.

By integrating a mass spectrometer with the top hat analyzer, the velocity distribution of the plasma (within the field-of-view) can be determined. The distribution function allows for derivation of macroscopic properties such as the transport properties

and temperature of the plasma through integration over velocity space. Due to the high atomic mass of propellants (i.e., Krypton and Xenon), the charge states within the plume are also easily isolated through use of the mass spectrometer.

1.6.2 Motivation for a Top Hat Analyzer for Plume Diagnostics

Electrostatic analyzers have been and are currently employed on spacecraft to investigate space plasmas such as the solar wind as well as the ionospheres and magnetospheres of Earth and other planets.^{49,50} Space plasmas offer a wide range of particle energies from less than 1 eV to several MeV. The desire to study these particles has led to the design of electrostatic analyzers capable of detecting particles over several orders of magnitude in energy;⁴⁹ however, these types of plasmas have an ion number density several orders of magnitude lower than Hall thruster and ion engine plumes. Figure 1-7 describes the typical energy and number density ranges of space, laboratory, and Hall thruster and ion engine plasmas.

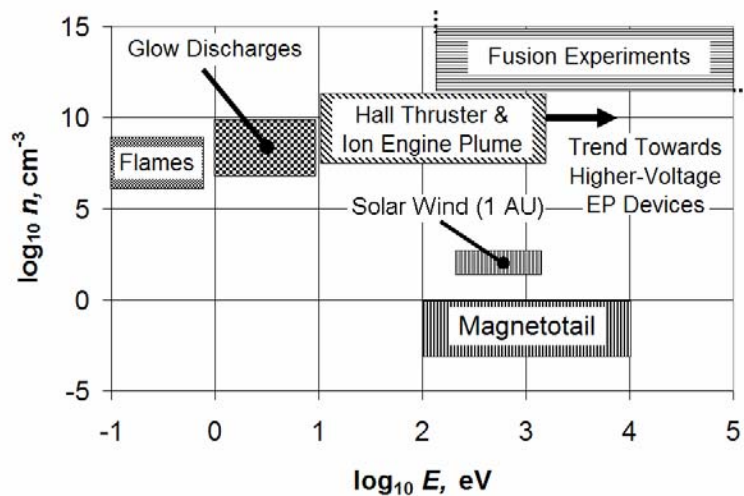


Figure 1-7: Number density and energy of typical space, laboratory, and electric propulsion plasmas.

Hall thruster plume is nestled between laboratory plasmas (thetatrions and fusion reactors) and space plasmas (solar wind and the magnetotail) on the density scale and similar to the magnetotail and solar wind plasma in terms of energy.

There are many examples of space plasma detectors that use the top hat configuration. EP plume measurements with this type of device, however, are much rarer. The Plasma Experiment for Planetary Exploration (PEPE), flown on Deep Space 1 (DS1)⁵¹, included a dual top hat analyzer to measure electrons and ions from the solar wind, the spacecraft photoelectron sheath, and products of the xenon ion propulsion system (XIPS). Low energy xenon ions at ~20 eV created from the beam ion interaction with neutral xenon particles leaving the thruster were observed by PEPE.⁵²

Although beam ions were not measured by PEPE due to the position and orientation of the thruster with respect to the instrument, the observation of charge-exchange ions provides evidence that the top hat analyzer can be used as a plume diagnostics tool for characterizing facility effects. Hall thrusters have been shown to yield higher current density profiles in the far-field plume at higher background pressures. It is theorized that charge-exchange ions created from beam ions and neutral background particles are the culprit for the elevated current densities.⁵³ Diagnostic tools capable of characterizing the low-energy charge-exchange ions as well as the high-energy beam ions are therefore necessary to distinguish facility effects on plume diagnostics.

1.6.3 Focus of Research

The principle aim of the research presented in this dissertation is the extension of top hat technology from the space plasma applications to the electric

propulsion plume-diagnostics field. The design, development, and utilization of a top hat analyzer for far-field plume diagnostics are described.

To this author's knowledge, a top hat analyzer has never been developed for the *sole* purpose of electric propulsion plume diagnostics. The research presented seeks to introduce the top hat analyzer as a viable electric propulsion plume-diagnostics tool, while concurrently addressing necessary modifications and limitations of the instrument. Due to the instrument's capability of fully characterizing high-energy plasmas, the top hat analyzer aides the successful integration of Hall thrusters being developed for more ambitious missions of the future. Plume diagnostics allows spacecraft designers to predict the environment of spacecraft components within the influence of a plasma thruster. Interrogation of the far-field plasma also reveals information on the performance of the thruster. For future engines being developed, a wide energy-range of particles will need to be characterized. The top hat analyzer has this ability.

1.7 Thesis Roadmap

A survey of existing plume diagnostic techniques is presented, with a comparison of the top hat analyzer. The theoretical design of the instrument is discussed in Chapter 3. Further specifics of the design are completed through the use of SIMION and Pro/ENGINEER, ion optics and solid modeling programs, respectively. Characterization of the instrument's voltage-energy and voltage-angle correlations is conducted through use of an ion beam facility in Chapter 4, and energy measurements on a Hall thruster and cluster of thrusters are then presented in Chapter 5.

Chapter 6 describes the integration of a mass spectrometer to the instrument. The instrument's capability is determined through an ion beam facility utilizing krypton,

xenon, and air propellants. Mass spectrometry measurements are discussed on the BHT-600 Hall thruster cluster.

Finally the instrument's applicability towards plume diagnostics and "lessons learned" during the development phase are presented, and recommendations for future designs for top hat analyzers and similar instruments are discussed in Chapter 7.

CHAPTER 2: PLUME DIAGNOSTICS AND THE TOP HAT ANALYZER

The top hat analyzer yields a surplus of benefits to plume diagnostics for electric propulsion engines (and Hall thrusters in particular) when compared with other types of diagnostics instruments. A brief overview of the major plume diagnostics tools is described in this chapter, and a comparison of the top hat analyzer with existing techniques is presented.

2.1 The Drive for Plume Characterization

As discussed in Chapter 1, plume diagnostics is essential for understanding the effect of EP systems on spacecraft. There are several types of instruments utilized (both in-situ and remote) to determine properties of the plume. For the purposes of this dissertation, the far-field plume will be defined as positions greater than or equal to 75 cm from the intersection of the thruster/cluster axial centerline with the exit plane of the discharge channel. All positions within 25 cm of this point are in the near-field plume, while the region from 25 cm to 75 cm is considered the mid-field plume.

The plume is composed of plasma consisting of electrons, neutral particles, and ions, for which macroscopic properties of each, such as density, mean velocity, temperature, and pressure, are desired. These macroscopic values are related to the 0th, 1st, and 2nd moments of the velocity distribution functions (VDFs) of each of these

populations.⁵⁴ Since all macroscopic quantities can be derived from the VDF, a complete measurement of this function for each type of particle yields all information about the plasma and is therefore highly desired.

Since highly-energetic charged particles are the major source of spacecraft damage from plasma thrusters, most diagnostic techniques are concerned with the characterization of the ion distribution instead of the neutral propulsion of particles in the plume. The diagnostic techniques described focus on ion distribution measurements, however, neutral particle measurements can yield valuable information on propellant utilization (and therefore thruster efficiency), facility effects,⁵⁵ and the plasma state of the inner region of the thruster⁵⁴ since neutral particles are unaffected by confining magnetic fields. A discussion of the principle diagnostic tools utilized for plume ion diagnostics follows.

2.2 A Survey of Plume Diagnostics Instruments

There are several instruments available for plume diagnostics. The three major types of diagnostics tools are direct-contact, remote sensing, and particle filtering techniques. The top hat analyzer is an ion filter-type instrument. A brief introduction to the major diagnostics tools and techniques for plume diagnostics is presented. The numerous instruments available for plume diagnostics preclude an encyclopedic description, therefore, only the most common diagnostics are included.

2.2.1 Direct-Contact Probes

Direct-contact probes are placed in-situ with the plasma at the location to be measured. These probes include (but are not limited to): Faraday Probes, Langmuir

Probes, and Emissive Probes for ion diagnostics as well as Hall probes and B-dot probes for magnetic field and (indirectly) electron current measurements.

2.2.1.1 Faraday Probe

Faraday probes are perhaps the simplest tool available for plume diagnostics. They are utilized for measuring ion current densities which is useful for determining plume divergence when measured as a function of thruster plume angle.⁵⁶ Faraday probes consist of a surface collection area surrounded by a guard ring. The collection area is usually spray-coated with tungsten to minimize secondary electron emission. Both the collection area and guard ring are biased negatively to repel electrons from the collection surface and minimize the negative electron influence on positive ion current measurements.

2.2.1.2 Langmuir Probe

Langmuir probes are similar to Faraday probes in that they measure current density, however, the probe is swept through a range of voltages, such that a saturation in ion and electron current is reached at the low and high ends of the range, respectively. The plasma potential, floating potential, electron temperature, electron density, ion density, and an estimation of the ion temperature can be extracted from the current-voltage relationship measured with the Langmuir probe. Due to the desire to minimize the perturbation of plasma by the Langmuir probe, the collection area is generally minimized, however, for high temperature and high density plasmas, probe damage can limit and prevent the in-situ measurements with this instrument.

2.2.1.3 Emissive Probe

Emissive probes purposely employ electron emission to determine the plasma potential. The probe is heated electrically or by the plasma, and electrons emitted by the probe are either collected or dispersed into the plasma depending on the probe's potential with respect to the plasma potential. The voltage of the probe is varied, and a change in probe current due to the emission of electrons signifies the probe is biased to the plasma potential. Below this potential, the emissive probe functions as a Langmuir probe, and therefore measurements of the electron temperature, floating potential, and ion density are possible with accurate knowledge of the probe collection area. The electric field structure of Hall thruster plume can be determined through emissive probe measurements as well.⁵⁷

2.2.1.4 Magnetic Field Probes

Measurements of the magnetic field topology and Hall current are possible with the Hall and B-dot probes, respectively. The Hall probe passes current through a semiconductor and generates charge build-up due to the Lorentz force of the magnetic field being measured. The voltage differential from the charge build-up is proportional to the magnetic flux density. Hall probes have been utilized for mapping magnetic field topography in MPD thrusters, Hall thrusters, and ion engines as well.⁵⁸⁻⁶⁰ B-dot probes measure the rate of change of magnetic flux. By sweeping the probe through a magnetic field, integration of the signal yields the magnetic field strength. B-dot probes have been used for mapping magnetic topology of Hall thrusters, as well as estimating the Hall current within the discharge channel.⁶¹

2.2.2 Remote Sensing Techniques

Remote sensing techniques include emission spectroscopy, laser-induced fluorescence (LIF), and microwave interferometry. The benefit of remote sensing techniques is that the plasma is not perturbed (or insignificantly perturbed), and locations inaccessible for in-situ measurements, due to either harsh plasma conditions or physicality, can be diagnosed.

2.2.2.1 Emission Spectroscopy

Emission spectroscopy relies on a particle's natural emission of photons when it is relaxed from an excited electronic state. The total number density, temperature distributions, and ionization fractions can be deduced for individual species within the thruster plume.^{62,63} A scanning monochromator with a photo-multiplier tube can be utilized to measure a single frequency or scan a range of frequencies, and measure the intensity of emission from the de-excitation of plume particles.

2.2.2.2 Laser-Induced Fluorescence

While emission spectroscopy passively measures emitted photons from the plasma, laser-induced fluorescence (LIF) is utilized to purposely excite particles into higher energy states. The particles' return to the lower-energy state yields emission of electromagnetic radiation. The emission is stimulated in a controlled manner, and accurate measurements of velocity (in multiple directions) and absolute density are possible.⁶⁴

2.2.2.3 Microwave Interferometry

Microwave interferometry measures electron number density by measuring phase shifts in microwave signals sent from an antenna through the plasma to a receiver. By varying the position of the antenna, electron density profiles of a plasma thruster plume as a function of position can be produced, non-intrusively.⁶⁵ This technique has been used extensively for fusion plasma characterization⁶⁶ since in-situ diagnostics tend to be difficult due to the high temperature and density of these plasmas.

2.2.3 Particle Filtering Techniques

Particle filtering techniques employ applied electric and/or magnetic fields to divert a small energy or mass range of particles to the detector. Information is also derived through dynamic electric fields and measurements of the detection time (i.e., the ions are *temporally* filtered) or ion resonance with an oscillating field. Neutral particle analysis can also be conducted by filtering all charged particles with electric or magnetic fields. While particular attention is made to minimize the direct-contact probe's influence on the plasma of interest, particle filters intentionally create a controlled environment about the plasma, such that a known subset of particles arrives at the detector. By varying the environment (e.g., applied electric and magnetic fields) of the plasma, distributions of the particle velocity, charge-state, and mass can be derived.

2.2.3.1 Magnetic Filtering Techniques

Two analyzers which utilize magnetic fields are the magnetic sector and $\mathbf{E} \times \mathbf{B}$ probe. The magnetic sector utilizes a magnetic field applied over a curved channel (hence the "sector") to select ions of a particular momentum-per-charge. The Lorentz Force

equation for an ion of charge q in an electric and magnetic field illustrates how this works:

$$\vec{F} = q(\vec{E} + \vec{v} \times \vec{B}) \quad \text{Eqn. 2-1}$$

In the absence of an electric field, the required acceleration for particles to travel through a channel with a radius r is v^2/r . The magnetic field is usually perpendicular to the velocity, so the vectors are reduced to scalar quantities. By inputting this expression into Equation 2-1 and solving for the known applied magnetic field strength B and radius r , the following relationship is derived:

$$Br = \frac{mv}{q} \quad \text{Eqn. 2-2}$$

It is important to note that in many cases magnetic sectors are employed in combination with energy analyzers, and the combination of an energy-per-charge selection yields a velocity distribution in one dimension. $\mathbf{E} \times \mathbf{B}$ probes (Wien filters) employ the same principles as a magnetic sector/energy analyzer combination, however, an electric field is applied perpendicular to the magnetic field and the channel is a straight path. If the electric and magnetic forces are balanced in opposite directions, the ion trajectory is unchanged and falls straight into the detector. Through variation of the electric and/or magnetic fields, a 1-D velocity distribution is recovered. By setting the force vector in Equation 2-1 to zero, the simple relationship is received for the velocity of ions detected in relation to the applied electric and magnetic field:

$$v = -\frac{E}{B} \quad \text{Eqn. 2-3}$$

$\mathbf{E} \times \mathbf{B}$ probes are employed extensively for measurements of ionic charge states in Hall thruster plume with the presumption that ions are accelerated to the same energy-

per-charge. This is a good assumption;⁶⁷ however, charge-exchange collisions (CEX) prevent exact ion species fractions from being measured with this technique.⁶⁸

2.2.3.2 Time-of-Flight Spectrometry

Like the $\mathbf{E} \times \mathbf{B}$ probe, time-of-flight (TOF) spectrometry directly measures a speed distribution of ions within the plasma. With precision electronics the resolution tends to be much higher, and the profile is almost instantaneously measured. Ions are initially prevented from passing through a large electric field, which acts as an electrostatic “gate,” at a known distance from the detector. For a brief moment, ions are allowed to pass through, and the arrival times of the ions are measured at the detector. A mass-per-charge distribution can be derived for ions with the same energy-per-charge, and for the massive propellant ions (e.g., xenon and krypton), ionic charge states can be determined. A TOF technique is utilized for TOPAZ and is discussed extensively in Chapter 6.

2.2.3.3 Quadrupole Analyzer

A similar mass-per-charge instrument is the quadrupole analyzer. The quadrupole analyzer consists of four parallel rods. The rods are electronically biased with an RF frequency superimposed over a DC voltage. Oppositely aligned rods share the same charge, and adjacent rods are biased negatively with respect to each other. Ions travel between the parallel rods, and only ions of a select mass-per-charge are detected at the end of the setup. Other ions will have an unstable trajectory and collide with either the rods or exit the detectable area. By varying either the DC and AC voltages or the RF frequency, a mass-per-charge profile can be generated.⁶⁹

2.2.3.4 Retarding Potential Analyzer

Most ion-filtering energy analyzers incorporate electrostatic fields to determine an energy-per-charge profile. The retarding potential analyzer (RPA) incorporates perpendicular electrostatic fields to filter a subset of ions from the detector. Figure 2-1 describes the electrostatics for the RPA.

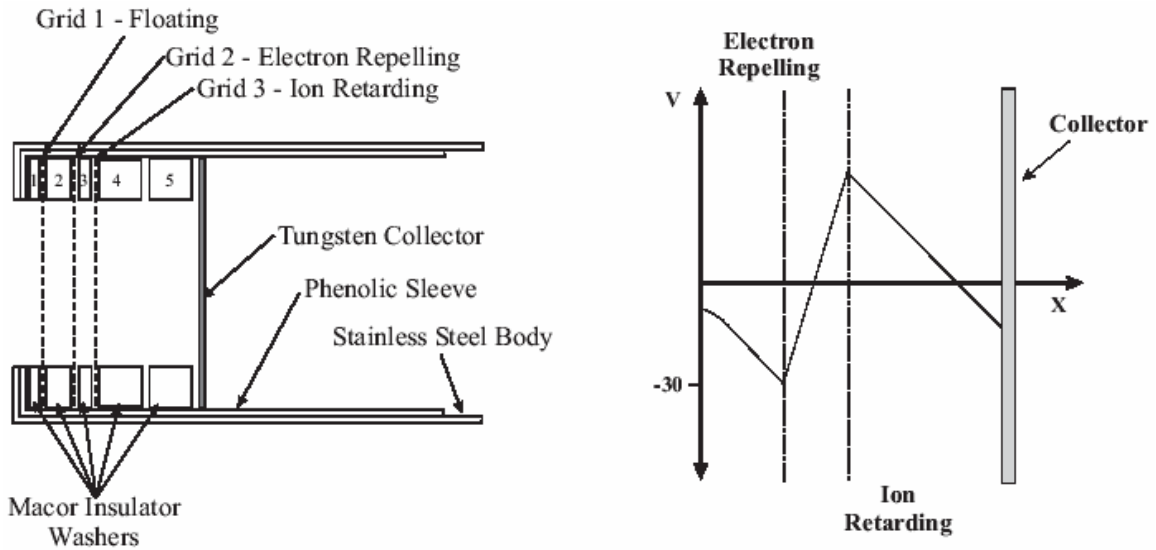


Figure 2-1: A schematic and plot of the potential for the retarding potential analyzer.⁷⁰

The RPA consists of an electron repelling and ion retarding grid placed in front of a detector. The electron repelling grid is biased such that electrons are unable to pass through to the detector. The ion retarding grid is initially grounded, and the bias is steadily increased until no ions are able to pass through the grid to the detector. The derivative of the signal as a function of ion retarding grid potential V_{grid} is related to the energy-per-charge (E/q) distribution of the plasma through Equation 2-4.⁷⁰

$$\frac{dI}{dV_{grid}} = -\frac{q^2 e_c^2 n_i A}{m_i} f(E/q) \quad \text{Eqn. 2-4}$$

The ion's charge state and mass are represented by q and m_i , while the area of the probe and the ion number density is represented by A and n_i , respectively. The electron charge is represented by e_c . The RPA requires differentiation of the signal which induces an increase in noise. The relative size of the instrument (1-2 cm) and simplicity, however, makes the RPA an excellent far-field plume diagnostics energy analyzer which can be moved easily on translation tables for studying multiple plume angles.

2.2.3.5 Electrostatic Analyzer

Another type of energy analyzer is the electrostatic analyzer (ESA). Electrostatic analyzers utilize electric fields which are perpendicular to the velocity of the ions. In a similar manner to the magnetic sector, a select range of ions is guided through a physical path to arrive at the detector. The ESA measures the energy-per-charge distribution of the plasma, and unlike the RPA, does not require differentiation of the signal. The top hat analyzer is a type of electrostatic instrument, since it utilizes orthogonal electrostatic fields to select ions.

Perhaps the simplest electrostatic analyzer is the parallel plate analyzer. This device consists of two parallel plates with one biased to a positive or negative voltage (for detecting positive or negative ions, respectively) while the other is grounded. Ions pass through an entrance slit, while the exit slit acts as an energy-per-charge filter. The electric field generated between the two plates allows ions of a small energy-per-charge range to follow the correct parabolic path from the entrance to the exit slit. Figure 2-2 displays a diagram of the parallel plate analyzer.

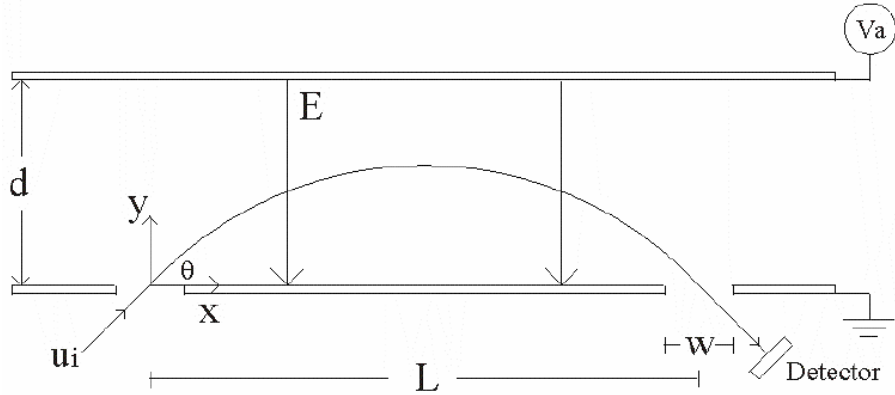


Figure 2-2: A schematic of the parallel plate analyzer.⁷¹

Ions traverse through the left slit and are curved in a parabolic trajectory due to the electric field E created between the plates. For $\theta = 45^\circ$, the trajectory of the ions is described by the following equation:⁷¹

$$y = x - \left(\frac{1}{2d} \right) \left(\frac{V_a}{E_i/q} \right) x^2 \quad \text{Eqn. 2-5}$$

The ratio of the distance between the slits to the separation of the parallel plates describes a dimensionless property of the geometry for the parallel plate analyzer. This expression also relates the applied plate potential V_a to the energy-per-charge measured by the detector and is defined as the spectrometer constant or analyzer constant K_{45} .

$$K_{45} \equiv \frac{L}{2d} \quad \text{Eqn. 2-6}$$

The analyzer constant defines the relationship between the parallel plate voltages, and is closely related to the resolution and selectivity of the instrument. Equation 2-7 describes the plate voltage relationship with the energy-per-charge measurement for the parallel plate analyzer:

$$\frac{E}{q} = K_{45} V_a \quad \text{Eqn. 2-7}$$

Electrostatic energy analyzers (ESAs) have evolved into different geometries to include angular measurements and increased resolutions through the use of clever electrostatics design. These other types of ESAs include the radial cylindrical analyzer, axial-focusing cylindrical-mirror analyzer, hemispherical analyzer,⁷² and toroidal analyzer⁷³. The top hat analyzer, introduced in 1982 by Carlson, et al.,⁷⁴ utilizes electrostatics to measure horizontal and vertical angular distributions, as well as energy-per-charge profiles, while maintaining high resolutions among each parameter. Electrostatic analyzers can be combined with mass spectrometers, to provide velocity distribution measurements within the field of view.

2.2.4 A Summary of Plume Diagnostics Instruments

A summary of the direct contact, remote sensing, and particle filtering instruments described is provided in Table 2-1, Table 2-2, and Table 2-3, respectively.

Instrument	Regime(s) of Use for Hall Thruster Plume	Measurement Capabilities	Complexity and/or Issues
Faraday Probe	- Far-field - Flush-mounted for internal diagnostics	- Ion Current Density - Beam Divergence	- Extremely Simple - Limited Measurements
Langmuir Probe	- Far-field - Near-field & Internal with Short Resonance Times	- Electron Density, Temperature - Ion Density, ~Ion Temperature - Space & Floating Potentials	- Very Simple - Flowing Plasma Requires Additional Data Analysis ⁷⁵
Emissive Probe	- Far-field - Near-field & Internal with Short Resonance Times	- Electron Temperature - Ion Density, ~Ion Temperature -Space (accurate), Floating Potentials	- Fairly Simple - Requires significant sheath corrections
Hall Probe	- Near-Field & Internal with Thruster(s) Off	- Magnetic Field Topology Mapping	- Simple - Utilized for field measurements
B-dot Probe	- Near-Field & Internal with Short Resonance Times	- Magnetic Field Topology Mapping - Hall Current Estimation	- Simple - Requires Integration of Signal

Table 2-1: A summary of direct contact methods for plasma thruster plume characterization.

Instrument	Regime(s) of Use for Hall Thruster Plume	Measurement Capabilities	Complexity and/or Issues
Emission Spectroscopy	- Far-Field - Near-Field & Internal - High-Density Plasmas	- Total Number Density - Temperature Distribution - Ionization Fractions	- Fairly Simple - Slightly Expensive - Optical Setup Required - Unobstructed Views Only - No plasma interaction
Laser-Induce Florescence (LIF)	- Far-Field - Near-Field & Internal - High-Density Plasmas	- Total Number Density - Temperature Distribution - Velocity Distribution - Ionization Fractions	- Requires Elaborate Optics Setup - Very Expensive - Enables Accurate Plume Interrogation of Limited Area - Virtually no plasma interaction
Microwave Interferometry	- Far-Field - Near-Field - High-Density Plasmas	- Electron density	- Fairly Simple - Plume Profiling Possible with Movement Tables - Non-intrusive

Table 2-2: A summary of remote sensing methods for plasma thruster plume characterization.

Instrument	Regime(s) of Use for Hall Thruster Plume	Measurement Capabilities	Complexity and/or Issues
Magnetic Sector	- Far-Field	- Momentum-per-Charge Distribution - ~ Ionization Fractions	- Very Simple - Large / Heavy
$E \times B$ Probe	- Far-Field	- 1-D Velocity Distribution - ~ Ionization Fractions	- Simple - Large / Heavy
Time-of-Flight	- Far-Field - Low-Density Plasmas	- 1-D Velocity Distribution (accurate) - ~ Ionization Fractions - Mass-per-Charge Distribution (with Energy Analyzer)	- Simple Design - Requires Drift Path & Accurate Electronics - Instantaneous Direct Velocity Distribution
Quadrupole Analyzer	- Far-Field - Low-Density Plasmas	- Very Accurate Mass-per-Charge Distribution	- Fairly Simple - Requires Drift Path - Moderately Complex Biasing / Accurate Electronics
Retarding Potential Analyzer (RPA)	- Far-Field - "Mid"-Field with Miniaturization	- Energy-per-Charge Distribution	- Very Simple - Requires Integration of Signal
Electrostatic Energy Analyzer (ESA)	- Far-Field - "Mid"-Field with Miniaturization	- Energy-per-Charge - Angular Distributions	- Fairly Simple - Size Limits Use to Far-Field - Can be combined with mass spectrometers

Table 2-3: A summary of particle filtering methods for plasma thruster plume characterization.

Some trends in the type of instrument and measurement capabilities and uses are apparent with the above table. Direct contact probes offer a wide measurement capability

while maintaining their relative ease of use. The Langmuir probe's simple setup, and measurement capability for several plasma parameters, has locked it as a standard diagnostics tool for plume studies. Remote sensing techniques are well suited for accurate velocimetry measurements where a low-perturbation of the plasma is preferred. This technique is applicable to a wide variety of plume types; however, complicated setup with an unobstructed view of the plasma prevents extensive plume profiling. In the far-field plume, particle filtering techniques offer simple designs, while allowing for multi-position plume measurements. Particle filters can be combined with each other to produce more powerful diagnostics.

2.3 Top Hat Analyzer Capabilities

Since the top hat analyzer can measure energy and angular profiles, velocimetry measurements in multiple dimensions are possible with the attachment of a mass analyzer. This allows for similar measurement capabilities to laser-induced fluorescence, as well as multi-position interrogation of the plasma without complex setup processes. The choice of a top hat analyzer for far-field plume diagnostics arises from its angular and energy capabilities, as well as the ease of repositioning the instrument to multiple areas of the far-field plume.

2.3.1 The Evolution of the Top Hat Analyzer

Several geometries exist for electrostatic energy analyzers (ESAs). The desire for increased energy resolutions, angular distribution measurements, and an increased field-of-view (FOV) forced the evolution of ESAs from the simple parallel plate analyzer to the top hat analyzer and other clever electrostatic designs which fulfilled the individual

design requirements for the mission. An example of a unique design is the Fast Imaging Plasma Spectrometer (FIPS) on the MESSENGER spacecraft which will characterize the plasma environment around Mercury.⁷⁶

Figure 2-3 describes some of the major electrostatic analyzer designs leading up to the top hat analyzer.

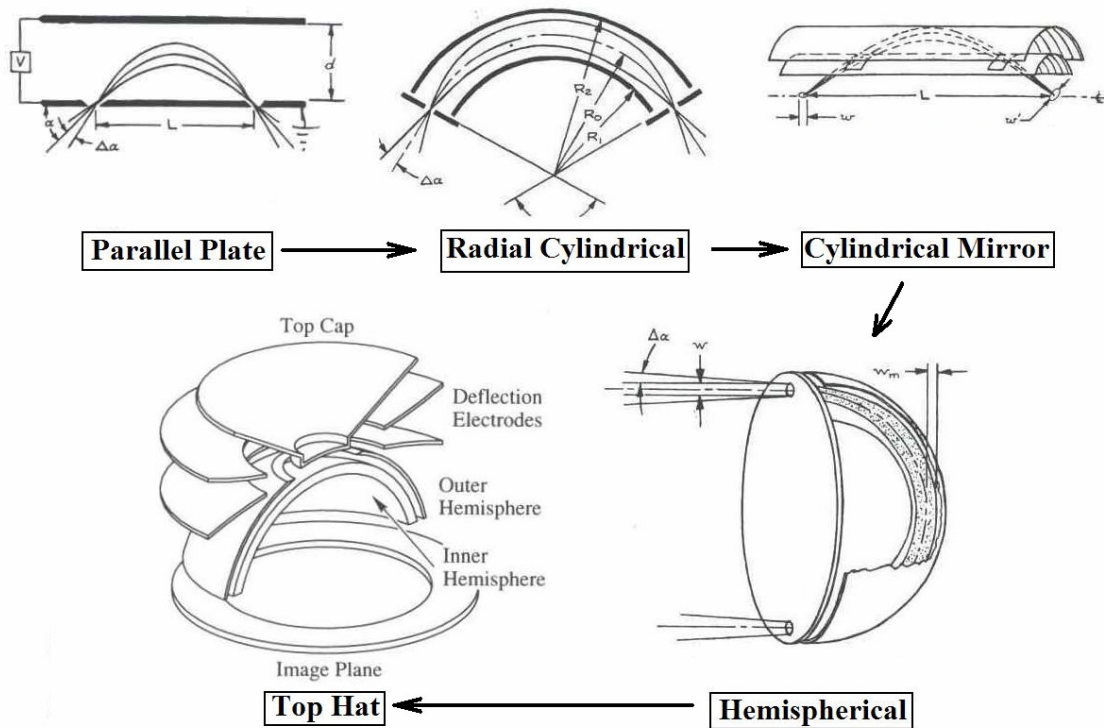


Figure 2-3: The evolution of the geometry for the top hat analyzer.^{72,77}

The parallel plate and radial cylindrical analyzers provide energy-per-charge measurements of the plasma, however the radial cylindrical design offers a superior resolution and does not require a large deflection region (and hence high plate voltages) for the same measurement.⁷² By concentrically curving the parallel plate analyzer, the radial-cylindrical mirror analyzer is produced, and ion trajectories are focused on both ends of the analyzer. This geometry allows for particles at multiple azimuthal angles (in and out of the page) to be collected. If the radial-cylindrical mirror analyzer is extended

180° and rotated about the azimuthal axis, the hemispherical analyzer is generated. This analyzer allows for ions to be collected from a small angular deviation $\Delta\alpha$ in any direction. The top hat analyzer is created through the addition of deflection electrodes and a replacement of the entrance and exit apertures with an entrance at the top of the hemisphere and an azimuthal exit channel, respectively. This makes the top hat analyzer similar to a right-angled radial cylindrical analyzer (otherwise called a quadrispherical analyzer) rotated 360° about the entrance. The deflection electrodes and exit channel allow for angular resolving in vertical and horizontal directions, respectively. The concentric hemispheres in the top hat analyzer maintain the focusing properties of cylindrical mirror and hemispherical analyzer designs.

Extensions of the top hat analyzer include “flat top” toroidal geometry which extends the focusing point beyond the channel exit.⁷⁸ This is useful for placing a time-of-flight detector system after the particle has exited the channel.

2.4 Summary

As stated in Chapter 1, far-field plume characterization is imperative for the integration of plasma thrusters onto spacecraft. The top hat analyzer in conjunction with a mass spectrometer offers a wide measurement capability with an easy setup for far-field plume diagnostics, as compared with existing plume diagnostics techniques.

The next chapter describes the theoretical design and computational modeling employed for the design the Top Hat Electric Propulsion Plume Analyzer (TOPAZ).

CHAPTER 3:

DESIGN AND THEORETICAL CHARACTERIZATION OF TOPAZ

In this chapter, the design requirements, theoretical design, computational simulation, and computer-aided design (CAD) of the Top Hat Electric Propulsion Plume Analyzer (TOPAZ) are discussed. The design requirements are first presented. Then the governing equations are discussed and solved for a preliminary design of the instrument to fulfill the design requirements. SIMION, a commercial ion optics simulation program, is utilized to characterize the plate-voltage relationships, and predict the resolutions and sensitivity of the instrument. An iterative process with SIMION is used to hone the model of the instrument to satisfy design requirements. Structural constraints are added to the design through use of the CAD program Pro/ENGINEER. The overall theoretical performance of the instrument is presented at the end of the chapter.

3.1 Design Requirements

The design requirements are dependent on the plasma being investigated by the instrument. The energy and angular design specifications arise from the increase in Hall thruster and ion engine operating voltages and the desire to accurately characterize high-energy beam ions (i.e., ions created and accelerated from near the discharge channel) from all parts of the thruster.

3.1.1 Energy Range Requirements

As stated in Chapter 1, an increase in power and specific impulse is expected for Hall thruster development in the future. The increased acceleration potentials inevitably lead to higher-energy beam ions emitted from the thruster, and hence a higher energy plume. While Hall thruster voltages are not expected to increase above 2 kV, ion thrusters that are being considered for deep space missions may have xenon ions of energy above 6 keV.⁷⁹ Although TOPAZ is utilized for Hall thruster plume diagnostics, the instrument could aid plume analysis of these high-voltage ion engines. A Xe^{2+} ion would accelerate to 12-14 keV at this potential; hence, a high-energy measurement capability of up to 15 keV was desired for TOPAZ. The nature of a top hat analyzer allows for the lower bound to be close to 0 eV, since the deflection plate potential directly corresponds with the energy-per-charge being measured. The lower-energy bound therefore is set by the accuracy of the power supplies used as well as space-charging limitations.

An energy profile of the P5 Hall thruster operating at 500 V, 10 A at a 0° thruster angle is shown in Figure 3-1.

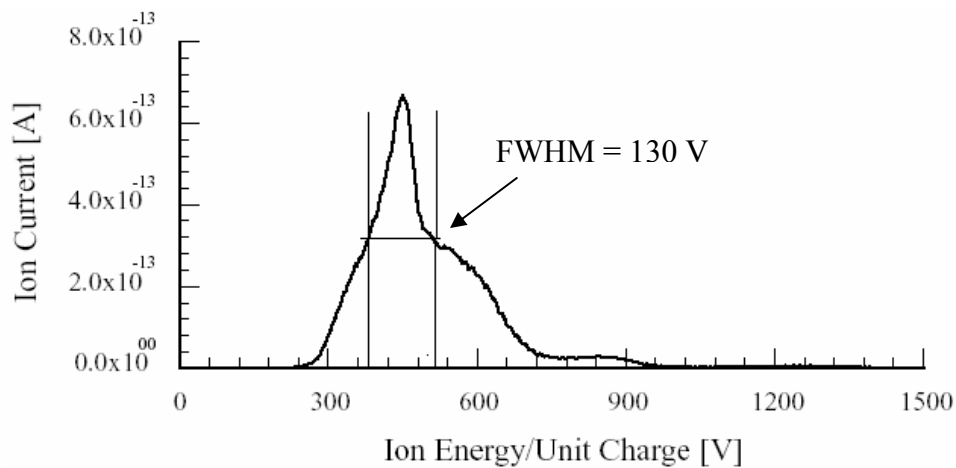


Figure 3-1: Energy-per-charge distribution one meter down the centerline of the P5 Hall thruster operating at 500 V 10 A.⁸⁰

A peak near 460 V exists with a full-width at half-maximum (FWHM) of 130 V. For an accurate resolving of this peak in increments of 2 V, and energy resolution ($\Delta E/E$) of 1.5% is required for the detector. Since a previous parallel plate analyzer designed for Hall thruster plume diagnostics, the Miniaturized Ion Energy Analyzer (MIEA), had this capability,⁷¹ an energy resolution of 1.5% was chosen as a design requirement of TOPAZ to maintain this accuracy as a plume diagnostics instrument.

3.1.2 Angular Resolution Requirements

Since TOPAZ is a far-field plume diagnostics instrument, an adequate field-of-view (FOV) is required to “image” the ions ejected from the entire discharge channel. A 30° vertical (elevation) FOV allows for 54 cm of an object to be viewed from 1 m away, well within the size range of most thrusters. The horizontal (azimuthal) angular FOV for top hat analyzers is ideally 360° by virtue of the geometry, however structural constraints can diminish this value. Angular resolutions in the FOV of 2°×2° (elevation × azimuthal) were chosen for TOPAZ, since this provides enough accuracy to determine the origin of a detected ion from the discharge channel, a different part of the thruster, or the plume.

3.1.3 Plasma Property Considerations

Although top hat analyzers have been utilized for the investigation of plasmas with energies well above Hall thruster and ion engine plume, the number densities are significantly lower for space plasmas than plasma thruster plume (see Figure 1-7). The relevant plasma properties of the P5 thruster, from one meter downstream are listed in Table 3-1.

Plasma Parameter	Value
Floating Potential, V_f	-1 – 2 V
Plasma Potential, V_p	6 – 11 V
Electron Temperature, T_e	1.1 – 2.1 eV
Electron Number Density, n_e $\geq 30^\circ$ from Centerline Along Centerline	$5 \times 10^{15} - 4.5 \times 10^{16} \text{ m}^{-3}$ $2 \times 10^{16} - 1.4 \times 10^{17} \text{ m}^{-3}$
Ion Number Density, n_i $\geq 30^\circ$ from Centerline Along Centerline	$5 \times 10^{15} - 3 \times 10^{16} \text{ m}^{-3}$ $5 \times 10^{16} - 3 \times 10^{17} \text{ m}^{-3}$
Species Composition	
Xe ⁺	92.5%
Xe ²⁺	6.8%
Xe ³⁺	0.7%
Xe ⁴⁺	Trace Amounts
Operating Pressure	1×10^{-5} Torr

Table 3-1: Plasma conditions one meter downstream the P5 Hall thruster operating at 300 V, 5.3 A.⁸⁰

The significantly higher electron and ion number densities present the possible problem of Debye shielding for an electrostatic analyzer. This occurs when a significant number of charged particles around a charged surface effectively shield the potential from the rest of the plasma. Electrons are more mobile than the massive ions; therefore as the electron density is increased, the shielding of the charged surface increases. Debye shielding decreases with increasing electron temperature, since without thermal agitation, the charge cloud collapses to an infinitely thin layer.⁸¹ The Debye length λ_D , is the length at which the difference between the plasma potential and a point charge immersed in the plasma is decreased by a factor of $1/e$. At a distance greater than approximately $10\lambda_D$, the point charge can be considered insulated. The Debye length is defined in Equation 3-1 with the units of each term in brackets:

$$\lambda_D = 7430 \left(\frac{kT_e}{n} \right)^{1/2} \text{ [m], } kT \text{ in [eV], } n \text{ in [m}^{-3}] \quad \text{Eqn. 3-1}$$

The plasma density is represented with n when quasineutrality (i.e., electrons and ions have approximately the same density) is obeyed. For the plume plasma described one meter downstream the P5 Hall thruster, the Debye lengths range from 0.03 – 0.15 mm, corresponding with effective shielding distances of 0.3 – 1.5 mm, respectively. This indicates the plate separation for an electrostatic analyzer should be on the order of a millimeter or less for the effective creation of a constant electric field between the plates. This problem can also be alleviated with the artificial decrease in plasma density, thereby decreasing the Debye shielding (i.e., increasing the Debye length) around the plate. For particle-filtering analyzers, collimated entrance slits and/or meshes in front of the entrance can significantly decrease the electron and ion densities while maintaining the overall energy profile of the plasma to be measured. A decrease in the plasma number density by an order of magnitude, for the above example, increases the effective shielding distances from 0.95 – 4.7 mm. This method is usually employed, since most electrostatic analyzers are utilized to measure energy distributions and not absolute electron/ion number densities for Hall thruster plume.

3.1.4 Arcing Considerations

Although the previous section suggests a smaller spacing between plates limits Debye shielding effects, arc discharges can also prevent the plates from being electrically isolated from each other. For large electric potentials, electrons can “jump” from one biased plate to another creating an arc discharge. The Paschen curve describes the conditions for which this happens, and it is related to the ambient pressure and the electric field between the plates. The Paschen curves for xenon, krypton, and air yield minimum electric fields for arcing to occur at potentials of 260 V, 205 V, and 350 V,

respectively, when the product of the plate spacing and pressure ($p \times d$) is between approximately 0.45 – 0.75 Torr-cm.⁸² For a 1 mm gap spacing between electrodes, this computes to a minimum voltage for the three gases at 20.5 V. However, Hall thrusters generally operate in testing conditions below 10^{-5} Torr, and therefore the mean-free path of particles (on the order of meters) is significantly larger than the plate spacing. Electrons are likely to cross the gap without collisions. The biased plates therefore effectively exhibit vacuum-like conditions for arcing, and electric fields of several thousand V/mm can be sustained for each of the gases at this low pressure.⁸³

3.1.5 Summary of Design Requirements

Table 3-2 describes a summary of the design requirements for TOPAZ. Included is the motivation for each of the design parameters.

Design Parameter	Design Requirements	Motivation
Energy Range	0 – 15 keV	<ul style="list-style-type: none"> • Characterization of multiply-charged beam ions for high-power/I_{sp} engines as well as low-energy CEX ions
Energy Resolution	1.5 %	<ul style="list-style-type: none"> • Accurate E/q profile desired • Capability is already available with other types of analyzers
Field-of-View	$360^\circ \times 30^\circ$ (azimuthal \times elevation)	<ul style="list-style-type: none"> • “Imaging” of entire thruster • Maximum utilization of axisymmetric geometry (about the azimuthal angle)
Angular Resolution	$2^\circ \times 2^\circ$	<ul style="list-style-type: none"> • Differentiation of ions emanating from different parts of the thruster
High-Density Plasma Capability	Measurements with $n \approx 10^{15} - 10^{16} \text{ m}^{-3}$ → Small Plate Spacing	<ul style="list-style-type: none"> • Typical far-field plume density of mid-power Hall thrusters is much higher than space plasmas

Table 3-2: The design parameters and requirements for TOPAZ and the motivation for each.

With knowledge of the design requirements, a preliminary design for TOPAZ is possible through theoretical calculations and simulations to meet those requirements. The

following sections first describe the theory of operation for the instrument, and then a description of the computational simulation of the instrument through SIMION follows.

3.2 Theory of Operation

The top hat analyzer utilizes a radial electric field to guide ions through a spherical shell-shaped channel between a grounded plate and a negatively-charged deflection plate. Figure 3-2 illustrates a quarter cut-away view of the top hat analyzer with a typical ion trajectory.

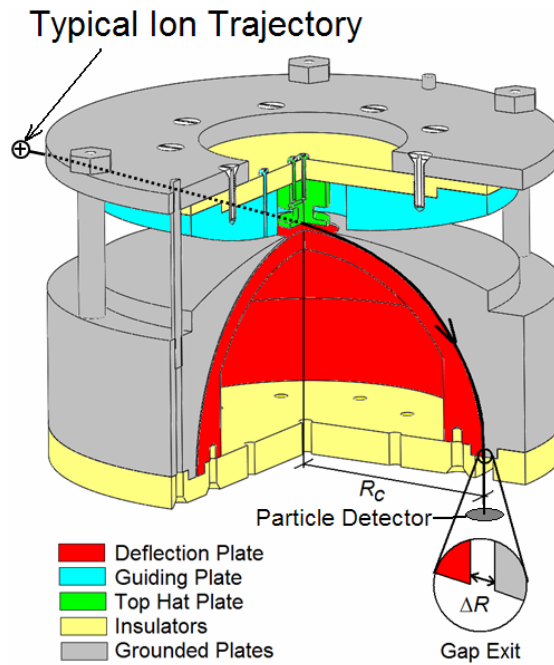


Figure 3-2: A cut-away view of the major components of the top hat analyzer with a typical ion trajectory.

The nomenclature described in the Figure 3-2 will be employed throughout the rest of this dissertation. As mentioned in Chapter 1, the elevation (vertical) angle of ions is selected by the guiding plate (turquoise). The energy-per-charge is selected by the field between the outside grounded plate (grey) and the inner deflection plate (red). The

particle's azimuthal (horizontal) angle is selected by the position of the detector underneath the analyzer. The combination of two angles and an energy-per-charge measurement, allows for the instrument to take a "snapshot" of ions of ion at a particular energy-per-charge within the field-of-view of the instrument.

Figure 3-3 displays the key dimensions and plates for a top hat analyzer utilized for the formulation of the theory.

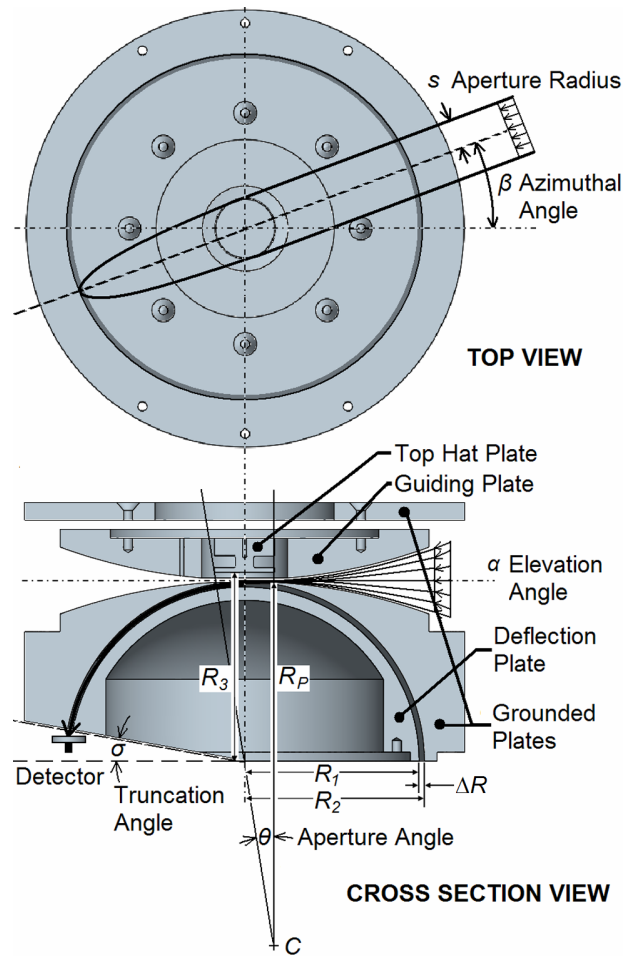


Figure 3-3: Principle design parameters for a top hat analyzer.

3.2.1 Analyzer Constant

The most important criterion for the instruments design is the analyzer constant K . This is defined as the ratio of the channel radius R_C to the channel size ΔR ($\Delta R = R_2 - R_1$) for the top hat analyzer:

$$K \equiv \frac{R_C}{\Delta R} \quad \text{Eqn. 3-2}$$

The channel radius R_C is simply the average of the inner and outer surface radii for gap. The analyzer constant is related to the energy- and elevation angle-to-voltage ratios, energy resolution, and selectivity of the instrument. The energy-to-voltage ratio is determined by equating the applied force required to turn a particle at the channel radius with the electric field generated in the gap. When the gap distance is small with respect to the turning radius (i.e., the analyzer constant is $K \gg 1$), the electric field can be assumed to be uniform between the deflection plate and grounded plate. Equation 3-3 displays the simple relationship between the deflection plate voltage V_D , the analyzer constant, and the expected energy-per-charge E/q (in units of eV/q) to be measured:

$$\frac{E}{q} = -\frac{KV_D}{2} \quad \text{Eqn. 3-3}$$

The inner deflection plate radius R_I is held to a negative plate potential V_D to detect positively-charged ions, while the outer radius is kept at ground potential. The linear correlation between the deflection plate voltage and energy-per-charge being measured indicates that there is no lower bound for the energy range. For higher energies, a high analyzer constant is desired, since the biased deflection plate voltage will remain fairly low, however, accurate DC power supplies are required to maintain the energy resolution throughout the energy range.

The top hat plate is usually held at ground but can be biased to increase or decrease transmissivity if needed. This plate functions as a gating plate for time-of-flight measurements through the instrument (discussed in Chapter 5). A maximum ratio of detectable ions to incoming ions (transmissivity) is realized when the top hat radius R_3 is larger than the deflection plate radius R_I by twice the gap distance (i.e., $R_3=R_I+2\Delta R$).⁸⁴ This distance yields an electric field over the aperture that is half that of the electric field in the channel. Hence, the particle travels with a radius R_p (with the center marked as point C in Figure 3) of approximately twice the normal channel radius over the aperture between the top hat plate and the deflection plate.

3.2.2 Guiding Plate Design

Guiding plates (also known as steering plates), which can vary either positively or negatively in plate potential, allow for variance in the vertical angular direction (elevation angle α) for the measured ions. Ions coming from the selected elevation angle are guided into the top hat region with a horizontal trajectory. The guiding plate radius of curvature is determined by setting the outer entrance angle of the surface slightly higher than the desired maximum-elevation angle α_{max} within the field-of-view. This angle is mirrored on the lower grounded plate surface. Through simple trigonometry, the guiding plate radius R_G is related to the channel radius R_C if the entrance to the instrument is aligned vertically with the exit of the channel:

$$R_G = \frac{R_C}{\sin \alpha_{max}} \quad \text{Eqn. 3-4}$$

For larger elevation-angle field-of-views, a smaller guiding plate radius is required; however, this increases the overall height of the instrument.

3.2.3 Aperture Size

Particles enter the top hat aperture and are turned at a radius R_p due to the electric field generated between R_3 and R_1 . As mentioned previously, the electric field is approximately half that of the gap; therefore, R_p is approximately $2R_2$. The center of curvature for the particles is at point C (see Figure 3-3). To determine the optimum aperture angle θ , the “grazing” trajectory of a particle is followed that touches the front lip of the top hat plate and follows the outer radius of the gap. The particle travels at a radius of $2R_2$ due to the field generated between the top hat plate and the deflection plate, and is “pushed” towards point C by ΔR across the aperture. Through construction of a right triangle between point C and the top hat entrance lip and the outer gap radius (holding the right angle), the optimum aperture angle θ can be derived:

$$\cos \theta = \frac{2R_2 - \Delta R}{R_p} \quad \text{Eqn. 3-5}$$

Since $R_p \approx 2R_C$ and $R_2 \approx R_C$ the aperture angle can be rewritten as a function of the analyzer constant through Equation 3-2:

$$\cos \theta \approx 1 - \frac{1}{2K} \quad \text{Eqn. 3-6}$$

Through a two-term Taylor expansion of the cosine function, the aperture angle is directly correlated with the analyzer constant for $\theta < 15^\circ$:

$$\cos \theta = 1 - \frac{1}{2}\theta^2 \dots \quad \text{Eqn. 3-7}$$

Therefore, the ideal aperture angle (in radians) is proportional to the inverse square root of the analyzer constant:

$$\theta \approx \sqrt{\frac{1}{K}} \quad \text{Eqn. 3-8}$$

The ideal aperture radius s is therefore:

$$s = R_c \sin\left(\sqrt{\frac{1}{K}}\right) \quad \text{Eqn. 3-9}$$

The optimum truncation angle σ for ion focusing at the detector is $\approx \theta/2$.⁸⁴ As the analyzer constant is increased (above 50), this value becomes small and can be ignored. Ions entering over the aperture diameter $2s$ are focused at the exit of the gap while maintaining their entrance azimuthal angle β (shown in the top view of Figure 3-3).

3.2.4 Geometric Factor

The geometric factor describes the total acceptance of the instrument in velocity space volume.⁸⁴ This parameter can be thought of the integration of the instrument's instantaneous effective collection area, energy resolution, and angular resolutions. Since the top hat analyzer is very similar to the quadrispherical analyzer, a similar formulation can be utilized for determining the sensitivity of the top hat analyzer. A derivation of the product of the velocity-per-charge and elevation angle acceptances for the quadrispherical analyzer is as follows:⁸⁵

$$\left\langle \frac{dv}{v} d\alpha \right\rangle = \frac{1}{4} \left(\frac{\Delta R}{R_1} \right)^2 \csc^3\left(\frac{90-\sigma}{2}\right) \left(\frac{7}{8} + \cos\left(\frac{90-\sigma}{2}\right) \right) \quad \text{Eqn. 3-10}$$

The angled brackets indicate the term is an overall weighted average over the velocity and elevation angle parameters. With the assumption that the approximate aperture area (collection area) is approximately 2/3 of the projected aperture area, and since the “energy” geometric factor $G(E)$ is twice the “velocity” geometric factor $G(v)$, the following estimation of the geometric factor (in terms of energy) is produced assuming the full 360° (or 2π rad) azimuthal field of view is utilized:⁸⁴

$$G(E) = (2\pi) \left(\frac{2}{3} R_1 \cdot 2\theta \cdot \Delta R \right) \left(2 \left\langle \frac{dv}{v} d\alpha \right\rangle \right) \quad \text{Eqn. 3-11}$$

The units for the geometric factor $G(E)$ in the above equation are $\text{cm}^2 \text{ sr eV/eV}$ if R_1 and ΔR are given in centimeters. The use of the seemingly redundant units of eV/eV indicates the term is a product of the energy resolution ($\Delta E/E$) and therefore the energy geometric factor. Equation 3-11 can be written in terms of only the analyzer constant for the ideal top hat analyzer by combining Equations 3-2, 3-8, 3-10, and 3-11, and assuming $R_1 \approx R_C$:

$$G(E) \approx \frac{4\pi}{3} \left(\frac{R_C^2}{K^{3.5}} \right) \csc^3 \left(45 - \frac{1}{4\sqrt{K}} \right) \left(\frac{7}{8} + \cos \left(45 - \frac{1}{4\sqrt{K}} \right) \right) \quad \text{Eqn. 3-12}$$

This slightly unwieldy function can be reduced for large analyzer constants by approximating the trigonometric factors, and simplifying the numerical constants:

$$G(E) \approx \frac{18.74 R_C^2}{K^{3.5}} \quad \text{Eqn. 3-13}$$

Equation 3-13 shows that the sensitivity of the instrument is highly dependent on the analyzer constant. Top hat analyzers with a small gap size over a large radius tend to act as very selective filterers. A top hat analyzer with an analyzer constant of 80, for example, will accept less than a hundredth of the ions a top hat with an analyzer constant of 20 transmits if they were both had the same size channel radius.

The above formulation provided the general basis for an analytical attack of the design of TOPAZ to meet the design requirements. Only an approximate response can be estimated, since nonlinear surfaces and fringe effects from structural constraints are difficult to model analytically. SIMION, an ion optics program, allowed for a more detailed design and characterization of TOPAZ to be determined.

3.3 Design of TOPAZ through SIMION

SIMION is a commercial computer program that is capable of modeling ion optics with electrostatic and/or magnetic potential arrays. For the purposes of TOPAZ, only electrostatic fields were modeled. First, a model of TOPAZ was defined through a geometry file that included the volume definitions and potentials of the instrument. TOPAZ was assumed to be cylindrically symmetric through the eyes of SIMION. The electric potential ϕ is solved for around the instrument through the Laplace equation (Equation 3-14). SIMION assumes a zero-charge volume density (i.e., no space charge).⁸⁶

$$\nabla^2 \phi = 0 \qquad \text{Eqn. 3-14}$$

An important property of this equation is the scalability of solutions for ϕ . Since the Laplacian operator satisfies homogeneity (i.e., $f(ab)=a \cdot f(b)$), solutions can be found for a particular potential field and scaled if *all* plate voltages are scaled accordingly. This significantly reduces the required number of simulations.

Over-relaxation, a finite difference technique, was used as the iterative process to converge on the electric potential field solution. After the potential field has been determined, ion trajectories are modeled by determining the electrostatic acceleration on the particle. SIMION incorporates a standard fourth-order Runge-Kutta method for integrating out the ion's trajectory.

3.3.1 Description of the Model

In determining the optimal design for TOPAZ, several configurations with differing analyzer constants were simulated. The deflection plate design was determined first, and then the guiding and top hat plates were added to the model. Finally, the top

grounded plate was placed to match a Pro/ENGINEER model structural constraint and help contain the applied electric field within the instrument. Figure 3-4 displays the initial and final models of TOPAZ in SIMION for modeling its properties.

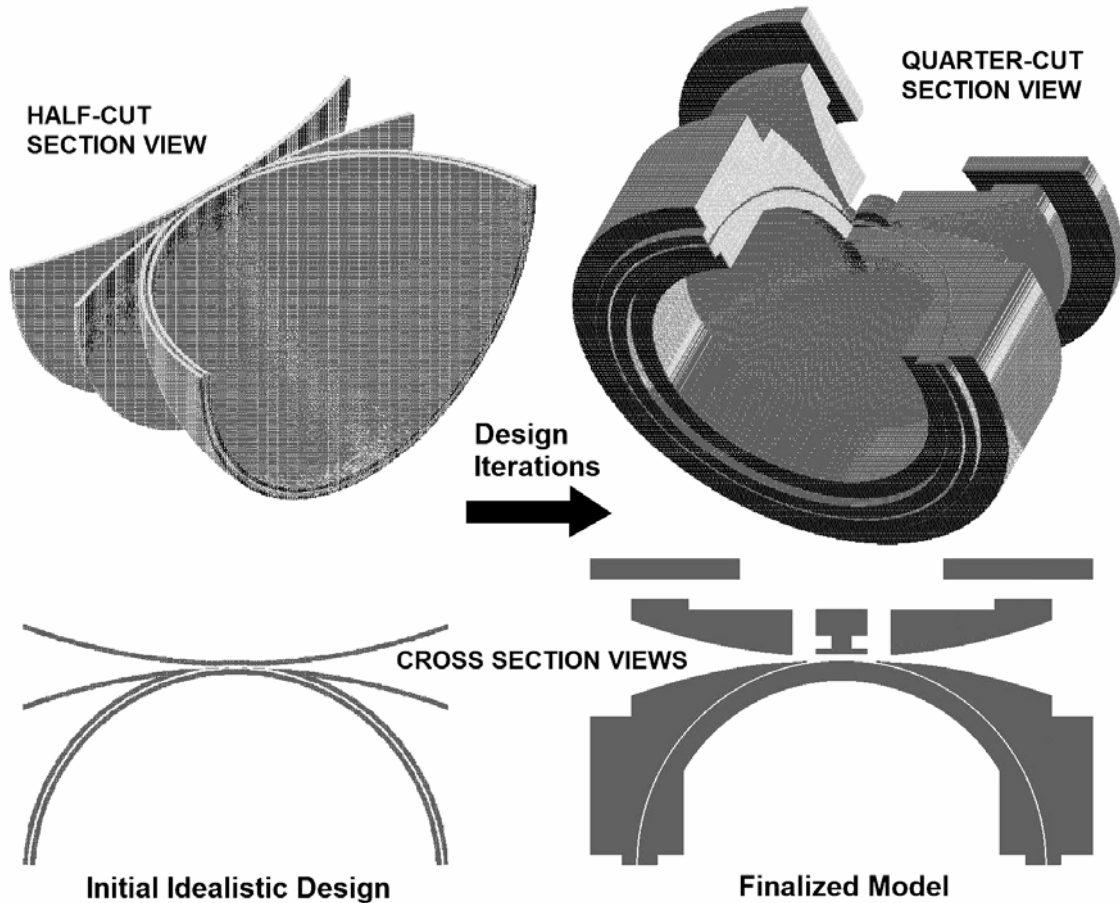


Figure 3-4: A comparison of the initial and final designs of TOPAZ in SIMION.

Over 1×10^6 ion trajectories were simulated to “fly” into the instrument to determine the instrument’s response for each configuration.

3.3.2 Energy Resolution

Monte-Carlo simulations of ions entering the instrument allowed for the distribution of detected ions to be determined as a function of the plate potentials. Since

the electrostatic analyzer discriminates energy-per-charge, singly-charged ions with a distribution of energies were flown through TOPAZ.

The energy resolution is defined as the full-width half-maximum (FWHM) of the profile normalized by the average energy of the detected ions. The width of the profile is determined as the difference in energy between the two points about the peak counts for which half of the maximum number counts were recorded. Several configurations with varying analyzer constants were simulated to establish the effect on energy resolution. A channel radius of 10 cm was chosen for TOPAZ, and the gap distance was varied from 1 – 3 mm. The theorized energy resolution is inversely proportional to the analyzer constant:⁸⁷

$$\frac{\Delta E}{E} \approx \frac{C_K}{K} \quad \text{Eqn. 3-15}$$

Through use of a least-squares fit, a proportionality constant C_K of 2.352 for TOPAZ was determined. Figure 3-5 displays a plot of the energy resolution versus the analyzer constant.

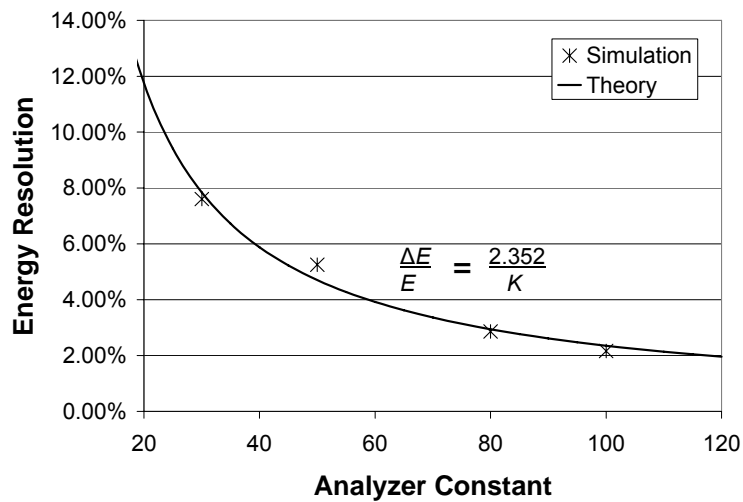


Figure 3-5: Energy Resolution as a function of the analyzer constant for multiple TOPAZ designs.

The energy resolution increases for increasing analyzer constants (i.e., decreasing gap distances); however the change is not appreciable for analyzer constants above 100. The original design requirement of an energy resolution of 1.5% requires an analyzer constant of approximately 157. For this value of K and a channel radius of 10 cm, a gap distance of 0.638 mm is required. Since this gap distance must provide a uniform electric field across the entire length of the channel, the construction of this configuration for TOPAZ is a fairly difficult task. Another idea is to increase the channel radius to 15.7 cm, but maintain the 1 mm gap distance. This would put make the instruments channel diameter over 30 cm, resulting in a large electrostatic analyzer. A final solution is to relinquish the energy resolution requirement of 1.5%. This would allow for a smaller instrument with a larger, constructible gap size.

A 5% or lower energy resolution was considered acceptable for the TOPAZ. An overall instrument size of approximately 20 cm was considered typical for electrostatic analyzers. The instrument size was assumed to be approximately twice the channel radius R_G . With a gap distance greater than or equal to 1 mm, the instrument's construction would be feasible. These design constraints (boundaries) provided an enclosure for the design space of the physical dimensions for TOPAZ. Figure 3-6 displays this plot utilizing the theoretical curve from Figure 3-5, and the design constraints are outlined.

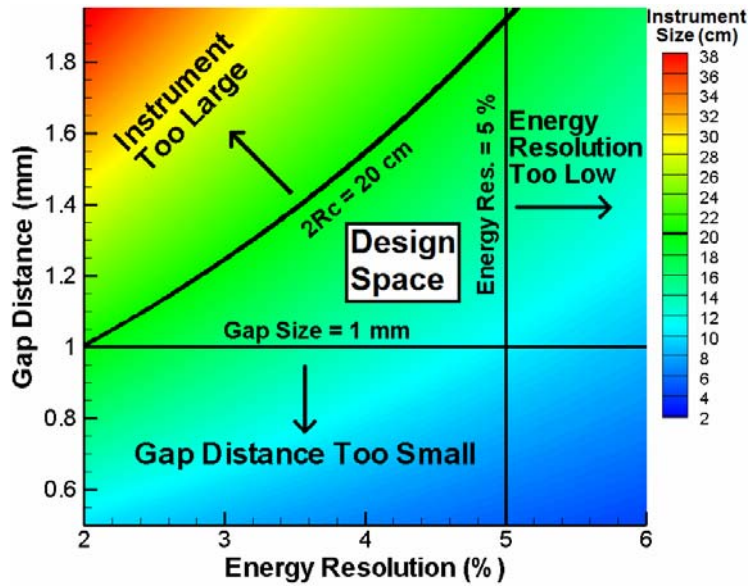


Figure 3-6: A graph of the design space for TOPAZ which satisfies the design constraints.

Ideally, if the design space is equally constructible, the maximum performance is realized with a gap distance ΔR equal to 1 mm and a channel length R_C equal to 10 cm, yielding an analyzer constant of 100 with an energy resolution of approximately 2%. The predicted geometric factor is $1.874 \times 10^{-4} \text{ cm}^2 \text{ sr eV/eV}$ from Equation 3-13. This was chosen as the design point of TOPAZ, as it also minimizes possible Debye shielding effects of high-density plasmas mentioned previously.

3.3.3 Top Hat Design

The top hat plate sits above the aperture and controls the electric field before ions enter into the channel, but after their elevation angle has been selected. Presumably, ions arrive with approximately parallel trajectories to the deflection plate and top hat surfaces. For an analyzer constant $K = 100$, the ideal aperture angle θ is calculated to be 5.7° (0.1 rad) through Equation 3-8. This coincides with an aperture diameter $2s$ of 2.00 cm (see top view of Figure 3-3).

As mentioned previously, the optimum distance between the top hat plate and the deflection plate is $2\Delta R$. If the top hat plate is grounded, the electric field produced is half that between the deflection plate and the grounded outer shell. However, for high analyzer constants, the three plate surfaces – the deflection plate, grounded outer shell, and top hat plate – must be placed within a millimeter of each other. Since a finite thickness for the edge of the aperture on the grounded must exist, the ideal design must be modified, since the grounded plate edge comes precariously close to the top hat plate.

To alleviate this concern, the aperture size can be increased, and the top hat plate can be moved further away from the deflection plate. This effectively decreases the electric field produced, however the ion travels over a larger distance across the aperture and has the same overall trajectory-change into the channel. A larger top hat plate decreases (and can eventually prevent) the horizontal transmission of ions into the aperture, since it should follow the curvature of the deflection plate to maintain the constant electric field across the aperture. To prevent this from occurring, the top hat plate diameter can be decreased, however, the plate must be biased positively, to generate a larger electric field over a shorter distance.

A combination of the above approaches was utilized to solve the proximity problem of the three plates for TOPAZ.

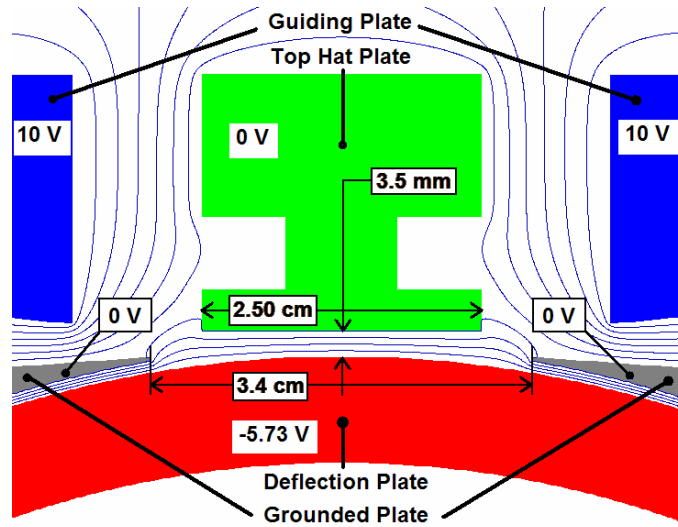


Figure 3-7: Top hat region detail, and electric potential lines for a typical operating condition of TOPAZ detecting 275 eV ions from 10° below the horizontal plane.

The top hat plate was raised from the ideal 2.0 mm ($2\Delta R$) to 3.5 mm from the deflection plate, and the aperture diameter $2s$ was increased from the optimal 2 cm ($\theta = 5.72^\circ$) to 3.4 cm ($\theta = 9.60^\circ$). Since the top hat plate covers a small angle of curvature over the deflection plate, a flat surface was utilized instead of a curved surface (as shown in Figure 1-6 of Chapter 1) since machining of the part was simpler, and the non-linearity in the electric field under the top hat plate had a negligible effect on the ions trajectory. An approximate optimal voltage for transmission under the top hat plate is created when the product of the electric field and aperture distance $2s$ is matched the ideal top hat analyzer. Using the geometry in Figure 3-7, the top hat plate must be biased positively by 1.38 times the deflection plate voltage. This optimal voltage is shown to be approximately true through simulation and experiment in the next chapter. Use of the optimal voltage is not required for the top hat plate, as a significant percentage of the maximum transmission is realized with a grounded top hat plate.

3.3.4 Guiding Plate Design

The original design requirement for the elevation-angle field-of-view was $\pm 15^\circ$ yielding a total range of 30° . Due to the possible fringe effects, the guiding plate was designed for a field-of-view of $\pm 20^\circ$, allowing for the original requirement to be well within the new range. The entrance lip of the guiding plate for TOPAZ was aligned with the top hat radius R_3 (10.3 cm) which is slightly larger than the channel radius R_C (10.05 cm). Utilizing Equation 3-4 with the top hat radius R_3 yields a guiding plate radius of 30.115 cm. The guiding plate is placed at a height, such that if the surface was continued over the aperture, the point intersecting the azimuthal axis of symmetry would coincide with the top hat plate intersection of the axis. This allows for the majority of ion transmission from the guiding plate region into the aperture region regardless of the elevation angle being selected.

3.3.5 Grounded Cover Plate and Outer Shell

A grounded cover plate is placed on top of the instrument for structural support of the top portion of the instrument and to prevent electric field lines from permeating from the instrument. The radius is matched with the size of the grounded outer shell, and structural stands (not modeled in SIMION) provide the required separation between the grounded outer shell and guiding plate, as well as the top hat plate and deflection plate. The guiding plate radius of curvature is mirrored on the grounded outer shell. This provides a uniform electric field for the elevation-angle selection of ions into the aperture.

3.3.6 Summary of Physical Characteristics of TOPAZ

The physical characteristics of the SIMION model of TOPAZ are summarized in

Table 3-3.

Parameter	Value
Analyzer Constant K	100
Inner Gap Radius R_1	9.95 cm
Outer Gap Radius R_2	10.05 cm
Top Hat Plate Distance (along centerline) R_3	10.30 cm
Gap Distance ΔR	1.0 mm
Total Instrument Size (diameter)	24.6 cm
Guiding Plate Radius R_G	30.115 cm
Aperture Angle θ	9.60°
Aperture radius s	1.70 cm
Geometric Factor $G(E)$	$1.874 \times 10^{-4} \text{ cm}^2 \text{ sr eV/eV}$

Table 3-3: Physical characteristics of the SIMION model of TOPAZ.

3.4 Pro/ENGINEER Model of TOPAZ

Although SIMION provides an excellent model of the electrostatics of TOPAZ, a computer-aided design (CAD) program is required to add the structural constraints which hold all the parts together. Pro/ENGINEER provided an excellent resource for designing the additional structural parts which maintain the channel size and radius, top hat plate and guiding plate positions, and mounting holes for the instruments installation onto other structures. Pro/ENGINEER was used in conjunction with SIMION to design TOPAZ. As the design was changed in Pro/ENGINEER, the SIMION model was updated to match the latest model of the instrument. Figure 3-8 displays the design process of the TOPAZ to its creation.

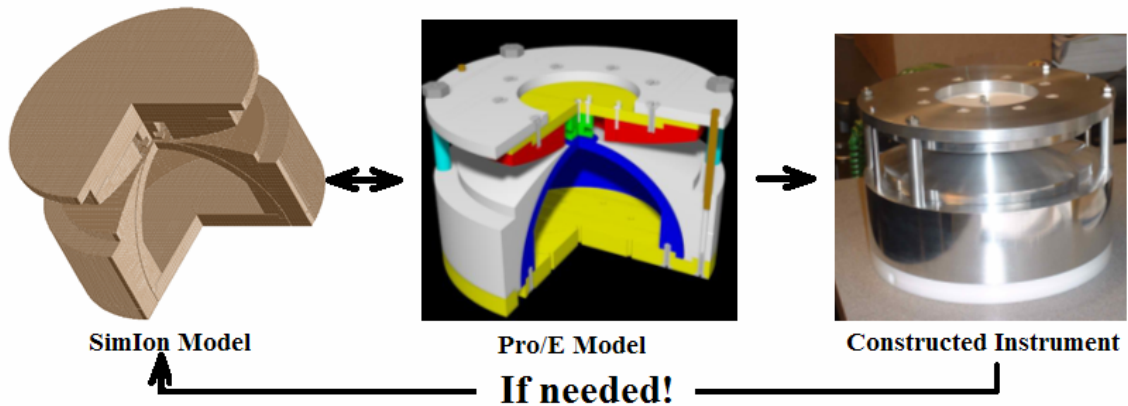


Figure 3-8: Design process (from left to right) of TOPAZ.

The SIMION and Pro/ENGINEER model were updated concurrently. After the instrument's construction, additional analysis was conducted in SIMION in case the instrument was not properly functioning, and a part had to be modified. An example of this was the concern of the analyzer constant being too high resulting in too few ions being detected. As a precaution, simulations through SIMION were conducted for a deflection plate with a 2 mm decrease in the radius (97.5 mm versus the original 99.5) resulting in an analyzer constant of 33 instead of 100. This increases the sensitivity of the instrument by approximately an order of magnitude while keeping the instruments operation virtually the same (with the deflection plate voltage needing to be tripled) and requiring the modification of only one part.

To position the deflection plate and grounded outer shell with the required 1 mm gap distance, an insulator is utilized with precisely-machined ledges to separate the parts. Figure 3-9 displays a view of the base plate.

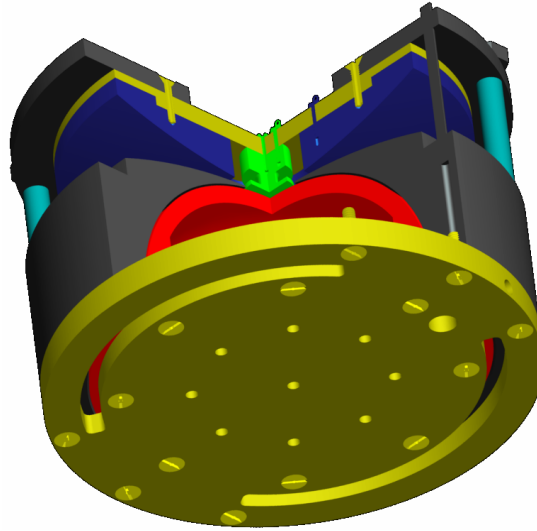


Figure 3-9: Bottom view showing base plate detail of the Pro/ENGINEER model of TOPAZ with a quarter cut-away section.

The base plate contains 120° azimuthal slots for ion detection. This prevents TOPAZ from utilizing the full 360° field-of-view in this direction, and is not modeled in SIMION; however this constraint does not limit the instrument's view of a thruster in the far-field plume. The top hat and guiding plates are accurately positioned vertically with respect to the grounded outer shell and aperture through the use of four sleeves (two shown in turquoise in Figure 3-9) which surround dowel pins that control the horizontal position of the top half of TOPAZ. Several mounting holes are added to the base plate, and nylon screws connect the biased deflection plate and grounded outer plate to the base insulator.

3.5 TOPAZ Performance Characterization through SIMION

As mentioned previously, the nature of the Laplace equation for the potential field allows for solutions to be scaled with plate potentials. The potential ϕ at every point can be multiplied by a constant yielding another solution to a new set of plate potentials. This

allows for significantly less computation, as simulations can be run for a specific energy range of ions, and the ion trajectories remain the same if the plate potentials are scaled accordingly.

For each simulation $10^5 - 10^7$ ions were flown towards TOPAZ with varying velocities (and hence energies), elevation angles, and positions to cover the entire entrance aperture. Since the model of TOPAZ is symmetric about the centerline in the azimuthal direction, the azimuthal angle is not varied. Each of the ion initial angles and velocities in each direction were recorded if it made it to the exit of the gap (i.e., to the detector). Distributions of these properties were created to determine what type of ions TOPAZ detected for a specific plate setting.

3.5.1 Geometric Factor

The “energy” geometric factor $G(E)$ is fairly easy to compute. By taking a product of the ranges of parameters varied in the SIMION simulation, and multiplying this by the fraction of ions detected, an estimation of the overall sensitivity is created. This Monte-Carlo technique effectively “integrates” the analyzer’s gathering power over each of the parameters varied.⁸⁸ Equation 3-17 describes the equation utilized to estimate the geometric factor:

$$G(E) = \left(\frac{\# \text{ successful trajectories}}{\# \text{ total ions flown}} \right) \left(\frac{1}{2} \right) (2\pi) (\sin(\alpha_{\max}) - \sin(\alpha_{\min})) \left(\frac{\Delta E}{E_{\text{avg}}} \right) (\Delta x \Delta y)$$

Eqn. 3-16

The first factor represents the fraction of ions detected from the simulation. This value ranged from 0.04 – 0.1%. Therefore, in order to characterize the detected ions, approximately 10^5 - 10^6 ions must be simulated to determine average values, while 10^6 - 10^7

ions must be flown to create distributions of detected ions. The factor of $\frac{1}{2}$ in Equation 3-16 describes the cosine-losses of a particle flux on the instrument's effective detector surface. A derivation of this is found in a paper by Sullivan.⁸⁹ The next factor of 2π represents the full azimuthal field-of-view (360°) – a parameter not varied in the simulation. This factor “converts” the 2-D response from the simulation into the equivalent 3-D response. The product then must be multiplied by the difference of the sine of the maximum and minimum elevation angles simulated. The elevation angle functions as the polar angle in spherical coordinates and therefore, is “projected” onto the collection area through the sine function (based on the definition of the horizontal being 0°). The final two factors respectively signify the energy range, normalized with the average energy detected and the area for which ions are flown in front of the instrument covering the effective collection area.

Utilizing Equation 3-16 yields a geometric factor of $2.23 \times 10^{-4} \text{ cm}^2 \text{ sr eV/eV}$ for the grounded guiding and top hat plates setting. This is slightly higher than the theoretical value derived previously ($1.874 \times 10^{-4} \text{ cm}^2 \text{ sr eV/eV}$); however, this is to be expected since the aperture diameter $2s$ was increased from the ideal value of 2 cm to 3.4 cm. This increases the effective collecting area of the instrument which is directly correlated with the geometric factor.

The geometric factor for TOPAZ is relatively low as compared with other instruments. Normalization with the square of the channel radius allows for effective comparison with differently sized analyzers. For TOPAZ, $G(E)/R_C^2$ is equal to $2.23 \times 10^{-6} \text{ sr eV/eV}$. For the Miniaturized Optimized Smart Sensor (MOSS), a torroidal analyzer, the normalized geometric factor is $5.5 \times 10^{-3} \text{ sr eV/eV}$.⁸⁷ The Cassini Plasma Spectrometer

(CAPS), a top hat analyzer, has a normalized geometric factor of 8.13×10^{-4} sr eV/eV.⁹⁰

The low sensitivity of TOPAZ is due to the high analyzer constant which increases the angular- and energy-discriminations to higher resolutions than both of these instruments.

3.5.2 Energy Correlation and Resolution

For simulations run on TOPAZ, the deflection plate potential was set to -300 V. Through Equation 3-3, this corresponds with the detection of 15 keV ions, and is the nominal ion energy to be detected by TOPAZ through the design requirements; however, since the plate potentials and ion energies can be scaled with deflection plate voltage, the chosen voltage is arbitrary. For determination of the energy resolution, the guiding and top hat plates were grounded, corresponding to a measurement of ions approximately along the horizontal plane ($\alpha \approx 0$). A total of 2082 ions flew through the instrument and exited the channel. The average energy of ions measured was 14,184 keV. Multiple simulations with varying energies and deflection plate voltages do not have to be run, due to the scalability of the Laplace equation. Since the deflection plate voltage (-300 V) is directly related to the energy measured (from Equation 3-3), the relationship is accurately revealed:

$$\frac{E}{q} = -47.28V_D \quad \text{Eqn. 3-17}$$

The expected coefficient of $K/2 = 50$ is slightly higher than the simulation results. This is due to the one dimensional assumption in Equation 3-3. In reality potential field between the deflection plate and grounded outer shell is slightly “stretched,” since the surface area of the biased-inner deflection plate is slightly less than the grounded outer

shell. This results in a lower electric field than predicted, and a higher-deflection plate voltage is required to measure a specific energy-to-charge.

A distribution of the ion energy is displayed in Figure 3-10.

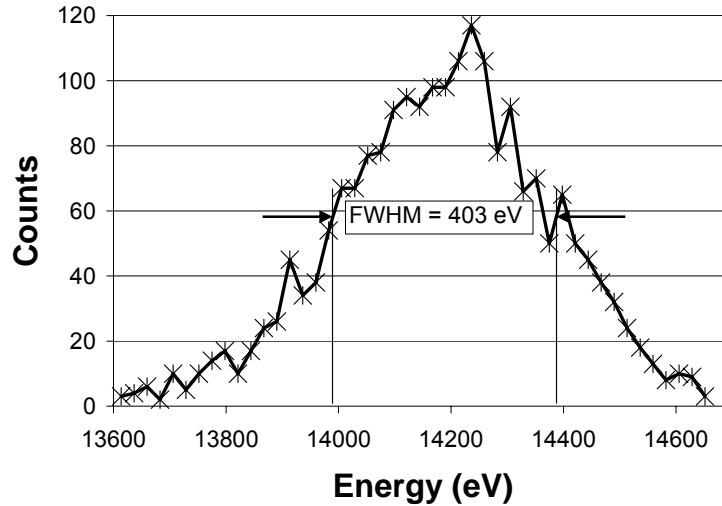


Figure 3-10: Energy distribution for $V_D = -300$ V and $V_G = 0$ V. Note: x -axis has been enlarged to show distribution detail.

The full-width half-maximum (FWHM) of the energy distribution is 403 eV. The energy resolution for TOPAZ is defined as the FWHM divided by the average energy and is computationally determined through SIMION as approximately 2.8%.

3.5.3 Elevation Angle Correlation and Resolution

In a similar manner as with the energy resolution, a distribution of the entrance elevation angles α yields the horizontal angular resolution. However, the assumption of the linear scaling of the guiding plate voltage V_G with the elevation angle α is not necessarily valid. Since the ratio of the guiding plate voltage to the deflection plate voltage determines the elevation angle being measured, multiple simulations must be run

for varying guiding plate potentials (thereby varying the ratio), and the average elevation angle must be correlated with the ratio.

3.5.3.1 Guiding Plate Voltage-Correlation with Elevation Angle

Figure 3-11 displays a plot of the average elevation angle measured by TOPAZ for varying ratios of guiding-to-deflection plate voltages. The ratio is negated, so that the ratio maintains the same sign as the deflection-plate voltage bias.

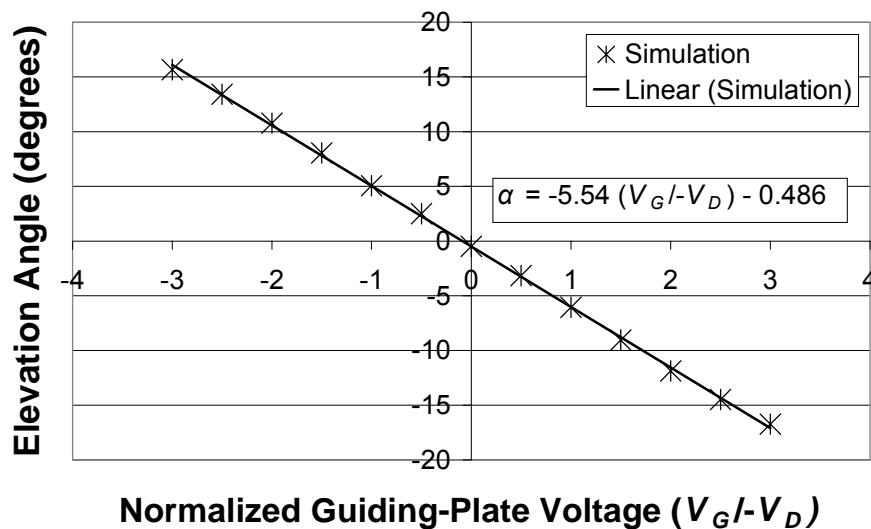


Figure 3-11: Correlation between the average elevation angle and the normalized guiding-plate voltage for TOPAZ.

For the above plot, the elevation angle is defined as positive if ions are detected from above the horizontal and negative from below. Ions were detected from -16.7° to $+15.7^\circ$ yielding a total demonstrated field-of-view of 32.4° . A very linear trend (R-squared value of 0.9995) exists between the normalized guiding-plate voltage and the average elevation angle. For the Wind 3D plasma instrument, a top hat analyzer designed for investigating the solar wind plasma, a similar linear relationship exists, and the slightly “s” shaped variance is also noticed.^{84,91} This is likely due to fringe effects of the

guiding plate, where the electric field is slightly larger near the surface. The proportionality constant (in units of $^{\circ}/(V_G/V_D)$), for this instrument is approximately double that of TOPAZ. This is due to the larger elevation-angle field-of-view, which requires further plate separation and therefore higher plate voltages to create similar electric fields.

3.5.3.2 Elevation Angle Resolution

The distribution of elevation angles selected by TOPAZ determines the angular resolution in the vertical direction for the instrument. Figure 3-12 displays the distribution.

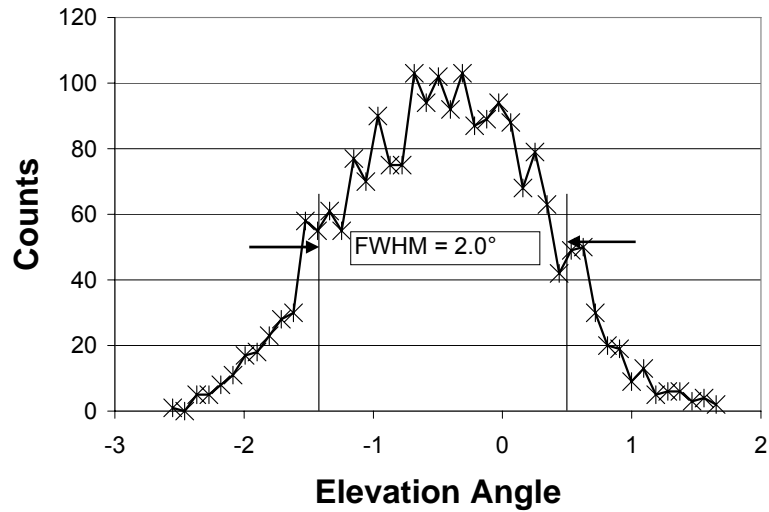


Figure 3-12: Elevation angle distribution for $V_D = -300$ V and $V_G = 0$ V.

The average angle measured for the detected ions is slightly below the horizontal at -0.486° . This corresponds with the y-intercept value for the guiding plate-elevation angle relationship. The elevation angle resolution is defined as the FWHM of the distribution, and is approximately 2.0° for TOPAZ.

3.5.3.3 Energy-Elevation Angle Response

A slight correlation exists for between the measured elevation angle and the energy of detected ions. This correlation has been noticed for several other top hat analyzers as well.^{74,77,84,92} Figure 3-13 displays a contour plot of the elevation angle versus the energy for a -300V deflection plate setting.

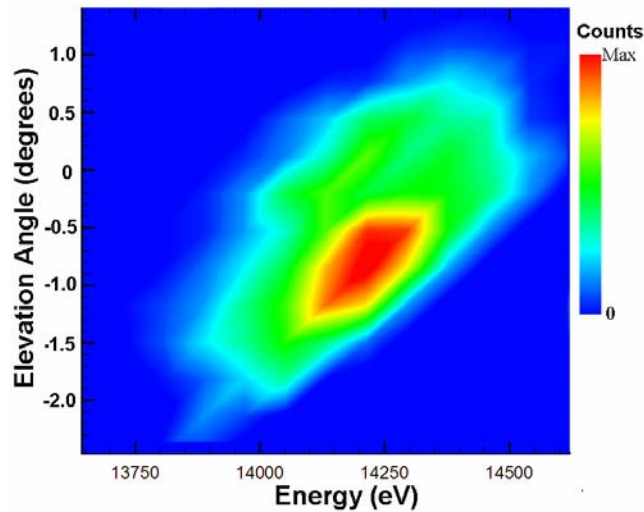


Figure 3-13: Elevation Angle-Energy relationship for a -300V deflection plate and grounded guiding plate setting.

Similar to previously referenced top hat analyzers, a positive relationship exists between the elevation angle and the energy measured. Since the correlation is within the resolution of each of these parameters, the relationship does not affect measurements among each of these parameters individually. The similar contour plot in Figure 3-13 is a testament to the similar characteristics TOPAZ shares with other top hat analyzers.

3.5.3.4 Guiding Plate Correlations with Other Parameters

A slight variation in the average energy measured by TOPAZ as a function of the guiding plate voltage exists. This correlation existed for the Wind 3D top hat analyzer as

well.⁹¹ Figure 3-14 shows the relationship between the average energy and normalized guiding-plate voltage.

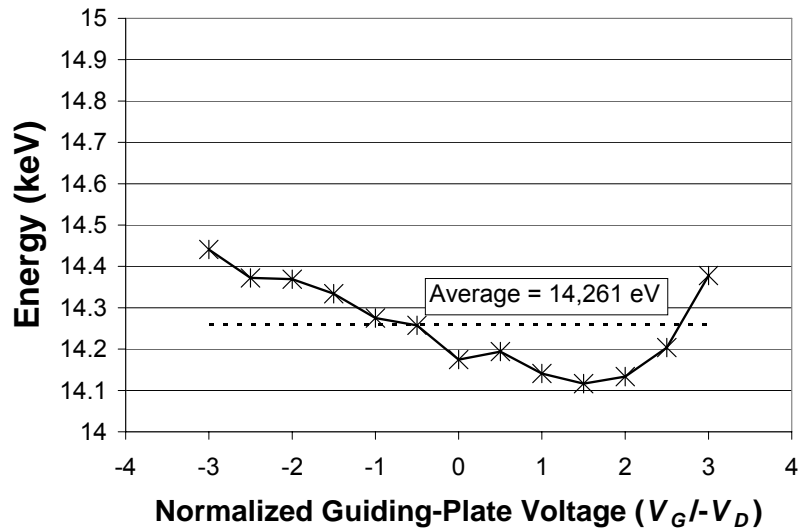


Figure 3-14: Average energy of detected ions as a function of the normalized guiding-plate voltage.

Since the average energy of ions detected does not vary more than the energy resolution of 2.8% over the range of guiding plate potentials, this relationship is considered negligible. Using average energy of 14,261 eV in Equation 3-16, requires changing the coefficient to 47.54; however, since the difference is within the energy resolution, the use of either value is valid.

3.5.3.5 Guiding Plate Voltage Effect on Geometric Factor

The equal transmission of ions through all elevation angles ensures accurate profiling in the vertical direction. The ion trajectory has the same shape across all azimuthal angles due to the axisymmetric geometry. However, ions entering TOPAZ with different elevation angles have significantly different paths to the aperture; therefore it is important that the transmission does not vary significantly across all elevation angles.

Figure 3-15 displays the geometric factor plotted against the normalized guiding-plate potential.

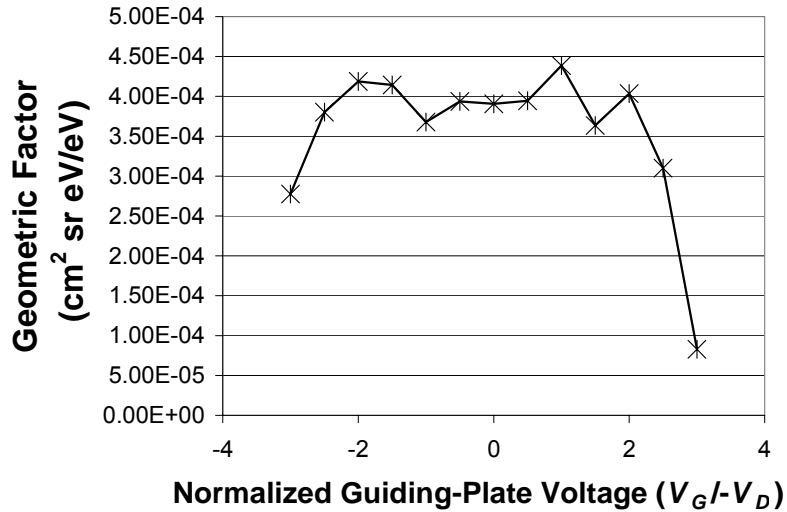


Figure 3-15: Geometric factor as a function of the normalized guiding-plate voltage.

For voltage ratios from -2.5 – 2.5, the geometric factor is relatively constant. Sharp decreases are seen at higher voltage ratios. This corresponds to an approximately constant transmission of ions for elevation angles of $-14.3^\circ - 13.4^\circ$. This is due to the physical presence of either the grounded outer shell or the guiding plate for the negative and positive angles, respectively. Ions traveling at trajectories with angles beyond the angular range skim these plates before entering into the aperture. This attenuates the elevation angle range (and possibly the energy range), thereby decreasing the geometric factor.

3.5.4 Estimation of Azimuthal Resolution

Since TOPAZ is azimuthally symmetric, the SIMION model incorporates a 360° field-of-view in the azimuthal direction. Although, the model incorporates no variation in the azimuthal direction, an estimation of the azimuthal angle resolution can be

determined by profiling the azimuthal-position variation at the exit of the gap. This describes the distribution (and hence maximum variation) of ions in the azimuthal direction at the detector with the precondition of all the ions having the same starting-entrance azimuthal angle.

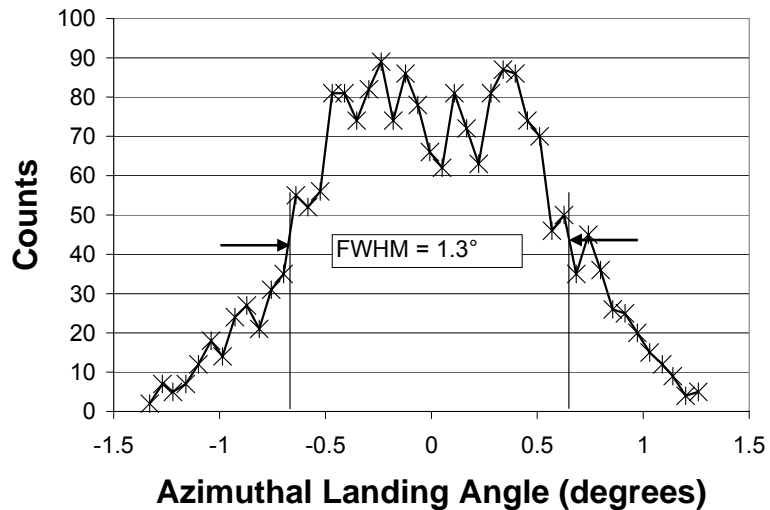


Figure 3-16: Profile of azimuthal landing angle of detected ions for $V_D = -300$ V and $V_G = 0$ V.

A slightly double peaked distribution for the azimuthal landing angle is evident for detected ions. Although this decreases the azimuthal angle resolution, the FWHM of 1.3° is within the original design requirement of 2° . The profile is approximately symmetric about 0° as expected, since the ions are flown across the aperture evenly; however the double-peak structure indicates a preference for the detection of ions at positions slightly off the centerline. Since the aperture diameter was increased in size from the ideal design and the ion truncation angle σ was assumed negligible (see Figure 3-3), the ions are not focused exactly on the detector. The azimuthal angle resolution represents the smallest discrimination of this dimension possible; however if the size of

the collector at the exit of the gap occupies a larger azimuthal range, the resolution is set by the detector size instead.

A look at the effective collection area of TOPAZ reveals that a larger amount of ions enter the aperture on the edges (i.e., at a greater distance than the ideal aperture radius) than on the aperture centerline.

3.5.5 Effective Collection Area

By profiling the entrance horizontal (x) and vertical (y) positions of detected ions, the effective “collection” area of the analyzer can be determined. Since the instrument’s detection of an ion is also a function of the energy and trajectory, the literal sense of a collection area detecting all ions (e.g., a Faraday Cup) is invalid. However, the effective collection area is useful for determining if a collimating entrance intersects with the possible entrance positions for ion detection. Figure 3-17 describes the distribution of the entrance position of ions with respect to TOPAZ.

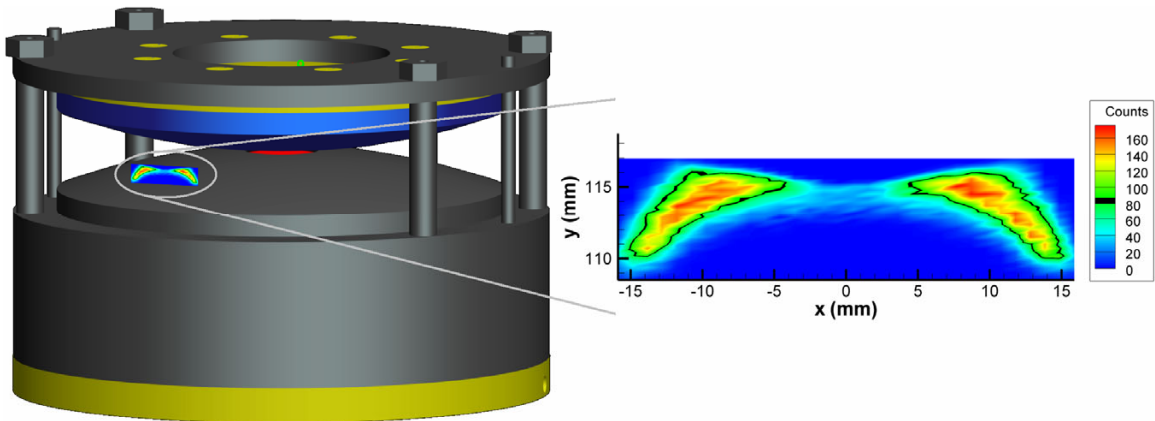


Figure 3-17: Entrance-positional distribution of detected ions for TOPAZ. The distribution is shown with respect to the Pro/ENGINEER model of TOPAZ (left) on the vertical plane tangent to the front surface of the instrument. The distribution is enlarged (right), and the origin of the axes is centered on the front-bottom edge of the instrument. The full-area half-maximum contour is highlighted in black.

The above plot indicates the area for which ions of the same azimuthal angle, but varying energies and elevation angles, are detected. Although the collection area occupies a larger azimuthal angle with respect to the instrument's centerline than the azimuthal resolution, the angular accuracy is unharmed since the ions are focused to within the distribution described in Figure 3-16. Based on the full-area half-maximum (FAHM) contour width and height, the effective positional "resolution" in the $x \times y$ directions is approximately 3.0×0.85 cm, respectively. The distribution in Figure 3-13 also displays a doubly-peaked distribution about the centerline of the instrument. This is likely due to the enlarged aperture diameter from the ideal size. Along the centerline of the instrument, ions must be deflected by a larger elevation angle before entering into the channel. On the fringes of the aperture, however, the channel entrance is more horizontal, and the ion trajectory does not have to be "pushed" by the top hat plate into the channel over a large distance. This discrepancy in ion transmission over the aperture affects time-of-flight measurements as well and is discussed in a later chapter. By multiplying the x - and y -resolutions, the total area of the "box of uncertainty" is 255 mm^2 . This is slightly lower than the typical collection area of Faraday probes utilized for far-field ion-current density measurements in Hall thruster plume.⁵⁶ Integration of FAHM contours through a trapezoidal approximation yields a total-effective collection area of 36 mm^2 .

3.5.6 Footprint of Detected Ions

The footprint of detected ions describes the statistics of the landing distribution at the end of the channel. The landing distribution is useful for detector sizing, and directly correlates with the azimuthal landing position discussed previously. Figure 3-18 describes the landing distribution of ions at the exit of TOPAZ.

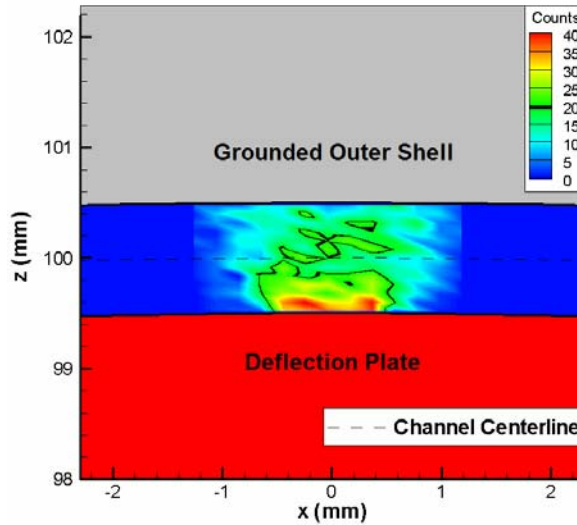


Figure 3-18: Landing distribution of ions at the exit of the channel. The FAHM contour is outlined in black, and the channel centerline is shown as a dashed curve.

Figure 3-18 displays a landing width of approximately 1.3 mm across the 1 mm gap for the ions of 0° azimuthal angle. This small landing size indicates it is likely the detector size which will limit the azimuthal resolution of the instrument, unless the detector is smaller than the ion footprint. It is also evident that ions are most likely to land closer to the deflection plate. This observation agrees with the detection of lower-energy ions then predicted by Equation 3-3. Ions that have less kinetic energy curve more towards the deflection plate while traveling through the channel. The finite width of the gap allows for the lowest-energy ions to first travel from the inside to the outside of the channel (in the z -direction in Figure 3-14), and then curve back towards the deflection plate before reaching the exit of the gap. A distribution plot of the z -landing position versus the ion energy reveals this is the case:

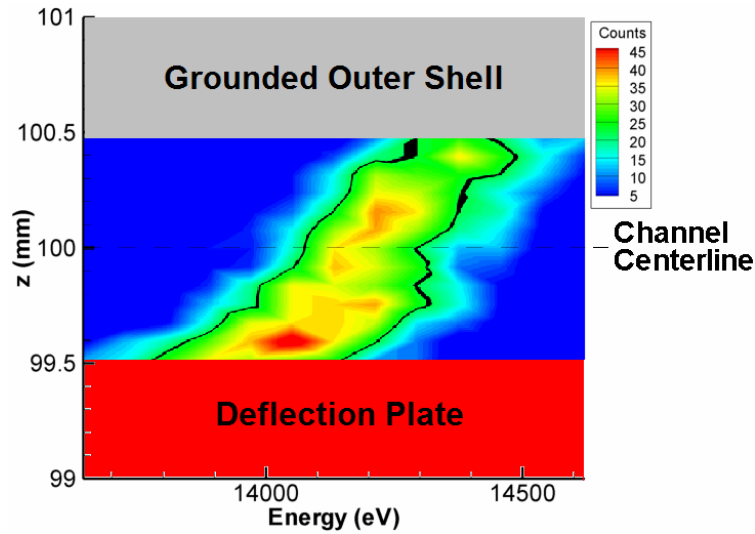


Figure 3-19: Distribution of the z (radial) position as a function of energy for detected ions at the exit of the channel.

Figure 3-19 displays a positive trend between the distance away from the analyzer centerline z and the incident energy of the ion. This trend corroborates the previous assertion that ions of higher-energies are less deflected through the channel. Also, it is interesting to note that a detector smaller than the gap size could significantly increase the overall energy resolution (i.e., decrease $\Delta E/E$), however, the collection area, and therefore the current, would be substantially smaller. This idea is plausible for top hat analyzers of similar size with larger gap sizes.

3.5.7 Top Hat Plate Effects

The top hat plate controls the ions transmission from the elevation-angle selection region to the energy-selection region by “pushing” ions from the horizontal plane into the channel. Since the aperture and top hat diameters were modified from the ideal size, the ion transmission must be compared with the top hat voltage to find the optimum electric field. The top hat plate also functions as a fine-tune control for the elevation angle.

3.5.7.1 Top Hat Plate Correlation with Ion Transmission

The transmission of ions can be defined as the geometric factor, as this value determines the maximum simultaneous “field-of-view” among all parameters. Figure 3-20 displays the correlation between the geometric factor and the top hat voltage normalized by the deflection plate voltage.

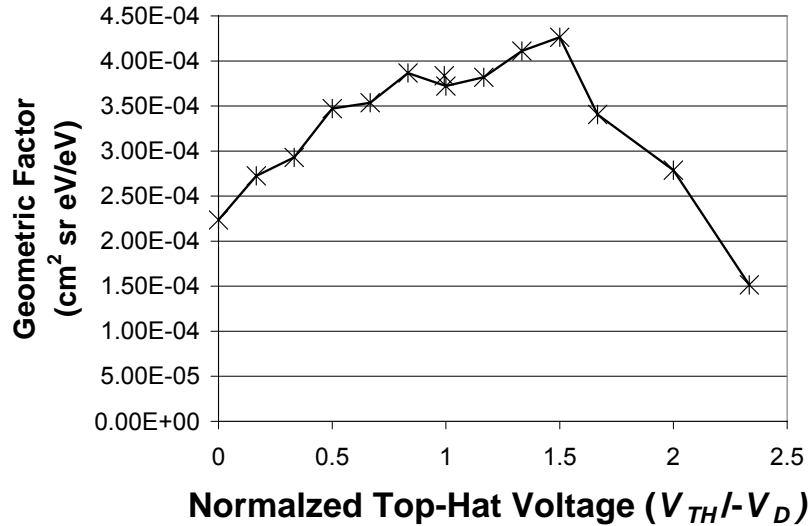


Figure 3-20: Geometric factor variation with the normalized-top hat voltage.

The above plot displays a maximum transmission is possible when the top hat voltage (biased positively) is approximately 1.5 times the deflection plate voltage. This agrees well with the previous prediction that the optimum electric field is created in the aperture for a top hat voltage that is 1.38 times the deflection plate voltage (see section 3.3.3). The geometric factor was independently verified to within 3.6% through a slightly different Monte-Carlo algorithm in SIMION by research scientist Robert Lundgren for the ($V_{TH}/-V_D = 1$) test case.

3.5.7.2 Top Hat Plate Correlation with Elevation Angle

While controlling the transmission of ions, the top hat voltage also changes the average elevation angle of detected ions. This is expected, as it has been shown by Carlson that changing the height (and therefore changing the electric field) shifts the elevation angle distribution. Figure 3-21 describes the elevation angle correlation with the top hat voltage.

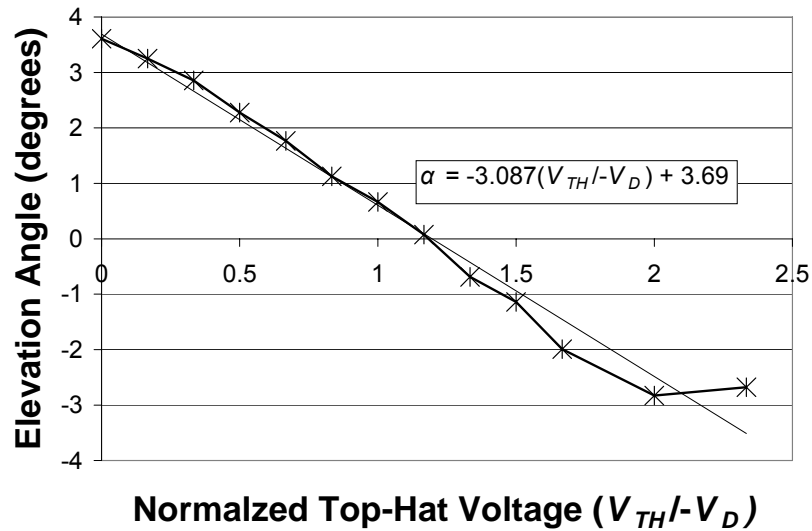


Figure 3-21: The effect of the top hat voltage (normalized) on the average elevation angle with a grounded guiding plate.

The top hat voltage affects the elevation angle less than the guiding plate voltage, and it operates over a smaller range of angles. Although this plate should not be used as a surrogate guiding-plate, the top hat plate can be utilized to “fine-tune” measurements in the vertical direction. This is useful for finding a horizontal beam or maximizing the transmission of ions to the detector. As discussed in a later chapter, this plate is utilized for time-of-flight purposes as an “on-off” switch, since it controls the transmission of ions into the channel.

3.6 Summary of SIMION-Determined Performance Characteristics

Several key relationships as well as interesting effects were derived with SIMION. The resolutions as well as the correlations between plate voltage and ion parameters were determined through the Monte-Carlo simulations.

3.6.1 Theoretical Performance of TOPAZ

Table 4-1 summarizes the major performance parameters determined with SIMION.

Parameter	Design Requirement	SIMION Prediction	Notes
Energy Range	0 – 15 keV	N/A	• Scalability allows for any energy to be measured
Energy Resolution	1.5 %	2.8%	• Machining requirements too high for desired energy resolution
Field-of-View (FOV)	360°×30° (azimuthal×elevation)	120°×27.7° Elevation FOV with fringe effects: 32.4°	• Structural constraints decreased azimuthal FOV • Fringe effects decreased elevation FOV
Angular Resolutions	2°×2° (azimuthal×elevation)	1.3°×2.0°	• Design Requirements Achieved
Effective Collection Area	Not defined	36 mm ²	• Double peaked and symmetric about centerline
Geometric Factor	Not defined	• Grounded V_{TH} : 2.23×10 ⁻⁴ cm ² sr eV/eV • Optimum V_{TH} : 4.26×10 ⁻⁴ cm ² sr eV/eV	• Varies as a function of normalized top-hat voltage

Table 3-4: Summary of SIMION-predicted performance marks as compared with the design requirements for TOPAZ.

Two of the design requirements not met were the energy resolution and field-of-view design requirements. When the design requirements were originally made, the energy-resolution correlation with channel width was unknown. After several simulations with varying analyzer constants, the original design requirement was eased due to manufacturing concerns. Structural constraints prevent the full azimuthal FOV from being achieved; however, since 120° is significantly larger than the FOV required to image any thruster from 1 m downstream, this was deemed acceptable. The geometric factor was decreased at the boundaries of the elevation angle FOV, thereby decreasing the range of elevation angles for which a constant transmission of ions is received. A vertical FOV of 27.7° allows for a 39.3 cm or 52.5 cm object to be viewed by TOPAZ from 75 cm and one meter downstream positions, respectively.

3.6.2 Characterization Curves

The two most important SIMION-derived plate-voltage relationships are the correlation between the deflection plate and measured energy and the correlation between the guiding plate potential and measured elevation angle. Although only singly-charged ions were flown to TOPAZ in SIMION, the deflection plate voltage measures the energy-per-charge, not just the energy. The equations below describe how the plate potentials control the energy (in eV) and elevation angles (in degrees) of detected ions. The top hat plate is assumed to be equivalent (biased positively) to the deflection plate voltage in the below equations; however grounding the top hat plate shifts the curve (by changing the “*b*” in *mx+b* format of the equation) by the amount described in Figure 3-21.

$$\alpha = -5.54 \left(\frac{V_G}{-V_D} \right) - 0.486 \quad \text{Eqn. 3-18}$$

$$\frac{E}{q} = -47.28V_D \quad \text{Eqn. 3-19}$$

The format of the above equations indicates the ion parameters were measured as a function of plate potentials; however these parameters can be solved for, and the required plate potentials can be determined as a function of the desired ion parameters.

3.6.3 Limits of SIMION

The detailed SIMION analysis describes the instrument's response in detail; however, an actual testing of the instrument eliminates any assumptions of the model and takes into consideration such as the 3-D effects of the added structures that break the axisymmetric geometry of the instrument. In the next chapter, the experimental characterization of TOPAZ is presented. The measurements are compared with the SIMION results, and in general, the instrument's response nearly matches predictions of SIMION.

CHAPTER 4:

EXPERIMENTAL CHARACTERIZATION OF TOPAZ

Several of the results obtained in Chapter 3 through SIMION, such as the ion-energy and ion-landing position relationship, would be difficult to determine in a laboratory setting; however, accurate measurements of the energy and angular resolutions, as well as the plate-voltage correlations are crucial for the instrument's operation as a plume diagnostics tool. Although the SIMION simulations of TOPAZ in Chapter 3 describe all the relevant performance characteristics and plate-voltage relationships needed for the instruments operation, measurements with a mono-energetic ion beam account for the instrument's 3-dimensional design, possible effects the insulators (such as plate charging) have on the electrostatics, and deviations from the no space-charge assumption in the ion trajectories.

In this chapter, the hardware and experimental characterization of TOPAZ is presented. The angular resolutions and plate-voltage correlations are determined experimentally. An ion beam facility, which outputs particles of a known energy and angle (since the beam is collimated), along with rotary motion tables are employed to experimentally determine the major relationships derived with SIMION in the previous chapter. These relationships are later utilized to extract data from the unknown far-field plasma of the Busek BHT-600 Hall thruster cluster.

4.1 Construction of TOPAZ

After the 3-D model of TOPAZ was developed through Pro/ENGINEER, the parts were machined on a high tolerance Romi M17 CNC Lathe, which is accurate to within 0.002 in (0.05 mm). Since all of the plates and insulators are mostly cylindrically symmetric, the lathe provided a great resource for the construction of all the parts, while $\frac{1}{4}$ -20 screw holes were tapped with the aid of a drill press (see Figure 4-1).

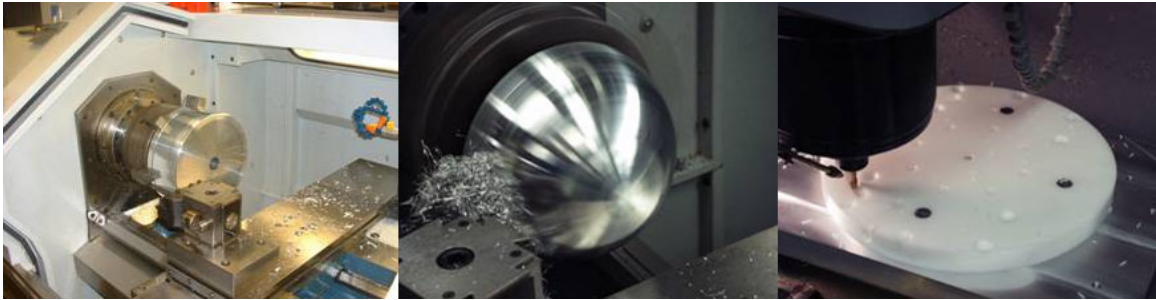


Figure 4-1: Construction of TOPAZ on the Romi M17 CNC Lathe and drill press.

The biased and grounded plates in TOPAZ are made of Aluminum 6061-T6. A Delrin® insulator on top is used to separate the top grounded cover from the guiding plate. Originally, the base plate was constructed out of Delrin®, however, due to the significant thermal-load on the instrument, and relatively low melting point of white Delrin®, the base plate was reconstructed out of machinable glass-mica, a ceramic with low thermal expansion and a high temperature melting point. This plate provides the required separation between the deflection plate and grounded plate to create the channel. Figure 4-2 displays the final construction of TOPAZ.



Figure 4-2: Final Construction of TOPAZ.

4.2 Experimental Apparatus

Two important components, external to TOPAZ, are the ion source and the type of detector utilized for instrument characterization. The ion-beam accelerator system has extensive heritage for the characterization of space-plasma instruments. Channel electron multipliers (CEM) are commonly employed for ion detection, since they significantly amplify the current, and generate small-time-scale pulses suitable for pulse counting and time-of-flight measurements.

4.2.1 Ion-Beam Accelerator System

The ion-beam accelerator system, provided by the Department of Atmospheric, Oceanic, and Space Sciences at the University of Michigan, was employed to calibrate TOPAZ. This facility consists of a homebrewed ion accelerator system attached to a 200,000 cm³ cylindrical chamber and is capable of maintaining an operating pressure of 10⁻⁶ Torr. The ion beam has an energy range from 500 to 30 keV with a current up to 1.5 nA over a 2-cm-diameter beam size (0.477 nA/cm²). Although the current density is

several orders of magnitude lower than a Hall thruster, the facility provides ions with known energies, positions, and trajectories, which is useful for correlation with the response of TOPAZ. The beam facility ionizes air particles as propellant, therefore the beam ions consist of mostly nitrogen, oxygen, and argon. Since topaz discriminates energy-per-charge, the mass of ions is irrelevant to the measurements. Figure 4-3 displays the ion-beam accelerator system.



Figure 4-3: Vacuum chamber (left) with ion-accelerator beam system (right).

4.2.2 Channel Electron Multiplier

A model 30052 Channeltron® by Burle Electro-Optics with an aperture diameter of 0.82 cm was used to detect the ions exiting from TOPAZ through the gap. The CEM operates by allowing ions to strike a ceramic surface with a high secondary emission rate. A voltage of 1800 – 2500 V is placed over the ceramic region to induce secondary electron multiplication within the CEM, and the signal is amplified by $10^6 - 10^7$ depending on the voltage. An Agilent 53131A frequency counter measured the pulse frequency and provided a good estimate of the ion flux out of the exit of the gap.

4.2.3 Power Supplies

The deflection, top hat, and guiding plates are each biased through three Kikusui PMC500-0.1A power supplies. A multimeter accurate to within 0.01 V is utilized to monitor the voltages set on each plate.

4.3 Gap Uniformity

The first test on TOPAZ was to test how well the 1 mm gap is maintained between the deflection plate and the grounded outer shell. The channel must be relatively uniform to ensure the transmission of ions through all azimuthal angles β . TOPAZ was placed on a rotational stage capable for rotating TOPAZ about its centerline to within 0.001° while the CEM remained underneath the instrument at the gap exit. This configuration allowed for beam ions to be measured through different azimuthal angles of the gap. Two test cases are presented and compared: keeping the top hat plate voltage constant (27 V) and optimizing the top hat plate voltage to maximize the counts. In both cases the deflection plate voltage is held constant to an approximate voltage of -21.0 V to measure 1 keV ions. A top hat voltage of 27 V was found to maximize the counts at approximately $\beta = 50^\circ$, and was therefore utilized for the rest of the angles in the constant voltage case. Figure 4-4 displays the counts measured (normalized to the maximum number of counts) as a function of the azimuthal angle.

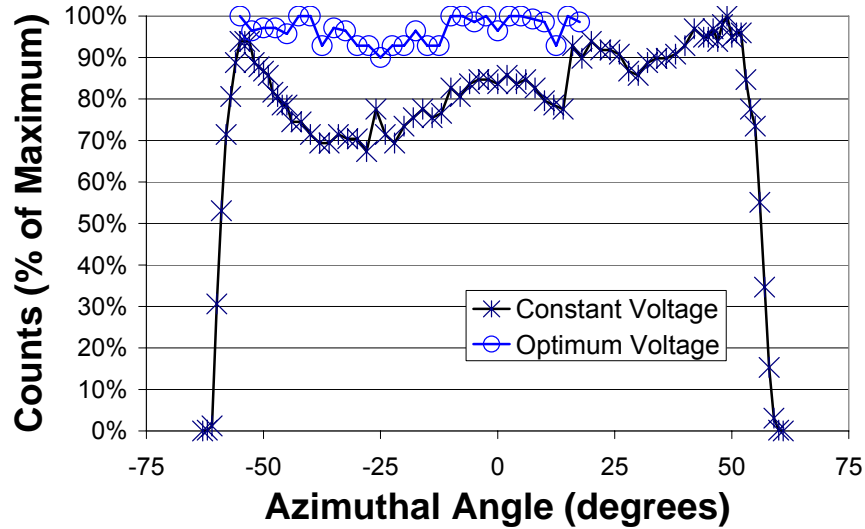


Figure 4-4: Normalized counts versus the azimuthal angle for a 1 keV ion beam.

For a constant top hat voltage, a dip in the counts was seen for lower angles. If the top hat voltage was changed to maximize the number of counts, the transmission of ions was roughly constant from -55° to 57° . The decrease in transmission beyond these angles is due to the Delrin® base plate, which has the 120° slot for the gap. Near the edges, fringe effects decrease the transmission of ions through the channel, decreasing the total range from 120° to yield an azimuthal field-of-view of 112° .

If the top hat plate voltage is varied, and the maximum number of counts is found for each azimuthal angle, the transmission of ions remains relatively constant throughout the azimuthal field-of-view. The likely cause of this is the slight relationship in the top hat voltage and elevation angle measured by TOPAZ. If the instrument is placed on the rotary table at a very small angle off from the axis of rotation, the elevation-angle instantaneous field-of-view (i.e., the elevation angle resolution) will go “in and out” of the ion beam’s constant 90° plane. This causes the dip in transmission; however since the top hat voltage can effectively scan minute elevation angles about the principle angle, the

beam can be “found” again. Although every effort was made to match horizontal plane of TOPAZ with the axis of rotation, this effect illustrates the very high sensitivity of TOPAZ with the elevation angle being measured.

4.4 Plate Voltage Characterization

With SIMION, the average ion properties at the exit of the gap were correlated with the plate potentials. Since information on the ion energy, trajectory, and position is easily obtainable, the plate potentials are matched with the average of each property to develop the correlations. With the ion beam, however, the distribution of the ion properties beyond the resolutions of TOPAZ is difficult to uncover. It is much easier to vary either the plate potentials or beam energy, and determine the settings for which maximum counts is received. Therefore, it is assumed the setting for which the maximum counts is detected is approximately equal to the average of the distribution of counts over which the parameter of interest is varied. For this particular ion-beam facility, this is a good approximation, however since the beam is not perfectly mono-energetic and has slight differences in current as a function of position, the differences in experimental data versus the SIMION simulations could result from the inhomogenities in the beam. Since the current output by the ion beam is a function of the energy, each plot is normalized by the maximum counts measured for the particular beam setting.

4.4.1 Energy and Optimum Transmission Correlations

The ion-accelerator beam provided an easy method for determining the deflection plate and energy-per-charge correlation. The ion energy is varied between 250 eV – 5500 eV, and for each setting, the deflection plate voltage is varied until the maximum number

of counts is reached. The top hat plate is also varied to optimize the transmission for each energy setting. Figure 4-5 displays the relationships derived with the ion beam facility as well as the SIMION-determined correlation for the deflection plate.

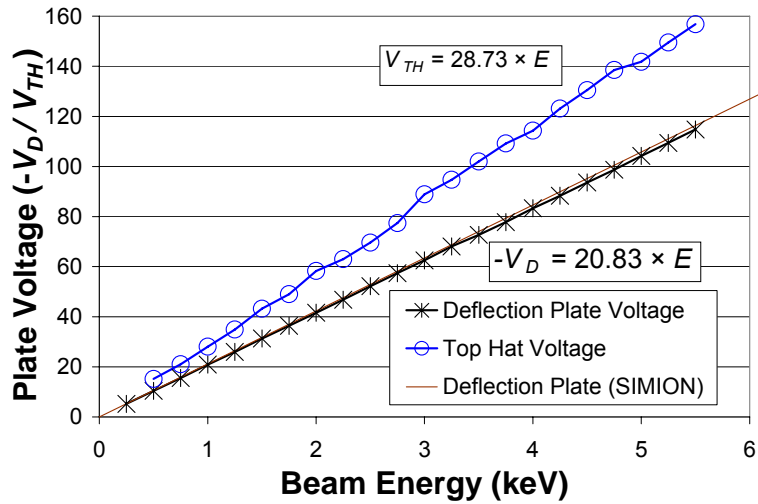


Figure 4-5: Optimum deflection plate and top hat voltages as a function of beam energy for TOPAZ.

4.4.1.1 Deflection Plate Response

For both plates, the optimum voltage is linearly correlated with beam energy. The constant of proportionality for the deflection plate (biased negatively), 20.83, is directly related to the analyzer constant – it is exactly 20 according to theory $((1000 \text{ eV/keV}) / K \times 2)$ and is 21.03 (see section 3.4.2) as determined through SIMION. The coefficient is higher than theory, due to the 3-dimensionality of the instrument, however, fringe effects (and very slight deviances in the channel width of 1 mm) could prevent lower-energy ions from having trajectories which skim over the deflection plate right before being detected (see Figures 3-14, 3-15). This would increase the average energy of detected ions, and yield a slightly higher energy being measured per unit plate voltage.

4.4.1.2 Energy Range

Measurements of the deflection-plate voltage relationship were conducted from 250 eV to 5500 eV. The ion-beam facility allows for a “floating” of the ion-beam power supply up to approximately 30 keV. Measurements on the ion beam with energies of 6-22 keV were conducted with TOPAZ. The power supply limitations for deflection plate voltages restricted measurements above 22 keV, however no arcing between plates was observed for voltages at and below this plate setting. Therefore, the total energy range for TOPAZ was demonstrated between 250 eV – 22 keV.

4.4.1.3 Top Hat Response

For energy settings from 500 eV – 5500 eV, the top hat voltage was adjusted to maximize the transmission of counts to the detector, while the deflection plate voltage was held constant. The top hat voltage functioned as a fine-tuning knob for adjusting the overall transmission for a particular energy. A similarly linear correlation between the optimum top hat voltage and the beam energy was found. By dividing the slopes of each of the correlations in Figure 4-5 the optimum ratio between the top hat and deflection plate voltages is found:

$$\left(\frac{V_{TH}}{-V_D} \right)_{opt} = 1.38 \quad \text{Eqn. 4-1}$$

This compares well with the theoretical value of 1.38 and SIMION-determined value of 1.50 (see sections 3.3.3 and 3.5.7.1, respectively). The transmission properties for the top hat plate are found by profiling the counts for each energy setting. Figure 4-6 displays the profiles for 2 – 5 keV beam-energy settings and compares the profiles with

the SIMION-determined geometric factor correlations in Figure 3-20. The curves are each normalized by the maximum count or geometric factor.

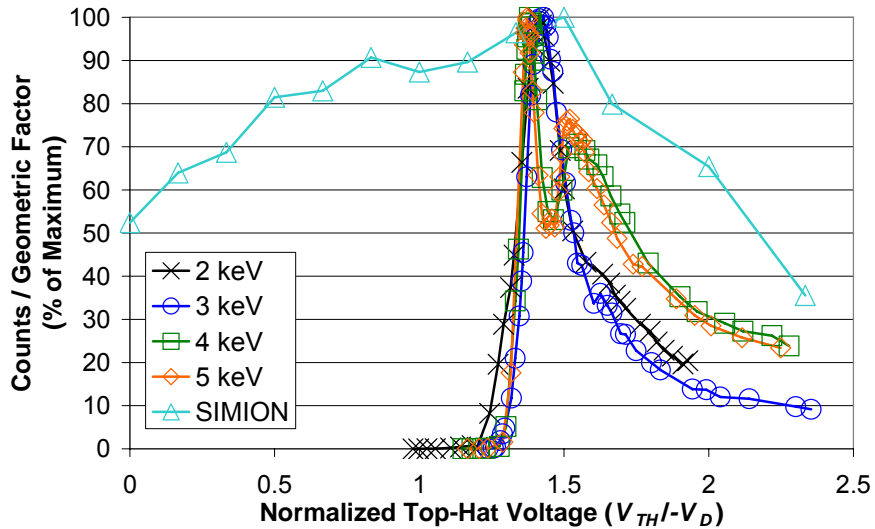


Figure 4-6: Counts measured against the normalized top-hat voltage. The geometric factor plot from Figure 3-20 is normalized here for comparison.

For each of the energy settings, a maximum response was measured for a top hat-deflection plate voltage ratio between 1.35 and 1.45. This is slightly lower than the SIMION-determined peak of 1.5. A sharp decrease in counts was noticed for ratios below 1.3. This is believed to be due to the slight relationship between the top hat voltage and elevation angle as predicted by SIMION (see Figure 3-21). For lower top hat voltages, higher elevation angles are measured, and since the beam has a finite elevation angular-distribution, a decrease in counts was measured when the instantaneous FOV of TOPAZ was outside this range. However, even though counts were not recorded for lower voltages, measurements can be conducted with a grounded top hat according to SIMION. For some of the profiles, a double peak is present. This is likely due to the internal structure of the ion beam, and the sensitivity of TOPAZ with small deviations from a perfectly mono-energetic and constant angularly-distributed ion beam.

4.4.2 Elevation Angle Correlation

To correlate the guiding plate voltages with the measured particle elevation angles, a separate setup from the above tests was used. TOPAZ was mounted sideways on the rotational stage to emulate particles entering into the instrument from different angles. Figure 4-7 displays the setup of TOPAZ for the guiding plate tests.

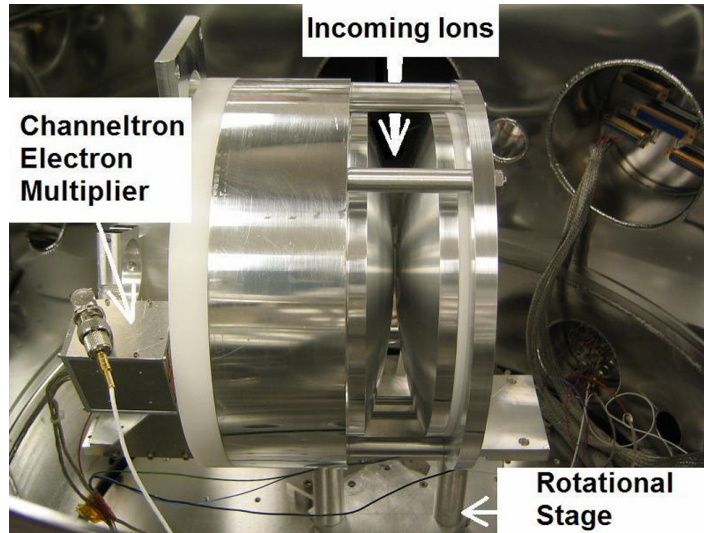


Figure 4-7: Guiding-plate test setup inside the vacuum chamber.

As TOPAZ was rotated about the aperture, ions enter at various elevation angles relative to the instrument. Rotating TOPAZ allowed for characterization of the guiding plates that steer ions in the vertical direction into the aperture. For each guiding plate voltage, the elevation angle with the peak number of counts was found. These data show that a linear correlation between the guiding plate potential and elevation angle exists, a relation that was predicted by SIMION.

Figure 4-8 describes the guiding plate trends with the elevation angle.

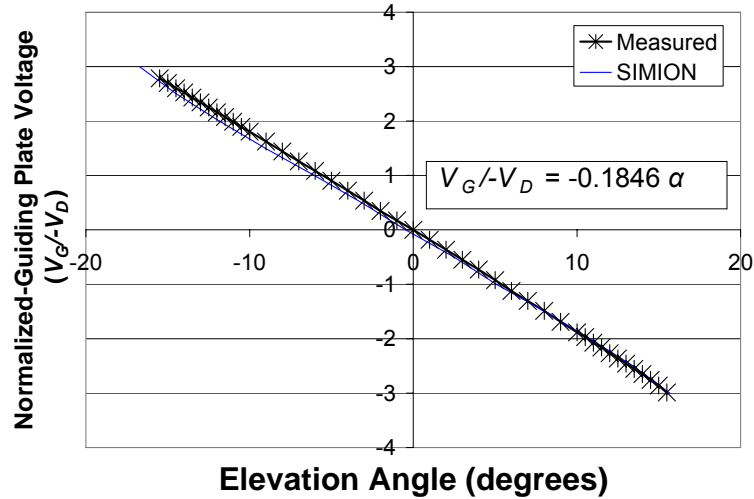


Figure 4-8: Optimum normalized guiding-plate voltage as a function of elevation angle for a 5 keV ion beam.

The measured counts and SIMION results are very similar. A more linear trend was measured with TOPAZ than predicted with SIMION. Since the field generated by the guiding plate was over a larger distance (versus the radius of curvature of the guiding plate), positive and negative voltages up to three times larger than the deflection plate voltage were required to retrieve ions from the full vertical angular field-of-view. The effective elevation angle field-of-view for TOPAZ was measured to be approximately $\pm 13^\circ$ since a sharp decrease in counts was seen beyond these angles; however, ions were detected for angles up to $\pm 15.5^\circ$ from the horizontal plane as well.

Figure 4-8 displays the similar relationship as shown in Figure 3-11 of the previous chapter. The axes are reversed, since for the ion-beam measurements the optimum voltage was determined as a function of elevation angle, while with SIMION the average elevation angle was measured for a given guiding plate voltage. The inverses of the proportionality constants for each of the relations are similar, -5.54 for SIMION

and -5.42 for the experimental data. These two values differ by 2.3% and confirm the accuracy of SIMION's computational results.

4.4.3 Resolution Measurements

Although the correlation between the biased plate voltages and particle angles and energies had been determined, the accuracy (or resolution) of each parameter is also important. The resolutions for the entrance energy and elevation angle were determined by keeping the plate voltages on TOPAZ constant and varying the two parameters. The profiles are compared with SIMION.

4.4.3.1 Energy Resolution

For determination of the energy resolution, the deflection plate potential was held constant, while the energy of the beam ions was varied. A distribution of the detected counts as a function of ion energy was determined. This distribution is compared with the SIMION results (normalized to 3 keV) in Figure 3-10.

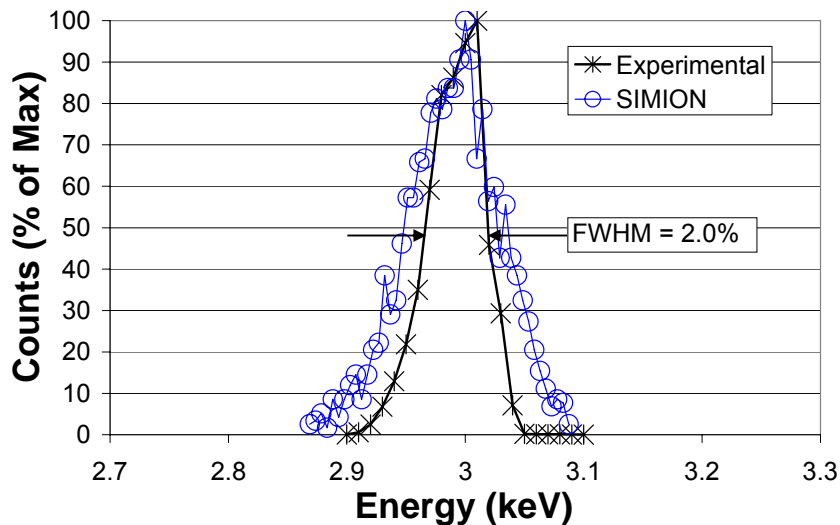


Figure 4-9: Energy distributions for a 3 keV deflection plate setting as compared with SIMION.

The measured and SIMION-deduced energy resolutions based on the full-width half-maximum values were 2.0% and 2.8%, respectively, for the 3 keV beam. The experimental energy resolution is less than the SIMION-deduced value, since any small imperfections in the machining of the deflection plate and grounded outer plates resulting in variances in the channel width decrease the available trajectories through the channel. Since the successful trajectories through the channel are a function of energy, slight deviations from the perfect channel geometry decrease the sensitivity and increase the effective energy resolution. Another possible reason for the smaller energy resolution is the use of ions with a relatively small elevation angle range within the beam. Since there exists a small energy-elevation angle relationship for detected ions, use of a distribution of ions with an elevation angle distribution smaller than the angular resolution will decrease the effective energy range detected as well.

4.4.3.2 Elevation Angle Resolution

For determination of the elevation angle resolution, the plate voltages were held constant while the elevation angle was varied, and the counts were recorded. The same setup as with the guiding plate test was utilized. Figure 4-10 displays the distributions recorded for the 1 keV and 2 keV ion beam settings as well as the SIMION distribution from Figure 3-12.

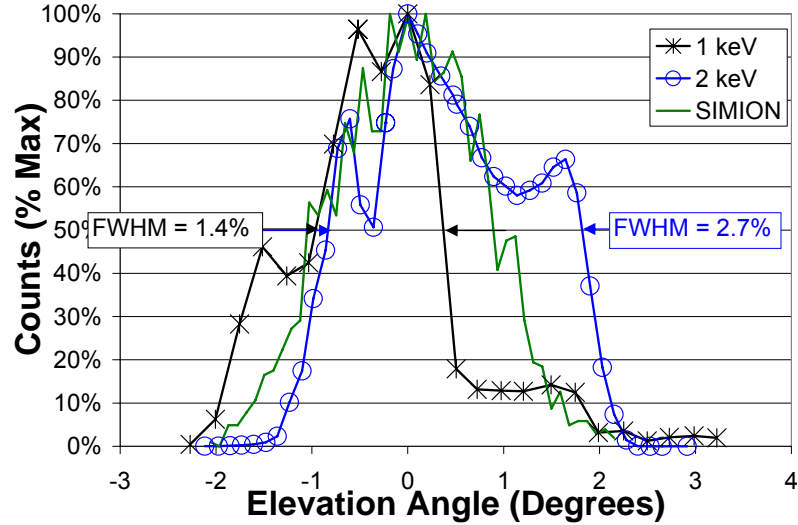


Figure 4-10: Elevation angle distributions for a 1 keV and 2 keV deflection plate setting as compared with SIMION.

The 1 keV and 2 keV distributions yield elevation angle resolutions of 1.4% and 2.7%, respectively. A change in the ion-beam characteristics for the two energies as well as the ion-beam width are likely the causes of the difference between the energy resolutions. The ion beam emanates from a distance of approximately 2 m from TOPAZ. The width of the beam has been measured to be several centimeters. Since a 2° angular width as measured by TOPAZ from 2 m downstream corresponds with a 5.2 cm width, ions arriving from either side of the beam broaden the elevation-angle distribution of ions being detected by TOPAZ. Therefore the assumption of a mono-angular beam is not perfectly valid, and ions will be detected from angles slightly larger and smaller than 0° depending on the beam width. However, the measurements in Figure 4-10 yield an approximate measure of the elevation angle resolution. An average of the experimental values of 2.1% was obtained compared to the SIMION-determined resolution of 2.0%.

4.4.4 Azimuthal Resolution

Since the 0.82 cm diameter of the detector was much greater than the width of the landing footprint at the exit of the gap of 1.7 mm (see Figure 3-18), the detector size limits the azimuthal angle resolution of TOPAZ. However, the previous SIMION simulations had agreed well with the experimental measurements, the SIMION-deduced azimuthal resolution of 1.3° (from Figure 3-16) is assumed accurate but not experimentally verified.

4.5 Summary of Experimental Characterization of TOPAZ

The ion beam facility provided an excellent method of determining the plate-voltage relationships as well as the performance of TOPAZ. This allows the user of the instrument to convert the measurements conducted with TOPAZ through the calibration curves into energy and angular profiles. The resolutions and field-of-views of the instrument describe the capabilities of TOPAZ.

4.5.1 Performance Parameters

Table 4-1 describes the original design requirements as well as the SIMION-determined and experimentally measured performance of TOPAZ.

Parameter	Design Requirement	SIMION	Measurement
Energy Range	0 – 15 keV	0 - ∞ (N/A)	250 eV – 22 keV
Energy Resolution	1.5%	2.8%	2.1%
Elevation FOV	30° ($\pm 15^\circ$)	27.7° (-14.3°-13.4°)	26° ($\pm 13^\circ$)
Azimuthal FOV	360°	120°	112°
Elevation Resolution	2.0°	2.0°	2.1°
Azimuthal Resolution	2.0°	1.3°	Not measured
Geometric Factor	Not Defined	<ul style="list-style-type: none"> • $V_{TH} = 0$: $2.23 \times 10^{-4} \text{ cm}^2 \text{ sr}$ eV/eV • $V_{TH}/V_D = 1.4$: $4.26 \times 10^{-4} \text{ cm}^2 \text{ sr}$ eV/eV 	Not measured
Effective Collection Area	Not Defined	36 mm ²	Not measured

Table 4-1: A comparison of the design requirements and the predicted and measured performance parameters for TOPAZ.

Most of the design requirements were nearly met with the experimental characterization on TOPAZ. The lower-end of the energy range was not confirmed due to limitations of the ion-beam facility. A higher energy resolution than the SIMION-determined value was measured; however, the original design goal of 1.5% was still not achieved. The field-of-view was slightly diminished due to structural constraints at large azimuthal angles and fringe effects at large elevation angles. Nevertheless, the total viewing-angle is large enough for most thrusters in the far-field plume. The azimuthal resolution is approximately the same as that predicted by SIMION.

While the azimuthal resolution, geometric factor, and effective collection area were not directly measured, the SIMION predictions are most likely accurate. The azimuthal resolution will likely be limited by the size of the detector instead of TOPAZ. Knowledge of the geometric factor is useful for comparison with other instruments;

however this trait is not necessary for the operation of TOPAZ. The effective collection area shown in Figure 3-17 is useful for putting collimators in front of the instrument. In general, the collimator should allow for the plasma to reach collection area but nowhere else, so that the thermal load on the instrument is minimized.

4.5.2 Characterization Curves

The two important characterization curves required for the accurate operation of TOPAZ are listed here:

$$-V_D = 20.83 \left(\frac{E}{q} \right) \quad \text{Eqn. 4-2}$$

$$\left(\frac{V_G}{-V_D} \right) = -0.1846(\alpha) \quad \text{Eqn. 4-3}$$

The deflection plate is biased negatively for the detection of positive ions with energy-per-charge given in keV. Theoretically, TOPAZ could be used to diagnose high-energy electrons, as well, through a positive bias of the deflection plate. This is done with the Miniaturized Electrostatic DUal-tophat Spherical Analyzer (MEDUSA) top hat analyzer which utilizes two hemispheres, one for ions and another for electrons, which share the same top hat region.⁹³

The guiding plate is biased positively for the detection of ions from below the horizontal (with negative α) and negatively for ions above the horizontal. Since the above equations are experimentally verified characterization curves, they are used to derive plasma properties through the operation of TOPAZ. The maximum transmission is achieved when the top hat plate is biased $1.38 \times (-V_D)$, however this plate can be

grounded (and not varied) since significant quantities of ions can still be detected with no bias.

With Equations 4-2 and 4-3, TOPAZ can be utilized for Hall thruster plume diagnostics. The extensive SIMION modeling and experimental characterization of the instrument allows for accurate diagnosis of the plume. The next chapter reviews measurements on the BHT-600 Hall thruster cluster with TOPAZ. Besides the plate voltages that can be varied with TOPAZ, the instrument can be placed at different thruster angles and positions in the plume. Single versus multiple thruster operation is possible as well, and the operating voltage of the engines can be varied. Although the focus of this dissertation is TOPAZ, and not the measurements conducted by the instrument, measurements on the plume yield novel, interesting results. The instrument's value as a plume diagnostics tool is proven with the energy-angle measurements conducted on the BHT-600 W Hall thruster cluster.

CHAPTER 5: MEASUREMENTS ON THE P5 HALL THRUSTER AND BHT-600 CLUSTER

In Chapter 2, the top hat analyzer was presented as an instrument with capabilities other diagnostics instruments lack. Chapters 3 and 4 described the design, modeling, and experimental characterization of TOPAZ through SIMION and an ion-accelerator beam facility. In this chapter, TOPAZ is tested on the BHT-600 Hall thruster cluster, a group of 4 mid-sized 600 Watt Hall thrusters. However, before extensive measurements were made on these thrusters, some changes to the instrument were done to adapt the instrument to a high-density plasma environment. As a preliminary test, TOPAZ was utilized to take measurements on the AFRL/UM P5 Hall thruster. Since the thruster has been heavily characterized, measurements could be compared with existing data to determine the veracity of the measurements through TOPAZ.

5.1 Measurements on the P5 Hall Thruster

After the successful characterization of TOPAZ, measurements on the P5 Hall thruster were conducted to verify the instruments operation in a relevant plasma environment. A description of the experimental setup and measurements with TOPAZ follows.

5.1.1 Experimental Setup

TOPAZ was placed 1 m downstream the centerline of the AFRL/UM P5 Hall thruster. All measurements were conducted in the University of Michigan's 6 m diameter by 9 m long Large Vacuum Test Facility (LVTF) at the Plasmadynamics and Electric Propulsion Laboratory (PEPL). The thruster was mounted on thruster station 1, while TOPAZ was mounted on thruster station 2. Figure 5-1 displays a schematic of the LVTF.

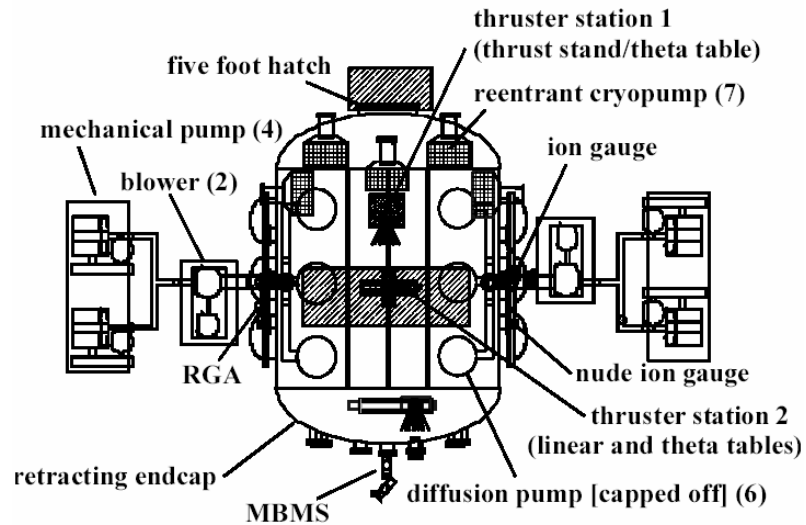


Figure 5-1: Schematic of the Large Vacuum Test Facility (LVTF).

The LVTF is equipped with seven CVI TM-1200 re-entrant cryopumps, which are each surrounded by an LN₂ baffle, to provide a total pumping speed of 500,000 l/s on air, and 240,000 l/s on xenon. Varion model 571 and UHV-24 ionization gages monitor the chamber pressure (shown in Figure 5-1). Only two cryopumps were used to purposely create an elevated ultimate base pressure of 2.5×10^{-5} Torr. The pressures presented during the operation of TOPAZ in the LVTF are corrected for xenon particles through the following equation:⁹⁴

$$P_c = \frac{P_i - P_b}{2.87} + P_b \quad \text{Eqn. 5-1}$$

Although the operating pressure of the chamber was above Randolph's criterion of 1.0×10^{-5} Torr for negligible facility effects on plume measurements,⁹⁵ a high-density plasma environment yielded the largest amount of Debye shielding which would be test the instrument's operation in an extreme setting. Measurements by Walker of the plume properties of a Hall thruster at various pressures have yielded facility effects below 1.0×10^{-5} Torr, as well.⁹⁶

A thermocouple was placed on the top cover of TOPAZ in the position shown in Figure 5-2.

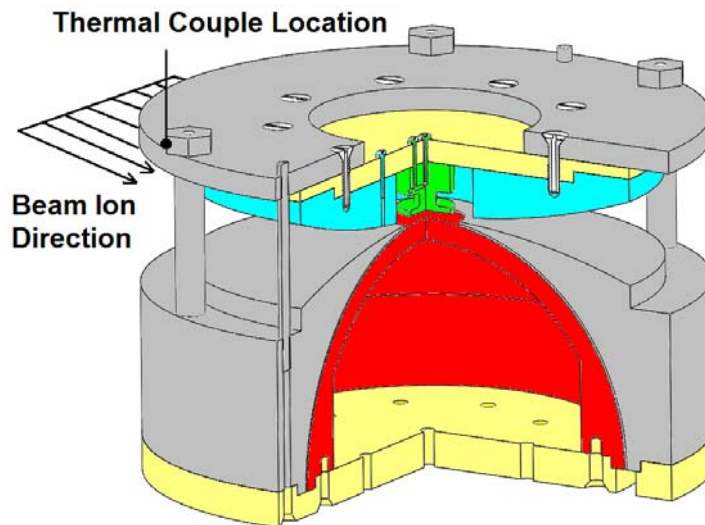


Figure 5-2: Location of thermocouple for the monitoring of temperature of TOPAZ.

For the tests on the P5 Hall thruster, an electro-mechanical graphite gate was placed in front of the entrance to TOPAZ. The gate could be controlled outside of the chamber, and was opened for measurements and closed for protection from the high-energy beam ions emanating from the thruster.

5.1.2 Ion Detection and External Hardware

Although an array of detectors could be placed at the exit of the gap for simultaneous azimuthal measurements, a single K&M Electronics model 7550m channel electron multiplier (CEM) was employed for the detection of ions at a single azimuthal angle. It is important to note, the CEM does not discriminate between charge-states of the ions and sends approximately equivalent current-pulses for every particle detected (see Section 4.2.2 for CEM operation theory).

The entire instrument was rotated about the azimuthal axis. As the instrument is azimuthally axisymmetric, this allowed for a virtually 360° viewing-angle in the azimuthal direction and eliminated the structural limitations on the field-of-view. A Daedal 20600RT rotary table with a resolution of 0.001° was operated through LabVIEW 6 software to rotate the instrument and CEM. The CEM was enclosed in a grounded cylindrical shield with a slit entrance, which limited the entrance of ions across 3.5 mm. The ion focusing of TOPAZ was within 1.3°, therefore, the size of the CEM limited the azimuthal resolution of TOPAZ to approximately 2.0°

Since the amount of ions detected at the exit of the channel was expected to be much higher than with the ion beam, a Keithly Picoammeter was employed to measure the current generated by the CEM outside of the LVTF. Plate potentials were controlled by a Keithley 2410 Sourcemeater and Kikusui power supplies.

5.1.3 AFRL/UM P5 Hall Thruster

The P5 Hall thruster was operated at an anode voltage of 300 V and a current of 5 A. The thruster has a mean channel diameter of 148 mm with a channel width of 25 mm. A Moscow Aviation Institute (MAI) acts as the electron source and neutralizer and is

located in the 12 o'clock position of the thruster. The anode and cathode flow rates were 54.3 and 9.4 mg/s on xenon, respectively. Haas describes this thruster and its performance in detail.⁹⁷

5.1.4 Measurements

An energy-per-charge profile along the thruster centerline was conducted with TOPAZ. The measurements of deflection plate voltages are converted into energy-to-charge through Equation 4-2. Figure 5-3 displays the measurement:

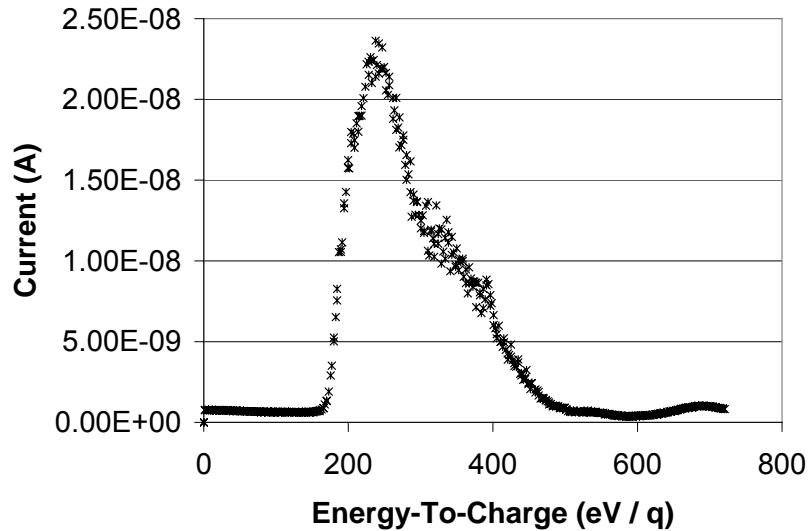


Figure 5-3: Energy-to-charge profile measured by TOPAZ for the P5 Hall thruster operating at 300 V and 5 A.

The error in the energy-per-charge is assumed to be equivalent to the resolution of TOPAZ – 2.0%. A peak at approximately 250 eV is measured for the thruster. This is similar to the peak of approximately 260 eV seen by Gulczinski on this thruster through measurements with the Molecular Beam Mass Spectrometer (MBMS).⁸⁰ This preliminary measurement confirmed the successful operation of TOPAZ. However, after approximately 45 minutes of immersion in the plasma, the peak current was measured at

successively higher energies. Eventually the current-peak drifted to voltages well beyond the operating voltage of 300 V. The measurements were not repeatable. A look at the temperature profile of TOPAZ as a function of time helped explain why this was happening.

5.1.5 Thermal Load on TOPAZ

Figure 5-4 displays a graph of the temperature measured with TOPAZ as a function of time.

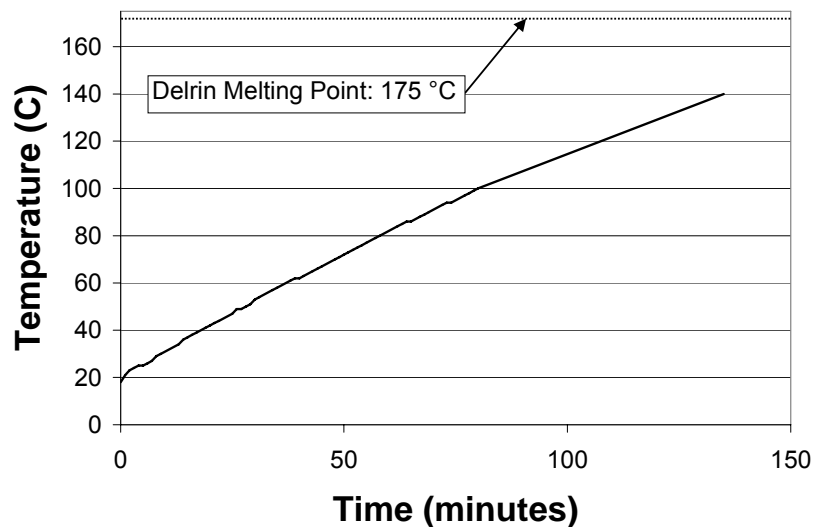


Figure 5-4: Temperature of TOPAZ one meter downstream the P5 Hall thruster as a function of time.

The above plot displays a significant thermal load on TOPAZ increased the temperature of the instrument dramatically. For approximately the first hour, the temperature increased at an approximate rate of 1 °C per minute. The melting point of the Delrin® plastic was approached in approximately three hours of continued immersion in the plasma! This posed a cap to the length in time for useful data taking. However, these measurements helped to explain the drift in the peak energy of successive energy-to-

charge profile measurements on the P5 Hall thruster. Since the coefficient of linear thermal expansion of Delrin® is 1.22×10^{-4} mm/(mm-K), a different in temperature of 20 K (or °C) across the channel diameter of 20 cm could yield an expansion of the Delrin® base plate by up to 0.49 mm. This is a significant fraction of the 1mm channel width. It is likely that thermal shifting in this plate changed the electric field between the inner deflection plate and outer grounded shell, thereby decreasing the effective analyzer constant. A shift in the inner plate towards the front of the instrument would increase the required voltage to detect beam ions, and artificially stretch the profile in Figure 5-3 towards higher energies.

5.1.6 Remachining of the Base Plate

Upon examination of the Delrin® base plate, significant melting of the material was present near the steel members which held the instrument in place inside the chamber. The structure likely heated up from the impact of beam ions and conducted heat-energy into the base plate of TOPAZ through its supports. The temperature at this site was not measured, and could have been higher than the measurements in Figure 5-4. Delrin® is an excellent choice for diagnostics instruments with low thermal loads due to its low water absorption, easy machinability, and good strength and insulative properties. However, due to the high thermal load of beam ions in the Hall thruster plume, a new material had to be utilized.

The base plate was remanufactured with High Temperature Machinable Glass-Mica. This ceramic has a coefficient of linear thermal expansion of 1.05×10^{-7} mm/(mm-K) with a thermal range up to 400 °C. The decreased thermal expansion (by 3 orders of magnitude) and much higher temperature range would allow TOPAZ to survive the high-

temperature environment in the Hall thruster plume. The coefficient of linear thermal expansion for the ceramic is also much less than Aluminum (2.3×10^{-5} mm/(mm-K)).

5.1.7 Conclusions on the Preliminary P5 Hall Thruster Measurement

TOPAZ survived the high-density environment of the Hall thruster plume; however, the thermal load on the instrument melted the base plate and required remanufacturing. The energy profile measured for the P5 Hall thruster confirmed the successful operation of TOPAZ as an energy analysis tool for Hall thruster plume diagnostics in a relatively high particle-density environment where facility effects can interfere with energy profile measurements. With the instrument's successful preliminary "test" measurement on the P5 Hall thruster, the instrument was ready for use with the BHT-600 Hall thruster cluster.

5.2 Measurements on the BHT-600 Hall Thruster Cluster

To further confirm the operation of TOPAZ within a Hall thruster plume, as well as characterize the plume of a cluster Hall thrusters, TOPAZ was placed one meter downstream of a cluster of four 600 W BHT-600 Hall thrusters. Four of the seven re-entrant cryopumps were operated to minimize facility effects and obtain accurate measurements of the cluster in an environment similar to low-earth orbit (LEO). The operating pressure for the cluster configuration was 4.1×10^{-6} Torr, while for single thruster operation the pressure was 1.97×10^{-6} Torr. Figure 5-5 displays the cluster.

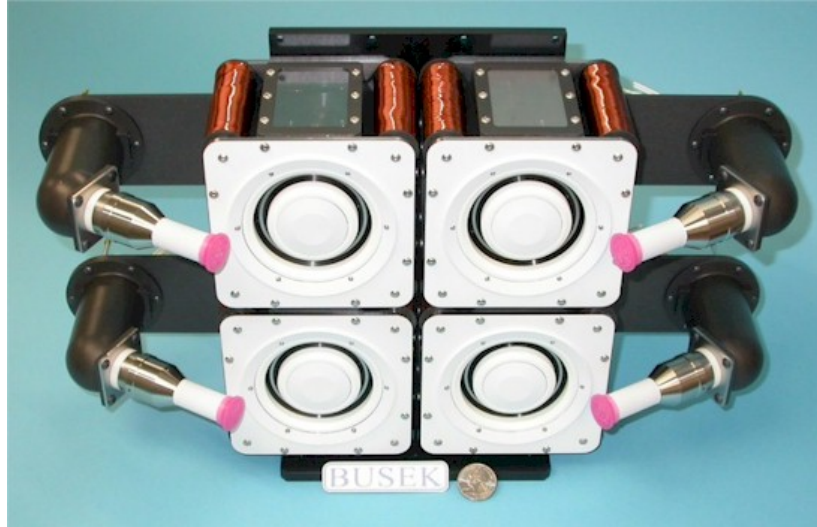


Figure 5-5: The 4×600 W BHT-600 Hall thruster cluster.

5.2.1 BHT-600 Cluster

The BHT-600 cluster was acquired for basic research on cluster characterization, facility effects, and plume characterization. Each thruster operates on xenon propellant at 300 V and 2 A. The cathode and anode flow rates for each thruster are 2.5 and 0.5 mg/s on xenon, respectively. The cathodes are mounted at the 9 o'clock and 3 o'clock positions on each thruster for the left and right sides of the cluster, respectively. Measurements were conducted at thruster plume angles of 0° and 60° to the left of the thruster from the vantage point of being downstream and looking upstream towards the cluster. Each thruster has mean channel diameter of 5.6 cm and is placed in a 4-square configuration such that the centerline-to-centerline distance is 11 cm. Single thruster measurements were performed on the bottom-left thruster.

5.2.2 Experimental Setup

Similar to the setup discussed in Section 5.1.1 above, the cluster was run from either thruster station 1 with TOPAZ placed on thruster station 2, or with the cluster on

thruster station 2, and TOPAZ mounted a meter downstream with unistrut stands. Either setup allowed for interrogation of the plume from 1 meter downstream at multiple plume angles. Thruster station 2 is mounted on two linear tables, each positioned perpendicularly to each other. This configuration allowed for measurements by TOPAZ to be taken from different angles on the cluster centerline by either moving the cluster with respect to TOPAZ or vice versa. It is assumed that both configurations yielded equivalent measurements of plume properties for various angles. All angles present are defined with respect to the cluster centerline, even for single thruster measurements.

Figure 5-6 displays the setup inside the chamber.

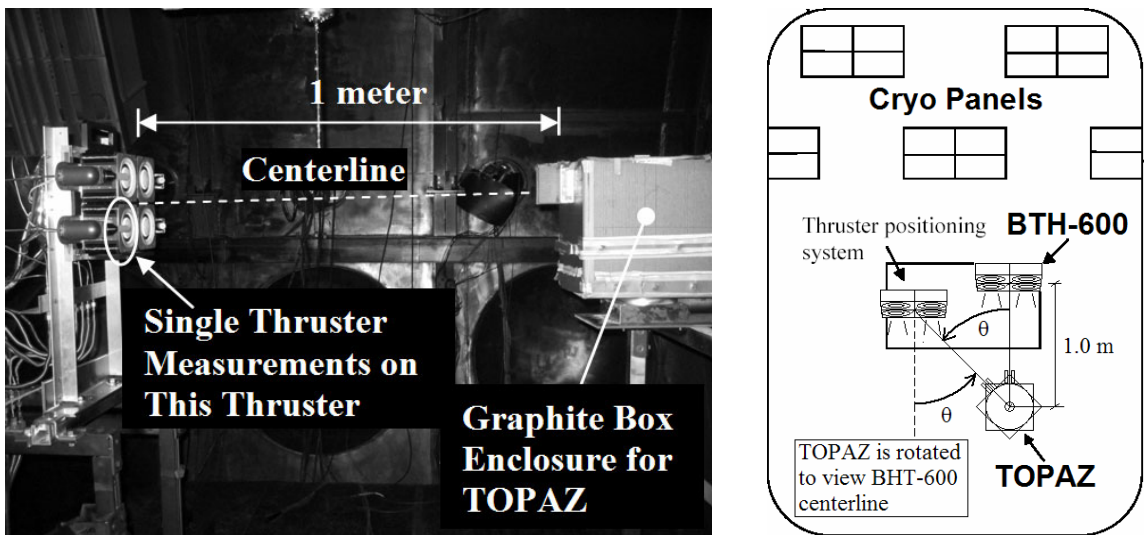


Figure 5-6: Setup of TOPAZ for measurements on the BHT-600 Cluster inside the LVTF. On the left, TOPAZ is moved to multiple angles with respect to the cluster, while the setup on the right, the cluster is moved with respect to the stationary TOPAZ.

Due to the high thermal load experienced with measurements on the P5 Hall thruster, a graphite box enclosure was used to protect TOPAZ from the beam ions. A thermocouple was mounted in the same position as shown in Figure 5-2. As with the previous P5 measurements, a K&M Electronics model 7550m channel electron multiplier

was employed to detect ions after they passed through TOPAZ, and a Keithley Picoammeter monitored the current generated by the CEM outside of the chamber.

5.2.3 Experimental Results and Discussion

A more extensive set of measurements were conducted on the BHT-600 cluster than the P5 Hall thruster. During all tests, the temperature remained between 20 – 67 °C. The temperature reached equilibrium with use of the graphite enclosure, unlike the tests on the P5 Hall thruster. Data sweeps were taken by either varying the deflection plate voltage to generate energy profiles or by sweeping through elevation and azimuthal angles at constant plate voltages to piece together “images” of the thruster(s) at a particular energy.

5.2.3.1 Energy Profile of Cluster

A similar energy-to-charge ratio profile of the cluster down the thruster centerline (thruster angle of 0°) was measured with TOPAZ with a grounded guiding plate setting. Figure 5-7 displays the plot.

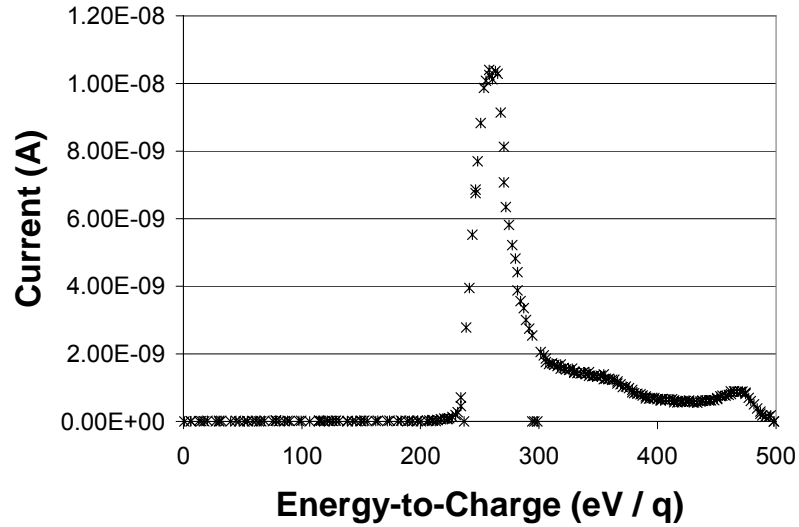


Figure 5-7: Energy-to-charge profile for the BHT-600 cluster along the centerline from 1 m downstream.

Similar to the P5 energy-to-charge measurement, a peak is seen at approximately 270 eV which is near the operating voltage of 300 V for the thruster. Ions with energies near 230 eV/q and up to 500 eV/q were measured as well. The peak ion voltage exists slightly below the discharge voltage due to the decrease in plasma potential near the anode. Ions accelerated in this region do not realize the full potential drop from the anode voltage to ground, because there is a voltage spread near the discharge channel.³⁸ Ions above and below this peak are measured due to charge-exchange (CEX) and momentum-exchange collisions with low-energy particles. CEX can decrease the charge-state of an ion while maintaining its energy, thereby creating ions with energy-to-charge ratios that are significantly higher than the thruster discharge-voltage in the plume.⁹⁸

5.2.3.2 Azimuthal Beam-Ion Distribution for Cluster Operation

By keeping the deflection plate and guiding plate voltage constant, the azimuthal position of the detector was varied to measure horizontal distribution of beam ions. The

guiding plate voltage was set to a voltage of -9 V. This corresponds to a vertical angle of approximately 8.5° and matched the top two thrusters. The azimuthal resolution is assumed to be equivalent to the SIMION-determined value of 1.3° . Figure 5-8 presents the azimuthal distribution of 275 eV/q beam ions that were detected from the horizontal centerline of the top two thrusters.

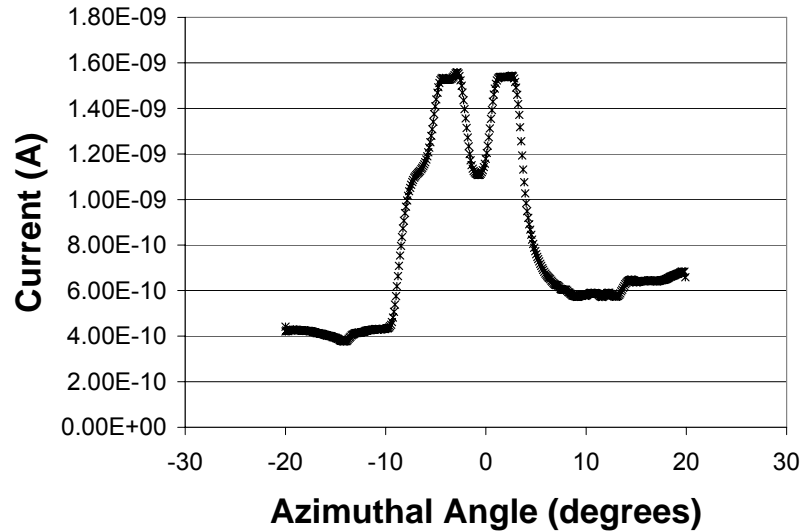


Figure 5-8: Azimuthal profile of 275 eV ions for the top two thrusters in the BHT-600 cluster.

The two peaks in the profile of Figure 5-8 are spaced 5.54° apart. With knowledge of the thruster centerline-to-centerline distance of 11 cm, a calculation of the effective profiling distance could be made, based on the apparent angle of 5.54° measured with TOPAZ. This yields a measurement distance of 113 cm. Since the distance of the front end of TOPAZ was 1 meter from the thruster face, and the radius of TOPAZ is 12.6 cm, the “imaging plane” is *not* the front tip of TOPAZ but rather the axis of symmetry of TOPAZ. The reason for this effect lies in the trajectory of detected ions. The azimuthal angle remains largely unchanged until the ion reaches the aperture. Over the aperture the ions are focused (see “top view” of Figure 3-3), and the azimuthal angle

is effectively “selected.” Therefore, azimuthal angular-selection on the ion trajectories occurs over the axis of symmetry of TOPAZ.

The image of 275 eV/q ions from the cluster indicates the beam ions from each thruster are not blurred together. Their trajectory is maintained into the far-field plume and beam ions from each thruster are easily discerned. A slight dip is also noticed at each peak, which is indicative of the annular geometry of the Hall thruster. The size of the dip is approximately 1.46° . Although this is beyond the azimuthal resolution, this is smaller than the expected dip size of 2.84° , and could be indicative of slight ion focusing from the discharge channel towards the centerline of each thruster.

5.2.3.3 Energy-To-Charge and Azimuthal Angle Relation for Cluster Operation

By profiling energy profiles for separate azimuthal angles, and “image” of the energy-azimuthal angle relation is formed. For this measurement the guiding plate was grounded for an approximate measurement along the centerline of the thruster. Figure 5-9 displays the contour plot of this relationship.

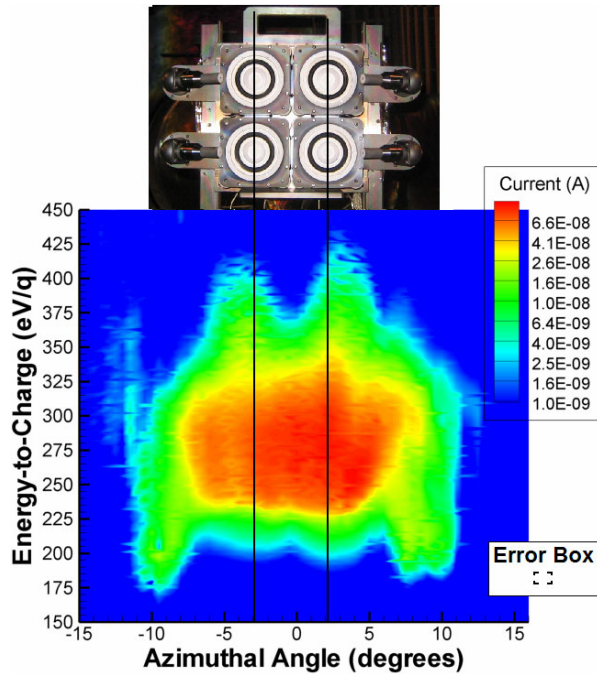


Figure 5-9: Current as a function of azimuthal angle and energy-to-charge for the BHT-600 cluster. The color coding is exponential to enhance low current features.

Since some important features of the above plot occur with low currents, an exponential color coding is utilized to enhance these features. The cluster setup from the vintage point of TOPAZ is placed above the graph to azimuthally correlate measurements on the thruster with the plot. Since the density of data points is beyond the energy and azimuthal resolutions, the error “box” is assumed to have dimensions of these resolutions.

It is interesting to note that each energy profile (a vertical slice) is highly dependant on the azimuthal angle being measured. The bulk of the current was measured at energies between 240 – 325 eV at positions directly in front the cluster. However, directly along the thruster centerlines, a wide energy-spread was measured between 200 eV – 420 eV. Since the cathode plume directly outputs electrons and neutral particles in front of the thruster, it is possible that cathode-plume interaction with the ions emitted from the discharge channel created multiply-charged ions which underwent charge-

exchange (CEX) collisions. A conversion of a doubly-charged to a singly-charged ion will be detected with an energy-to-charge ratio which is twice the ion's original acceleration potential before the CEX collision.

Measurements to the outside regions of the cathode indicate significant populations of ions from 175 – 325 eV. These low energy-to-charge ions are either products of CEX collisions where the ionic state increased or momentum-exchange (MEX) collisions resulting in lower energies for the ions. If the ionic state increases or the energy decreases, the overall ratio decreases. Ions also born at potentials outside the discharge channel will have lower energies in general; therefore the energy-to-charge ratio will be lower if the ionic state of the ion does not change.

5.2.3.4 Elevation Angle and Energy-To-Charge Correlation for Single Thruster Operation

Measurements on single bottom-left thruster were conducted to illustrate differences (if any) between the plume properties of single-thruster versus cluster operation. The thruster is located at apparent angles of -3° in both the elevation and azimuthal angles. For the first measurement, the guiding plate potential was varied as a function of each energy-to-charge profile. The azimuthal angle was held constant along this thruster's centerline ($\beta = -3.0^\circ$). This allowed for a correlation between the measured elevation angle and energy-to-charge to be determined. Figure 5-10 displays a plot of the relationship measured for the single-thruster operation. Since the current is displayed on a linear scale on this plot and the following plots, the units of current are discarded. A maximum current of 1×10^{-7} A was measured.

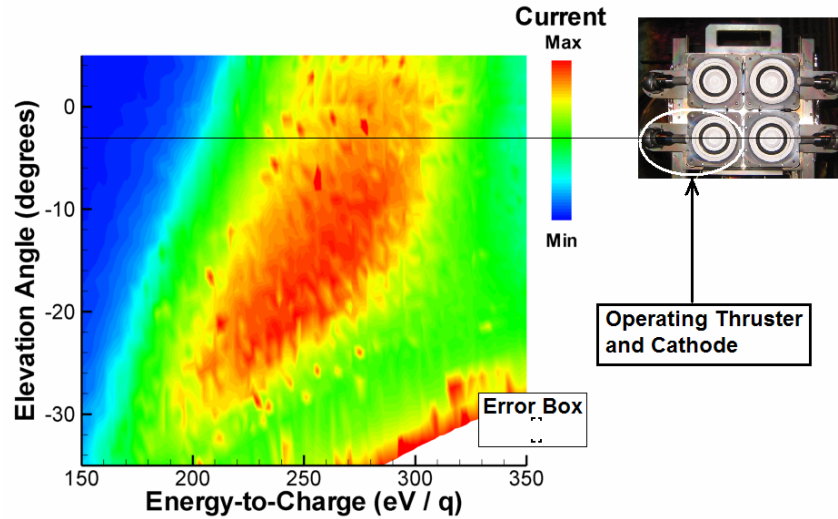


Figure 5-10: Elevation angle and energy-to-charge relationship for the bottom-left BHT-600 thruster at a 0° cluster plume angle.

For Figure 5-10, horizontal slices represent energy-to-charge profiles taken at different elevation angles. The above plot indicates ions with lower energies are generally measured at lower elevations. There is a positive correlation between the elevation angle and energy-to-charge ratio. Since the thruster is slightly below the horizontal plane of TOPAZ, measurements at lower elevation angles also correlate with measurements further away from the thruster face and within the plume. Ions that are born outside the channel and directly in front of the thruster must have positive elevation angles to reach TOPAZ from below the horizontal plane. Since the plasma potential decreases as a function of distance away from the discharge channel, the correlation could be the result of ions being accelerated by lower potential drops in front of the thruster. The plot indicates that ions with larger deflection from the horizontal plane that emanate away from the thruster tend to have lower energies. This idea is corroborated with a plot of the energy-to-charge correlation with azimuthal angle for the single thruster.

5.2.3.5 Energy-To-Charge and Azimuthal Angle Relation for Single Thruster Operation

As with the cluster operation, a plot of the energy-to-charge ratio as a function of azimuthal angle was done for the single-thruster operating condition as well. Figure 5-11 displays a plot of the energy-to-charge relationship with the azimuthal angle for the bottom-left thruster.

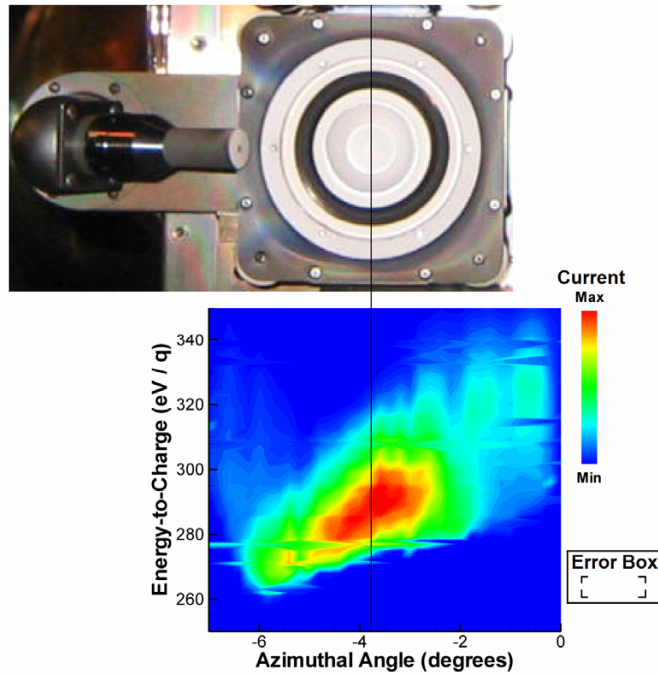


Figure 5-11: Current as a function of azimuthal angle and energy-to-charge ratio for single BHT-600 thruster operation along the cluster centerline.

As with the cluster measurement of energy-to-charge ratio as a function of azimuthal angle, a similar trend of ions with lower energies emanating from the near the cathode is noticed. In comparison with Figure 5-9, the emanation area is much smaller, not just overall, but per thruster. The effective width of the detection of ions is over approximately 6° which correlates to 11.8 cm from 112.3 cm downstream of the thruster (i.e., the effective plume interrogation point). This is approximately twice the discharge channel diameter. For the cluster operation, the area was over approximately 20° . A

significant number of ions were detected from behind the cathodes, whereas for the single thruster operation these ions are absent.

A possible scenario for this is the ionization of propellant particles due to interaction with the opposite-cathode plume. Since the cathode plume likely extends across the entire cluster and over the oppositely-placed cathodes, electrons which “overshot” the discharge channels could provide an ionization source behind the oppositely placed cathodes. The cross-pollination of electrons would effectively increase the total number of ions produced per cathode. Since the overall ionization region is increased, a slight increase in thrust is predicted for the cluster configuration versus the sum of four single-thruster measurements of thrust. This scenario assumes the ions generated behind the cathodes were not “displaced” ions that would have been accelerated in front of the discharge channel.

Measurements and simulations by Beal on the BHT-200-X3 cluster, showed that the cluster configuration yields an ion-focusing effect on CEX ions while the beam ions are largely unaffected by weak fields generated with the concurrent operation of the thrusters.⁹⁹ Walker measured thrust for single thruster and a two-thruster cluster configuration of the P5 Hall thruster “twins.” He found no change in the overall thrust of cluster configuration for the 5 A setting and a slight increase in the 10 A operation which he attributes to the increased ingestion of background particles due to facility effects.¹⁰⁰ It is important to note that for the operation of the P5 cluster, the cathodes were not facing the discharge channels of the opposite thruster. However, for the BHT-600 cluster, this is the case, and measurements by TOPAZ support the theory that the cross-pollination of

electrons emitted by the cathodes could increase the overall ionization of beam ions, and therefore increase the overall thrust and thruster efficiency for the cluster configuration.

The asymmetry measured in Figure 5-11 also indicates the thruster generates slight yawing-torque towards the cathode since ions are accelerated to higher energies away from the cathode versus near the cathode. Recent experiments conducted by Hofer suggest that a centrally placed cathode decreases plume divergence and results in an asymmetric plume about the thruster axis.¹⁰¹ Since a centrally-placed cathode would eliminate thruster output-power into the yawing-torque as predicted by TOPAZ, it is possible a slight increase in thrust force, and hence anode efficiency, would be measured with this configuration if the input power was held constant.

A final measurement of a beam-ion “image” for the single thruster configuration was conducted at a cluster angle of 60°.

5.2.3.6 Beam-Ion Image of Single Thruster Operation at 60°

By keeping the deflection plate voltage constant for a detection setting of 275 eV/q ions, and sweeping the azimuthal position and guiding plate potential, an “image” of the beam-ions emanating from the lower-left thruster was created at a 60° cluster angle. Figure 5-12 displays a plot of the data.

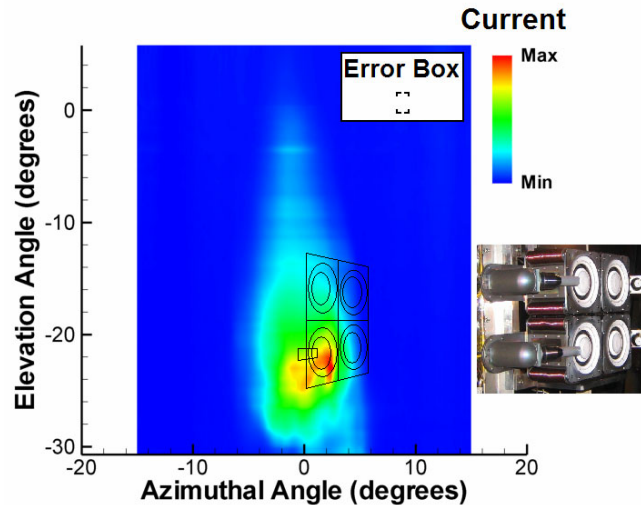


Figure 5-12: An image of 275 eV/q ions emanating from the bottom-left BHT-600 thruster. An approximate projection of the thruster dimensions (with the operating-thruster cathode) over the angles is drawn.

An immediate effect believed to be due to Debye shielding is apparent in the above plot. The beam ions are detected from well below the horizontal plane of 0° with a maximum of approximately -22° . Since the thruster's apparent elevation angle is -3° from the vantage point of TOPAZ, the image seems to be shifted by -19° . A possible reason for this is the exposure of the guiding plate to high-density plasma. The guiding plate region has a maximum plate separation of 37 mm. Assuming an approximate plasma density of $10^{14} - 10^{15} \text{ m}^{-3}$ yields Debye lengths of 0.3 - 1 mm. This corresponds to effective shielding distances of 3 - 10 mm. Since the guiding plate separation varies from 37 mm to approximately 3 mm near the aperture, it is likely that portion near the aperture was functioning properly (i.e., creating the expected electric field), while near the leading edge, the plate was being insulated by the plasma. Larger voltages were therefore required to turn ions from the desired elevation angle to the horizontal plane over the aperture. Since the oval shape is approximately indicative of a circle which is projected

from a 60° onto the thruster, it is *assumed* that the coefficient of correlation between the elevation angle and guiding plate voltage is approximately the same as measured with the ion beam facility. The shifting effect likely existed for elevation angle and energy relationship measured in Figure 5-10, however, no measurements were directly correlated with positions the thruster and only general relationships were observed.

Analysis of the plot yields that larger portion of 275 eV ions are detected near the right of the discharge channel centerline than the left side even though it is slightly further and at a higher angle of incidence. Since the cathode is physically in between the left side of the discharge channel and TOPAZ, it is likely this blocked a significant number of beam ions emanating from left side of the channel from reaching TOPAZ.

5.2.4 Conclusions on the BHT-600 Cluster Measurements with TOPAZ

Several interesting phenomena were observed with TOPAZ on the BHT-600 cluster that has never been measured for a Hall thruster cluster-configuration before. A peak current was measured at an energy-to-charge ratio of 270 eV/q, a value slightly below the 300 V operating voltage of the cluster. Beam ions were found to maintain their pathway from the cluster into the far-field plume 1 meter directly downstream. The annular shape of the discharge channels was found to affect the azimuthal-energy measurements downstream. A very slight focusing must exist since the measured width of the peak about the discharge channels for the left- and right-two thrusters was less than the apparent angle from the measuring point at TOPAZ.

Azimuthal angle-energy measurements yield that a majority of beam ions with energy-to-charge ratios near the discharge voltage were detected between the cathodes at the cluster face. However, significant high-energy ions with energy-to-charge ratios up to

425 eV were detected along the centerlines of the left- and right-two thrusters. CEX collisions which reduce the ionic charge state but leave the energy unaffected are reasoned to have created these ions. At positions behind the cathodes, ions with energy-to-charge ratios as low as 175 eV/q were detected. A possible reason for this is the ionization of particles by the opposite cathode. Since the potential hill is decreased in this region, the ions accelerate to less energy than the beam ions.

Similar measurements were conducted on the lower left thruster, however, low-energy ions were not observed beyond the cathodes. This concurs with the previous theory, since cross-ionization does not occur with the operation of a single thruster. Near the cathode and away from the centerline of the cluster, ions are detected with lower energies than those detected from near the centerline of the cluster. This implies that a slight yawing-torque is generated by the thruster *solely* due to the cathode placement. Cathode plume particles that are concentrated highly near the cathode orifice could decrease the energy of beam ions through elastic and charge-exchange collisions.

Another correlation exists between the ion energy-per-charge and the elevation angle. Ions detected from well below the horizontal plane tend to have lower energies. This is most likely due to the ions birth being significantly outside the acceleration region of the thruster. Since a similar energy relation was observed with the azimuthal angle, the following generalization can be made: Ions emanating from regions outside the thruster and towards the centerline in the far-field plume, and therefore having large azimuthal- and elevation-angle trajectories, tend to have lower energy-to-charge ratios. This is most likely due to the ions not gaining the full acceleration of the potential drop just outside the discharge channel.

Measurements of the single thruster operation at 60° yielded that a significant amount of beam ions are detected from this plume angle. However, the cathode physically blocks ions from arriving from the discharge channel near the plume interrogation point.

5.2.5 Conclusions on the Operation of TOPAZ with the BHT-600 Cluster

While the phenomena observed with TOPAZ is interesting, the measurements displayed important characteristics of operation of the electrostatic analyzer within the Hall thruster plume and its applicability as a plume-diagnostics tool. Since the analyzer displayed expected energy-to-charge profiles in the far-field plume, the instrument works well to profile the energy-to-charge ratio of beam ions. It is important to note, however, that energy-to-charge measurements are specific to the azimuthal angle and guiding plate settings of TOPAZ.

By sweeping through the guiding plate voltage and azimuthal angles of the instrument, as well as the deflection plate voltage, new measurement capabilities for plume diagnostics are demonstrated through TOPAZ. Particularly, the energy-to-charge ratio can be correlated with the trajectory of ions arriving at the interrogation point. The azimuthal angle measurements are most accurate, as the ion trajectory does not have to be altered, and the ion focusing results in a high resolution for this parameter.

Elevation angle correlations are also possible, however they are less accurate. Due to probable Debye shielding of the guiding plate, a shift in the elevation angle profiles was measured. Through single-thruster measurements a total shifting of approximately -19° was noticed. Since this is a property of the plasma density, and hence the plume angle, since centerline measurements are likely to have higher plasma densities.

Measurements on the thruster were attempted with large open-area fraction grounded grids placed at the entrance to decrease the plasma density (and hence the Debye shielding) within TOPAZ. Unfortunately, this resulted in an undetectable signal. From a design perspective, an instrument with a lower analyzer constant would significantly increase the current at the exit of the gap. By utilizing a grounded grid at the entrance of this instrument, possibly the Debye shielding effect on the guiding plate could be mitigated while still receiving an appreciable signal at the exit of the gap.

5.3 Capabilities and Improvements on TOPAZ

With the electrostatics, TOPAZ can determine the energy-to-charge ratio and the azimuthal and elevation angles of ions. However, as an energy analyzer, the instrument is unable to discriminate the charge or mass of these particles. Hall thrusters were shown in the late 1990s to have significant populations of multiply-charged ions in the plume.¹⁰² This represents an efficiency loss for the thruster, since the ionization energy per charge increases beyond singly-charged xenon, krypton, and other common propellants utilized for Hall thrusters. Multiply-charged ions are also accelerated to exceedingly high energies, and therefore present significant risk to spacecraft components interacting with the plume particles.

To augment the capabilities of TOPAZ, a mass analyzer was added. The next chapter describes the design process (which is much simpler since the design is inherent) experimental characterization, and measurements on the BHT-600 cluster with the mass analyzer. The mass analyzer in congruence with the electrostatic energy analyzer makes TOPAZ a powerful far-field plume diagnostics tool.

CHAPTER 6: THE ADDITION OF A MASS ANALYZER FOR TOPAZ

The previous chapters have focused on the energy plume diagnostics on Hall thrusters. As stated previously, plasma transport properties and ionic charge states are also important for understanding how Hall thrusters work and for improving their performance.⁴⁸ Therefore, to maximize the capability of TOPAZ as a plume diagnostics instrument, a mass analyzer was added to the instrument's arsenal for plume characterization. Ultimately, the ion velocity distribution in each direction allows for any macro-property to be determined through integration of moments of the distribution.⁵⁴

Most mass spectrometers which utilize electrostatics measure the mass-to-charge ratio of detected ions. For measurements on heavy elements such as Xenon (131.3 amu) and Krypton (83.3 amu), measurements of propellant ions discriminates the charge-state since they are much heavier than other elements significantly present within the testing facility. Measurements of the mass-to-charge ratio m/q in combination with the energy-to-charge ratio E/q yield information on the velocity distribution, since a division of the latter by the former yields the energy-to-mass ratio E/m . For measurements of kinetic energy in non-relativistic frames, this is equivalent to half the square of the ion speed. The addition of angular measurements allows for the extraction of the velocity components. In this chapter, the selection, design, characterization, and measurements utilizing a mass analyzer in conjunction with TOPAZ is presented.

6.1 Mass Analyzer Selection

There are several types of mass-to-charge spectrometers. Similar the energy analyzers, they usually employ some type of ion-filtering technique to discriminate a small range of mass-to-charge values to be detected. Quadrupole analyzers, magnetic sectors, and time-of-flight mass spectrometers are common techniques for mass-discrimination of ions in plasmas. These methods including a novel idea, the Harmonic Oscillator, were considered for adaptation to TOPAZ.

6.1.1 Quadrupole Analyzer

The quadrupole analyzer is discussed briefly in Section 2.2.3.3. The extremely high mass resolution for the quadrupole analyzer made this method attractive for outfitting TOPAZ; however, the geometry of the top hat analyzer requires the mass analyzer to operate at multiple azimuthal angles. Since the quadrupole analyzer requires four rods to surround the pathway of detected ions, an array of poles would be required for the simultaneous detection of ions emanating from the gap at different azimuthal angles.

6.1.2 Magnetic Sector

As described in Section 2.2.3.1, the magnetic sector functions as a momentum selector by allowing ions within a small momentum-to-charge range to be detected. This in combination with energy-per-charge measurements allows for the direct measurement of velocity, for which the mass-to-charge ratio can be derived with the energy selection. The diagram in Figure 6-1 describes a possible design for a magnetic sector-type filter for TOPAZ.

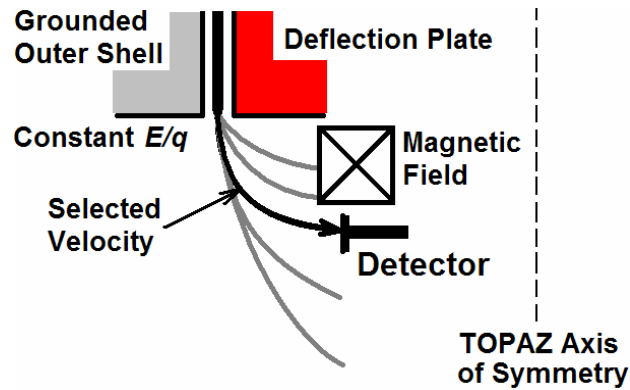


Figure 6-1: Integration of a magnetic sector-type filter for TOPAZ.

The magnetic field selects ions exiting the cap of a specific velocity to impact the detector. By varying the magnetic field strength, a profile of the velocity distribution is created. The combination of the electrostatic energy analyzer with the magnetic selector would allow TOPAZ to function like an $\mathbf{E} \times \mathbf{B}$ probe with, however, angular and an energy-to-charge ratio measurements.

A simple calculation reveals why the magnetic sector was not chosen as a mass analyzer for TOPAZ. The magnetic field strength required to turn singly-charged xenon ions of 275 eV energy over a radius of 5 cm is approximately 5500 Gauss (see Equation 2-2). This is exceptionally large. Considering the magnetic field required for Hall thruster operation is over an order of magnitude less,¹⁰³ a magnetic field of this strength would require significant current for running the electromagnets and shielding the contained, uniform field just outside the exit of the gap.

6.1.3 Harmonic Oscillator

The use of oscillating fields outside the gap of TOPAZ was theorized to select a mass-to-charge ratio of ions. By applying an orthogonal RF electric field to the ions inside a channel, ions of a specific mass-to-charge will have a specific resonance height

(based on their mass-per-charge) and distance (based on their velocity). By forcing ions to physically pass over a step, ions of a specific mass-per-charge could be selected by the frequency of the RF field. Variation of the frequency or magnitude would yield a mass-per-charge profile of the ions. The benefit of this filter arises if the physical step is axisymmetric and placed concentrically with the gap exit since all azimuthal angles are selected simultaneously through the biasing of one plate. Jessica Brooks designed a Harmonic Oscillator for TOPAZ, and found distances on the order of 10 cm would be ideal, however the mass-per-charge resolution was low. Also, the extension of ion trajectories beyond the gap exit results in their focusing in the azimuthal direction decreasing the azimuthal resolution.

6.1.4 Time-of-Flight

The final method of mass-to-charge ratio selection is the measurement of the time-of-flight (TOF) of the ions. The velocity could be determined if the path length is known. This analyzer requires the use of a high-speed on/off gate for the ions, and accurate measurements of arrival time versus the start time of ion flow. Most TOF instruments utilize electrostatic plate which, when biased, prevent ion flow to the detector. By grounding the plate for a small length of time (i.e., pulsing the gate), ions are allowed to flow towards the detector. A measurement of the difference in time between the “opening” of the gate and detection time is the time-of-flight.

The time-of-flight method has several advantages. Since the length in time for the slowest ion to arrive at the detector is on the order of microseconds, the entire mass-per-charge profile is almost instantaneously measured. A disadvantage, however, is the sharp decrease in the current detected at the exit. Therefore, many samples must be measured to

create an accurate distribution. This slightly counterbalances the instantaneous measurement capability. In general, however, for high density plasmas an accurate profile can be generated in under a second. This is significantly faster than other techniques which require sweeping through plate voltages or frequencies to measure a distribution.

6.1.5 Summary of Considered Techniques

Table 6-1 displays a table of the mass-analyzer designs considered for TOPAZ.

Detection Scheme	Advantages	Disadvantages
Quadrupole Analyzer	<ul style="list-style-type: none"> • Many commercial products available • Excellent mass resolution 	<ul style="list-style-type: none"> • Incorporation into TOPAZ with azimuthal discrimination requires complex design
Magnetic Sector	<ul style="list-style-type: none"> • Relatively simple approach • Good mass resolution 	<ul style="list-style-type: none"> • Massive • Requires large magnetic field • Containment/design of field is tricky
Harmonic Oscillator	<ul style="list-style-type: none"> • Novel idea • Easily adaptable for TOPAZ 	<ul style="list-style-type: none"> • Novel idea • Requires precise machining • Mass selection not fully understood, low Resolution
Time-of-Flight	<ul style="list-style-type: none"> • Very fast scanning of entire mass profile • Heritage in PEPL • Already built-in to TOPAZ 	<ul style="list-style-type: none"> • Fast voltage-pulsing electronics & detection scheme required

Table 6-1: Mass-Analyzer options for TOPAZ.

A simple detection scheme was desired for TOPAZ, and the time-of-flight method was selected, due to its heritage in the laboratory on similar thrusters. This method has some heritage with Hall thruster plume diagnostics. A separate time-of-flight region (not requiring a pulsing of ions) could be created with TOPAZ; however a simpler method

involving utilization of the top hat plate as the gating plate was employed. Since the top hat plate controls transmission of the instrument, this plate could function as the on/off switch for ion flow to the detector. The channel length from the aperture to the detector functioned as the drift space for measuring the time-of-flight. An advantage to this method is that no modification is required of TOPAZ. The time-of-flight hardware is inherently “built-in.” It is interesting to note that with the use of time-of-flight in this fashion, a simultaneous measurement of energy-to-charge, two angles, and the mass-per-charge are conducted through the clever geometry of the top hat analyzer and electric fields only. In the following section, the principles of time-of-flight are presented before the characterization and experimental measurements utilizing this method of mass selection.

6.2 Time-Of-Flight Principles

First the underlying equations for time-of-flight calculations are presented. Then the relationship to TOPAZ geometry is established. This allows for determining how the design parameters for TOPAZ affect time-of-flight measurements.

6.2.1 Theory of Operation

Time-of-flight mass spectrometers utilize the principle that particles of different masses with the same energy E travel with different velocities inversely proportional to the square root of the mass:

$$v = \sqrt{\frac{2E}{m}} \qquad \text{Eqn. 6-1}$$

The time-of-flight t_{TOF} of the particle over a prescribed distance d_{TOF} is therefore directly proportional to the square root of the particle mass:

$$t_{TOF} = d_{TOF} \sqrt{\frac{m}{2E}} \quad \text{Eqn. 6-2}$$

Since TOPAZ filters the energy-per-charge E/q , the mass-to-charge ratio m/q can be written in terms of the energy-per charge through algebraic manipulation:

$$\frac{m}{q} = 2 \left(\frac{t_{TOF}}{d_{TOF}} \right)^2 \left(\frac{E}{q} \right) \quad \text{Eqn. 6-3}$$

To determine the time-of-flight t_{TOF} of a particle, the ion flow to the detector is turned “on” and “off” by use of a top hat plate which acts as an electrostatic gate. To “open” the gate, the top hat plate is biased with a positive voltage such that the transmission of ions through the channel to the detector is maximized. To “close” the gate, the voltage of the plate is biased to a negative voltage (or grounded if possible, however, as previously determined with TOPAZ, a significant transmission of ions occurs with a grounded top hat plate). In this state, no ions are able to travel through the aperture and arrive at the detector.

6.2.2 Pulse Length

The use of the top hat plate as a gate for the ion flux to the detector requires voltage pulses, such that the pulse width is long enough for the slowest ion of interest to travel across the gate. However, if the gate is biased “on” for too long, a wider range of ions traveling with different velocities (i.e., different masses of the same energy) arrive at the detector at the same time. This, in effect, broadens the peaks in the mass distribution. Therefore the smallest pulse width possible is desired to maintain the best mass

resolution while not sacrificing a loss in signal from the slowest (and largest mass-per-charge) ion.

Equation 6-4 depicts the required pulse width t_{gate} required to allow the slowest ion to traverse across the gate distance d_{gate} .

$$t_{gate} > d_{gate} \sqrt{\frac{(m/q)_{max}}{2(E/q)}} \quad \text{Eqn. 6-4}$$

The total distance the ion travels from the entrance of the gate (the leading edge of the aperture) to the detector is expressed in Equation 6-5.

$$d_{TOF} = R_C \theta + \frac{\pi R_C}{2} + \Delta x \quad \text{Eqn. 6-5}$$

The first term represents the flight of the ion from the leading edge of the aperture entrance to the axis of symmetry of TOPAZ over the centerline along the radius of the aperture. For this term it is assumed $R_C \approx R_p$. The second term denotes the traveling of the ion from the axis of symmetry to the exit of the channel turning a total 90° along the channel radius. The final distance Δx is the path length between the exit of the gap and the entrance into the detector. For TOPAZ geometry, the total TOF distance is expected to be approximately 18.05 cm if the detector is placed directly under the instrument (approximately 1 cm from the exit of the gap).

6.2.3 Relation to the Ideal Top Hat and Mass Resolution

Equation 6-5 can be written in terms of the analyzer constant for the ideal top hat analyzer (see Equation 3-8) if Δx is considered negligible:

$$d_{TOF} = R_C \left(\frac{1}{\sqrt{K}} \right) + \frac{\pi R_C}{2} \quad \text{Eqn. 6-6}$$

For a pulse that is long enough to allow slow propellant ions (e.g., Xenon or Krypton) to just cross the gate length t_{gate} , faster ions of the same energy (e.g., Oxygen or Nitrogen) will have a mass-per-charge uncertainty equivalent to the difference in the values deduced for ions with time-of-flight distances d_{TOF} including and excluding the gate distance d_{gate} . The reason is that a quick ion can traverse the entire gate just before the gate is closed, while a slightly slower ion just traverses the distance after the gate, however both ions arrive at the detector at the same time. This inherently gives two ions with slightly different mass-to-charge ratios the same measurement. Formulation of this scenario allows for an approximation of the mass resolution with χ representing the non-dimensional parameter of the gate distance over the entire time-of-flight distance, d_{gate}/d_{TOF} .

$$\frac{\Delta m}{m} = \frac{4\chi - 2\chi^2}{\chi^2 - 2\chi + 2} \quad \text{Eqn. 6-7}$$

For small values of χ (i.e., $\chi < 0.15$), the above expression can be approximated:

$$\frac{\Delta m}{m} \approx 2\chi \quad \text{Eqn. 6-8}$$

The above equation dictates that small gate distances with respect to the time-of-flight distance are desirable for high mass resolution. For the dimensions of TOPAZ with the modifications from the ideal top hat analyzer, the approximate mass resolution error-bar is 27.7% or $\pm 13.9\%$ from the mean value. For a bell curve-type distribution, a full-width half-maximum (FWHM) would be approximately half this value yielding a mass resolution of 13.9%. This represents the worst-case scenario of detecting light ions in the same profile with heavy propellant ions. The resolution suggests that charge-state discrimination should be possible for charges of 1 – 4; however the discrimination of

lighter elements like nitrogen and oxygen would be difficult due to peak broadening. This Equation 6-8 can be related to the ideal top hat analyzer through the analyzer constant.

$$\chi = \frac{2}{2 + \pi\sqrt{K}} \quad \text{Eqn. 6-9}$$

By combining Equation 6-8 and 6-9, the mass resolution is related to the analyzer constant for the ideal top hat analyzer.

$$\frac{\Delta m}{m} \approx \frac{4}{2 + \pi\sqrt{K}} \quad \text{Eqn. 6-10}$$

For large analyzer constants ($K > 30$), the expression above can be further simplified:

$$\frac{\Delta m}{m} \approx \frac{4}{\pi\sqrt{K}} \quad \text{Eqn. 6-11}$$

The expression above indicates the mass resolution is inversely proportional to the square root of the analyzer constant. Therefore, ideal top hat analyzers with high analyzer constants are desired for precise mass resolution if the time-of-flight technique utilizes the top hat as a gating plate and the channel for the drift region.

6.3 Experimental Characterization of the Mass Analyzer

To verify the operation of the time-of-flight analyzer, the ion-beam facility described in Section 4.2.1 was utilized. Two factors need to be determined for the time-of-flight operation of TOPAZ – the effective time-of-flight distance and the electronics delay time (specific to the ion-beam setup).

6.3.1 Experimental Setup

TOPAZ was placed two meters downstream of the ion beam, and ions of known energy and composition were flown through the instrument to a K&M Electronics model 7550m channel electron multiplier (CEM). Unlike the previous energy-analyzer characterization, the composition of the beam (i.e., the mass of particles emitted), was important for the measurements. The CEM has an aperture of 1.0 cm. Since the azimuthal resolution was irrelevant to the time-of-flight measurements, the full size of the aperture entrance was utilized to maximize the detection of ions. As stated previously, the CEM detects ions by accelerating them into a highly emissive secondary-electron surface. Figure 6-2 describes the electrical schematic and controlling instrument setup for testing the TOPAZ time-of-flight mass spectrometer.

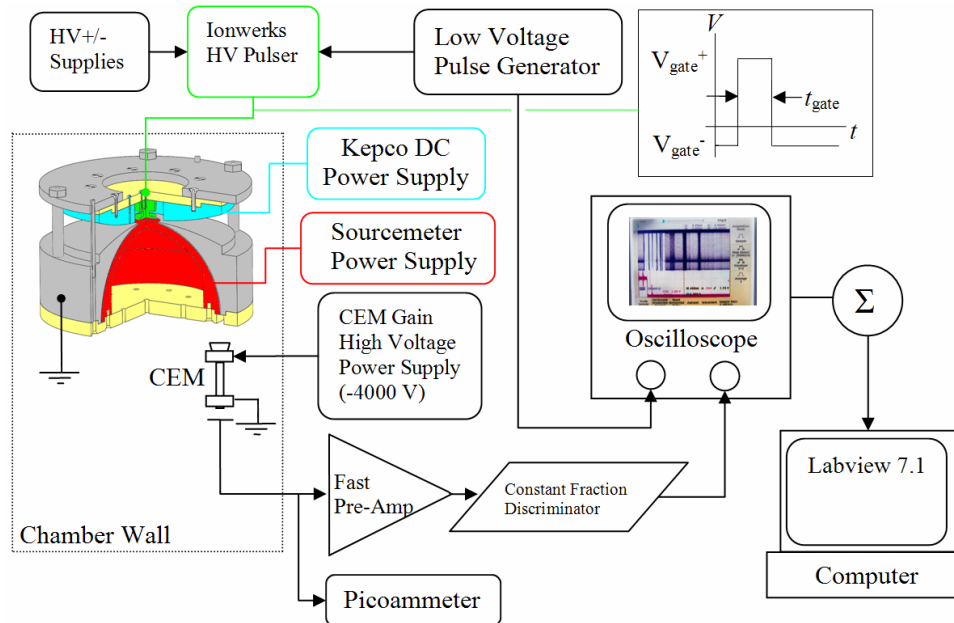


Figure 6-2: Electrical schematic of controlling electronics and data system for the time-of-flight mass spectrometer for TOPAZ.

The energy-per-charge of ions detected by the CEM is determined by the voltage of the deflection plate (in red) set by the Sourcemeter power supply. The guiding plate

potential (in turquoise) is controlled by a Kepco DC power supply. The voltage is set, such that the maximum number of ions fly through the aperture to be detected. The top hat plate potential (in green) is set by the Ionwerks High-Voltage pulser. A low voltage pulse generator drives the pulse width and frequency, while external high-voltage power supplies set the upper and lower peak voltages (V_{gate}^+ and V_{gate}^-). The pulse generator sends signals to the oscilloscope for monitoring the start time of the pulse.

After an ion flies into the CEM, a pulse is created due to the avalanche of secondary electrons emitted. The gain for this response is controlled by the high-voltage power supply. The pulse exits the chamber, and the current is converted into a voltage pulse via the fast pre-amplifier. A constant fraction discriminator shapes the pulse into a TTL signal with constant width (approximately 50 ns) and voltage peak (1.7 V). This allows for the equal measurement of each pulse. The signal is sent to the oscilloscope, and the delay of detected ions with respect to the pulse generator is measured. The voltage as a function of time is summed over 2000 samples through LabVIEW code and saved on a personal computer.

6.3.2 Experimental Procedure

The ion beam energy was varied from 1 keV to 5 keV in 1 keV increments. Three gases were used as ion sources: krypton, xenon, and air. Krypton and xenon are common propellants used in Hall thrusters and ion engines. Air is composed of light gases, and therefore provided a challenging medium for time-of-flight measurements, since the velocities are much higher over the same energy range.

6.3.2.1 Optimum Top Hat Voltages

Before time-of-flight measurements could be conducted, the optimum top hat voltages which control the flow of ions to the detected had to be determined. The voltage which generated the most current (or counts) would be selected as the “on” voltage for the top hat plate. The nearest voltage which prevented the transmission of ions to the detector was used as the “off” voltage. Figure 6-3 displays a plot of the counts as a function of the top hat voltage for a 1 keV beam setting.

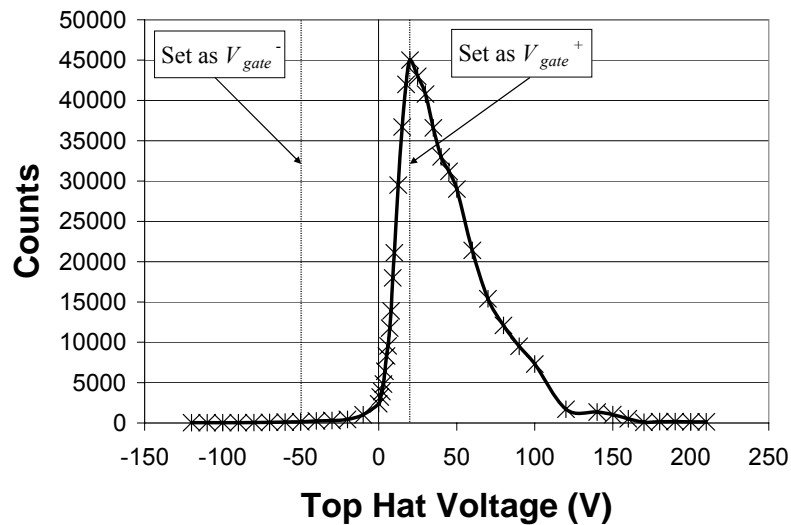


Figure 6-3: Detection of ions for a varying top hat voltage with a 1 keV beam.

The above plot is similar to the response for the previous top hat plate characterization (see Figure 4-6). The asymmetric profile indicates a negative bias would be the best choice for the “off” voltage, since this would require the smallest peak-to-peak distance for pulse signals. For many time-of-flight instruments, the “on” voltage bias is 0 V, while the “off” voltage is a large negative or positive voltage. Since the geometry of TOPAZ was modified from the ideal analyzer, the maximum transmission is produced with a biased top hat plate. A grounded voltage could be used for transmission,

however, since a maximized sampling per unit time is desired, a biased voltage is utilized for the maximizing the transmission of ions through the aperture.

6.3.2.2 Time-of-Flight Operation

For all measurements, a “zero” profile is first taken with the deflection plate grounded. Spurious ions detected by the CEM, as well as transient signals generated by the pulser, are recorded and subtracted from measurements of mass spectra with the deflection plate biased. Figure 6-4 displays a sample plot of the voltage profile generated for a 1 keV beam of krypton ions summed over 2000 samples.

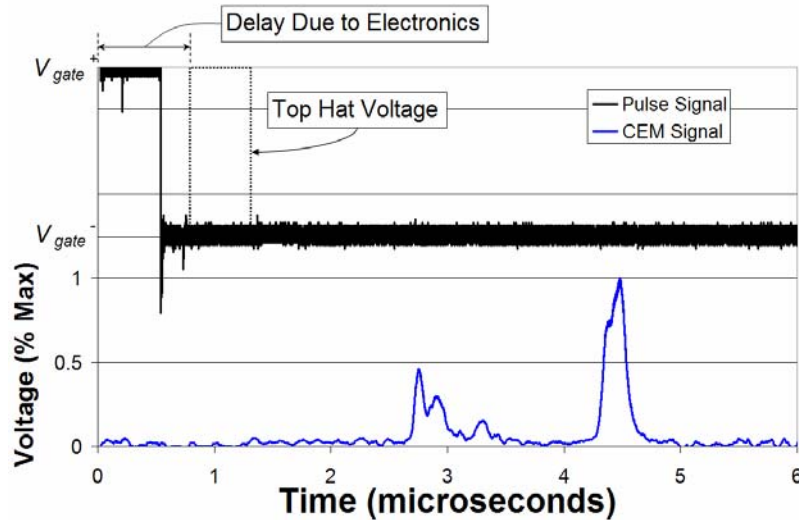


Figure 6-4: Sample voltage-time profile for a 1 keV krypton ion beam.

An important artifact of the time-of-flight measurements is the inherent delay in electronics used for the voltage-biasing. Since the measurements are on the order of microseconds, the difference in signal between the pulser and the time the top hat voltage is biased is significant. The delay time is a variable that must be accounted for the conversion of time-of-flight profiles into mass-per-charge distributions.

A boxcar average over 50 nanoseconds is performed over the CEM signal to smooth data and filter noise introduced by the cabling and Picoammeter. This length in average was chosen since the peak detection and width were not significantly altered, while the noise variance was greatly reduced. Figure 6-4 displays four peaks from the left to the right corresponding with the Kr^{4+} , Kr^{3+} , Kr^{2+} , and Kr^{+} charge-states, respectively. The lowest voltage is received for the Kr^{2+} ion. There are a few possibilities for this which includes the lower species-fraction of Kr^{2+} as compared with Kr^{+} while the Kr^{3+} and Kr^{4+} ions have a longer transmission time since they travel faster across the gate and have a longer window of opportunity. Also, the CEM might yield a higher-percentage of detected ions for more-energetic particles. Although this prevents a direct measurement of species fractions, they were not required for the time-of-flight characterization of TOPAZ.

Since the elements of krypton in the time-of-flight profile have known mass-per-charges, the time-of-flight distance, l_{TOF} , can be reverse calculated by combining expressions for krypton ions of two different charges using Equation 6-2, and subtracting out the delay time. An expression for l_{TOF} is below:

$$l_{TOF} = \left(\frac{t_{Kr^{q+}} - t_{Kr^{r+}}}{\frac{1}{\sqrt{q}} - \frac{1}{\sqrt{r}}} \right) \sqrt{\frac{2E}{m_{Kr}}} \quad \text{Eqn. 6-12}$$

In the above expression the charge states of two peaks are represented by q and r . With the difference in the time-of-flights of each charge, the time-of-flight distance can be determined. If Equation 6-12 is utilized for the peaks in Figure 6-4 a time-of-flight distance of 18.7 cm is calculated. This correlates well with the geometry of the instrument. Subtracting the time-of-flight calculated for the Kr^{+} ions (through Equation 6-

12) from the measured value yields a delay time of 529 nanoseconds. This value is subtracted out of all the time-of-flight profiles before they are converted into mass-per-charge distributions.

To alleviate uncertainty in measuring mass-per-charge for light species and multiply-charged propellant ions, a separate measurement was made with a smaller pulse width for 3+ and 4+ charge states. A pulse width of 890 nanoseconds was utilized for TOF measurements of the first two charge states of xenon and krypton. For an aperture distance of 3.4 cm, this allows for a Xe^+ ion (the slowest particle measured) to travel underneath the full diameter of the top hat plate. For the lower mass-per-charge elements, the pulse width was varied from 130 – 650 nanoseconds.

6.3.2.3 Krypton Measurements

Figure 6-5 and Figure 6-6 describe the mass-per-charge profiles obtained for krypton gas.

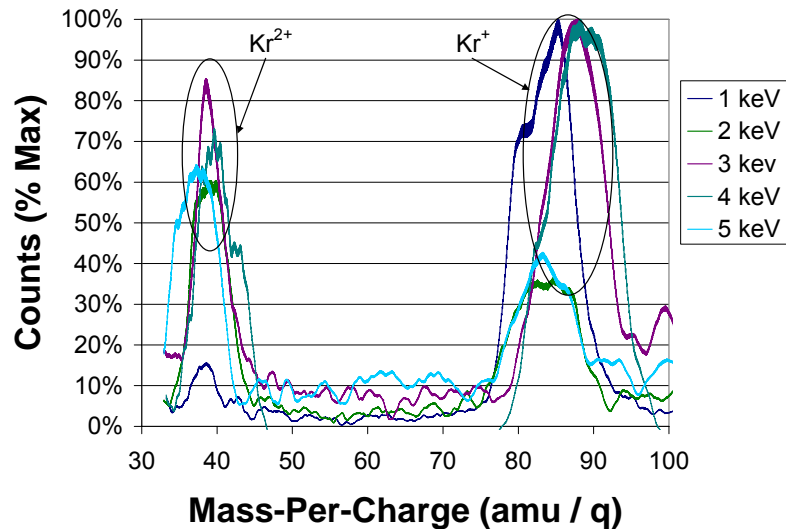


Figure 6-5: Mass-per-charge profile depicting singly- and doubly-charged krypton for various beam energies.

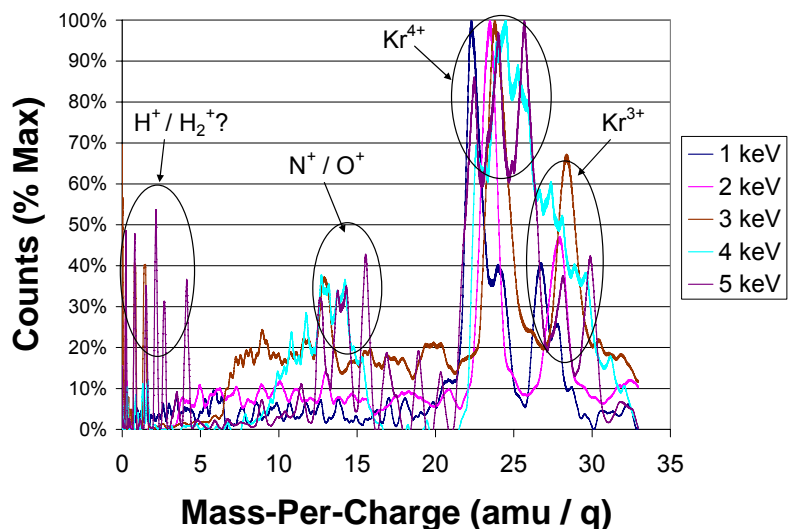


Figure 6-6: Mass-per-charge profile depicting multiply-charged krypton ions and lighter elements for various beam energies.

The first and second charge states of krypton are easily identified for all beam energies in Figure 6-5. The peak for the second charge state of krypton is slightly shifted towards the left (lower mass-per-charge). This is likely due to the pulse width being larger than the time-of-flight for Kr^{2+} ions across the gate. The delay time is calculated such that the Kr^{+} peak is correctly placed. Doubly-charged krypton ions, however, have an earlier average arrival time, since the pulse width is larger than their time of flight across the gate. Therefore, the peak arrival time of ions arriving at the gate is earlier, and the mass-per-charge is calculated as being less than expected.

Figure 6-6 depicts the higher charge states of krypton and lighter elements measured. The third and fourth charge states of krypton are more closely spaced than the first and second, since the mass per-charges are lower. The signal for the fourth charge-state is higher than the third charge-state in most cases. As previously stated, this is most likely due to the variance in the CEM gain as a function of impact-energy of ions on the ceramic. Peaks between 14 and 16 amu are measured for some beam energies. This could

represent background nitrogen and oxygen particles that have been accelerated through the ion beam. Below 5 amu, some of the measurements display possible molecular and atomic hydrogen ions; however, since the uncertainty in mass-per-charge is especially high for very light ions, this conclusion is taken with caution.

6.3.2.4 Xenon Measurements

As with krypton, xenon was utilized as propellant for the ion beam. Figure 6-7 and Figure 6-8 display plots of mass-per-charge for xenon for the first two charge states and lower mass-per-charge measurements, respectively.

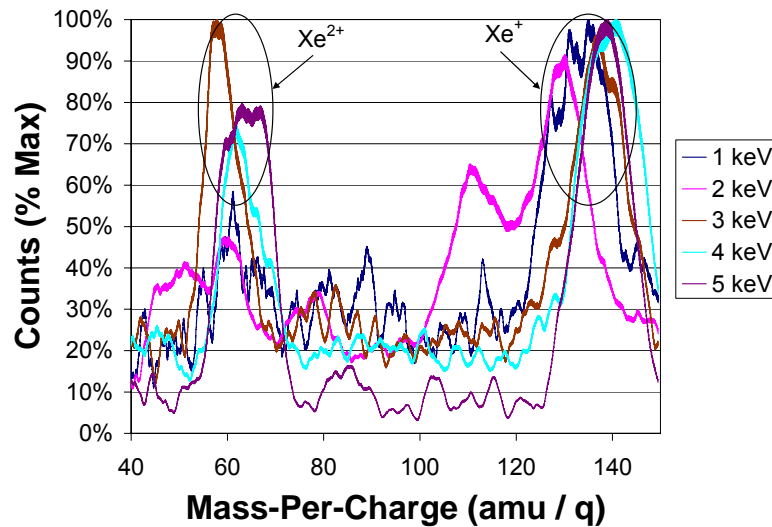


Figure 6-7: Mass-per-charge profile depicting singly- and doubly-charged xenon for various beam energies.

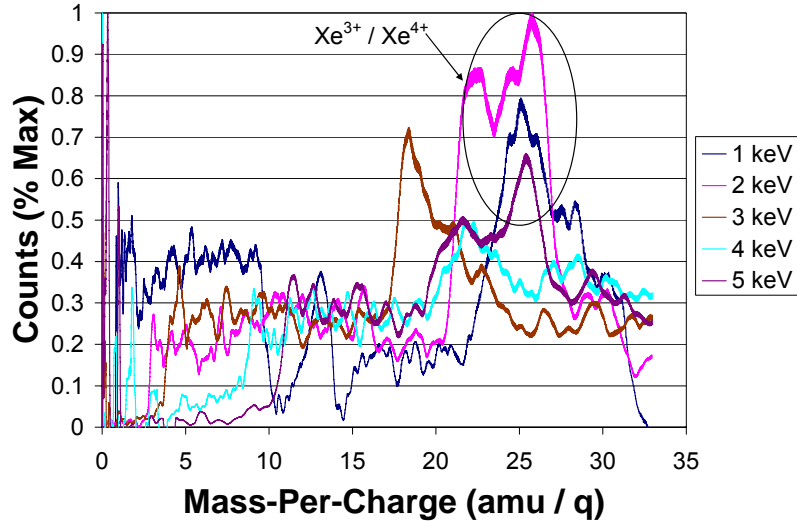


Figure 6-8: Mass-per-charge profile depicting multiply-charged xenon ions.

Figure 6-7 displays single and double-charge states of xenon as principle peaks at approximately 131 amu and 65 amu. For the 2 keV ion-beam setting, an anomalous peak is measured at approximately 110 amu/q. An attempt to discriminate the higher charge states of xenon was made in Figure 6-8; however, the noise overwhelmed the signal, and a clumping of the two charge states is observed. The noise below 20 amu is too significant to distinguish peaks corresponding to nitrogen, oxygen, and lighter elements. A lower mass flow-rate for the xenon propellant versus krypton is the likely reason the measurements have increased noise and less detected ions overall.

6.3.2.5 Air Measurements

Since lighter particles are the most challenging medium (and an easy setup) for time-of-flight measurements, time-of-flight measurements were attempted on the beam operating on air. Figure 6-9 displays the mass-per-charge profiles for air at energies from 2 keV to 5 keV.

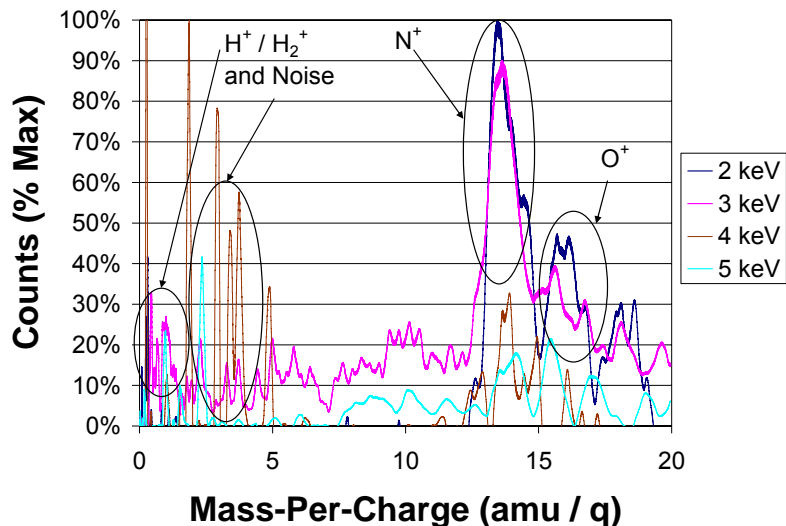


Figure 6-9: Mass-per-charge profile for air displaying nitrogen and oxygen ions at various beam energies.

For beam energies 4 keV and 5 keV, the required pulse widths were 150 and 130 nanoseconds. Since this approaches the rise and fall times of the pulse generator (20 – 60 nanoseconds), the inaccuracy of the top hat voltage-pulses was high, and a true “on” and “off” switch was not obtained over the aperture resulting in ambiguous measurements. Peaks corresponding with single-charge states of nitrogen and oxygen were measured for the 2 keV and 3 keV beam settings; however peaks representing the molecular ions (N_2^+ and O_2^+) were absent. Measurements of hydrogen ions are coupled with noise, and it is likely that other types of particles present in the chamber in of insignificant quantities that could be detected by TOPAZ.

6.3.3 Discussion

An overall time-of-flight distance of approximately 18.7 cm was determined for TOPAZ. The delay in electronics was calculated to be 529 nanoseconds; however this measurement is specific to the setup with the ion beam facility. Since the cable length and

choice of electronics affect the electronic delay time, the value must be calculated for the specific setup utilized.

Measurements on the krypton and xenon ion beams yielded the same charge-states that have been measured in Hall thruster plume operating on those same propellants.⁷⁰ For krypton the first two charge states were easily discernable for beam energies of 1 – 5 keV. The slight shift to the left for the doubly-charged krypton and xenon peaks is attributed to the optimization of the pulse width for the singly-charged species. A similar effect of peak-shifting is seen in the mass-per-charge profiles for the multiple-charge states of krypton and xenon in Figure 6-6 and Figure 6-8, respectively.

Figure 6-6 depicts the count obtained for the fourth charge-state of krypton is significantly higher than the third charge-state. This is likely due to the impact energy of the Kr^{4+} being significantly higher than the Kr^{3+} (i.e., $4E$ versus $3E$, where E is the beam energy). Since the CEM operates on an avalanche effect created from secondary electrons emitted by the first impact, the higher energy ions will generate more electrons, and the pulse is more likely to be detected by the constant fraction discriminator. For this characterization, the number of counts for each species was of little interest and a very large CEM voltage of -4000 V was utilized to maximize the sensitivity. For experimental measurements with TOPAZ, a CEM which offers approximately the same overall gain for particles of different energies should be used.

Measurements on xenon yielded easily discernable first- and second-charge states accelerated by the ion beam; however the third- and fourth-charge states were less defined than that of krypton. It is likely that the mass flow rate (not directly measured)

for krypton was slightly higher than for xenon and there was a lower sampling rate, resulting in a larger signal-to-noise ratio for these measurements.

The measurements of the ion beam utilizing air propellant indicate discerning nitrogen and oxygen was possible with the 2 keV and 3 keV beam settings. Above 3 keV, obtaining an accurate signal and providing precise pulse-voltages for the top hat with short pulse widths was difficult. Nitrogen and other background particles present in the chamber have been detected emanating from Hall thrusters.⁹⁸ Since the Hall thrusters currently operate at lower energies, it is possible TOPAZ can measure these elements if present in significant quantities in the chamber.

6.3.4 Conclusions on the Time-Of-Flight Characterization of TOPAZ

Measurements with the ion beam indicate the effective time-of-flight distance for ions is approximately 18.5 cm. This agrees with the geometry of the analyzer. The delay time of approximately half a microsecond was determined based on the time-of-flight distance and velocity of the ions; however this measurement is specific to the equipment used for the ion beam facility. Measurements inside the Plasmadynamics and Electric Propulsion Laboratory, for example, would most likely require a longer delay time, since the cable lengths are much longer inside the larger chamber.

The instrument was shown to measure multiple charge states of xenon and krypton for energies well above the current discharge voltage of most Hall thrusters. Since Hall thrusters accelerate ions to lower velocities, the time-of-flight measurements should be more accurate since the required pulse width is longer and the time-of-flight for the ions is longer as well.

An estimation of the effective mass-to-charge resolution can be made by measuring the full-width half-maximum of the peaks observed. For the Kr^{1+} the resolution is approximately 11.5%, while Xe^{1+} the resolution is approximately 12.0%. This indicates measurements of the charge states for propellant ions are possible; however individual species recognition (within a couple amu) would be difficult.

A possible reason for this is the geometry of the instrument. Since ions enter across the aperture across most of the diameter (see Figure 3-17), the length of time the ion is within field generated by the top hat plate varies as a function of the ion's distance from the centerline. Ions which enter the gap along the centerline of the instrument experience the field in the aperture for the longest period of time, while ions that enter the aperture through the fringes only briefly are affected by the top hat voltage. Since the top hat turns the transmission of ions on and off, ions that enter through the fringes of the aperture have a shorter effective time-of-flight distance l_{TOF} than ions along the centerline. Ions along the fringe can briefly pass over the aperture while the gate is "on" at the end of the pulse, while ions along the centerline must cross the largest distance of the aperture while the gate is "on" the entire length. This effectively increases their time-of-flight distance with respect to the fringe ions and results in broadening of the peaks in the mass-per-charge profiles. This also causes the ion peaks to not align exactly with the correct m/q values; however this can be accounted for with a modification of the effective time-of-flight distance as a function of ion velocity (which is directly measured).

Although the geometry of TOPAZ prevents the time-of-flight measurements from being a highly accurate mass spectrometer, the instrument can depict the charge state of heavy ions, which is of great interest for plume diagnostics. Ionization fraction describes

the ionization efficiency of Hall thrusters as well as the expected energies of far-field plume ions which can interact with other spacecraft components.

The next section describes time-of-flight measurements through TOPAZ on the BHT-600 cluster. The combination of energy-to-charge, mass-to-charge, and two angular measurements allows for significant insight into far-field plume properties of Hall thrusters including *in-situ* measurements of the velocity distribution of each species.

6.4 Time-Of-Flight Measurements on the BHT-600 Cluster

Mass analyzer measurements on the BHT-600 cluster were conducted with a similar setup as with the energy measurements. A review of the setup (with some slightly different hardware) is presented, followed by the measurements, and discussion of the data. It is important to note that the purpose of the measurements was to validate and showcase the measurement capabilities of TOPAZ as well as uncover interesting phenomena present in the plume (with capabilities specific to TOPAZ) rather than conduct an exhaustive characterization of all regions of the plume as a function of operating conditions of the thruster.

6.4.1 Experimental Setup

All measurements on the BHT-600 cluster were conducted in the Large Vacuum Test Facility (LVTF) discussed in Section 5.1.1. TOPAZ was placed in a similar configuration as previously done for the energy measurements at a distance one meter downstream of the cluster. Two perpendicularly mounted linear tables allow for multiple thruster angles to be interrogated by TOPAZ as described in Figure 5-6. For single thruster measurements, the pressure was maintained at approximately 1.9×10^{-6} Torr and

at 4.1×10^{-6} Torr during cluster operation. As with the previous measurements, the thrusters were operated at 300 V and 2 A, with 2.5 mg/s and 0.5 mg/s anode and cathode flow rates on xenon, respectively.

A thermocouple was utilized to monitor the temperature of TOPAZ, and during all measurements the temperature remained between 20 – 55°C. For the time-of-flight (TOF) measurements, a similar setup as with the TOF characterization was utilized, however some slightly different hardware was employed. Figure 6-10 displays the electrical component diagram for measurements in the LVTF.

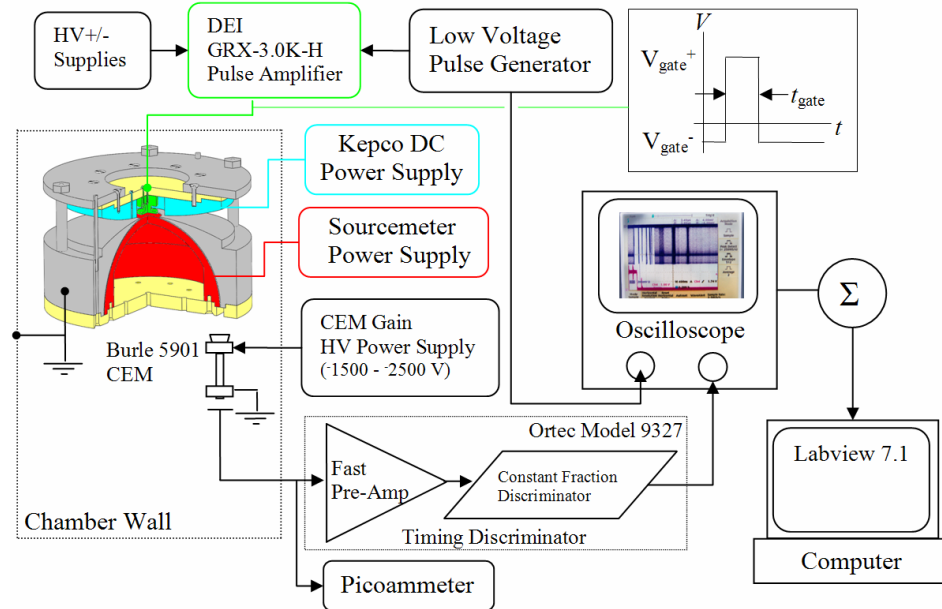


Figure 6-10: Schematic of electrical components utilized for time-of-flight measurements in the LVTF on the BHT-600 cluster.

As with the TOF characterization, a low voltage pulser drives the pulse amplifier, however Directed Energy, Inc. GRX-3.0K-H pulse amplifier was employed for measurements within the LVTF. Also a new Burle 5901 Magnum Electron Multiplier was employed which did not require very high voltage biasing to power (-1500 V – -2500 V versus -4000 V for the K&M Electronics model 7550m CEM) for operation. This

CEM also has an approximately equal detection efficiency which is independent of the charge state (or impact energy) of the particle on the detector. A picture of the CEM with the grounded enclosure is displayed in Figure 6-11. A grounded mesh with an 80% open-area fraction covers the 1 cm aperture on the grounded enclosure.

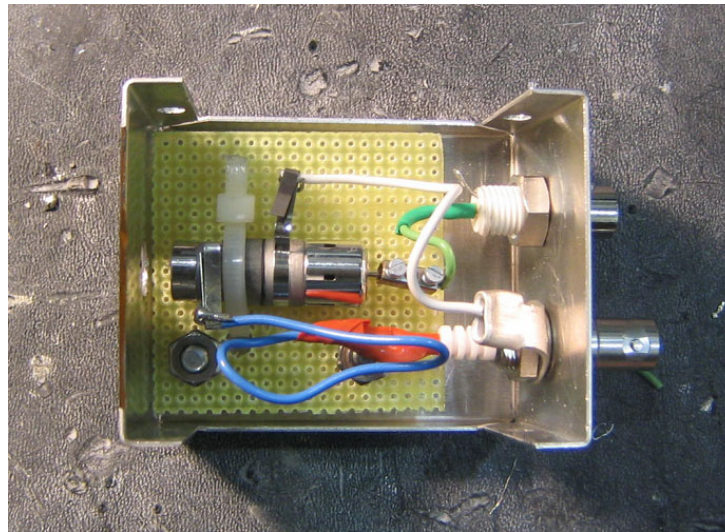


Figure 6-11: Burle 5901 Magnum Electron Multiplier with grounded enclosure.

An Ortec Model 9327 timing discriminator is utilized to convert the CEM pulses into TTL voltage signals with 50 ns pulse widths, and voltage heights of 1.7 V. The signal is sampled and summed up through a Tektronix TDS 3034B Oscilloscope and LabVIEW 7.1 code.

6.4.2 Experimental Procedure

Measurements were conducted for varying plume angles from 0° - 20° in increments of 10° for the cluster and single thruster operation. The low current received at 20° plume angle for the single thruster operation, however, was unrepeatable and therefore discarded. TOF measurements were conducted for energies between 0 – 650 eV, while the azimuthal and elevation angle of ions being detected is changed through the

detector position and variation of the guiding plate potential, respectively. Operation of the single thruster as well as the full cluster allowed for comparison of their plume properties. For all measurements, the thrusters were operated for 10 minutes until a stable discharge voltage and current settings were achieved. Figure 6-12 displays a picture of the cluster operating with TOPAZ one meter downstream the centerline of the cluster.



Figure 6-12: Operation of BHT-600 cluster with TOPAZ placed one meter downstream inside the Large Vacuum Test Facility (LVTF).

TOF measurements are converted to mass-per-charge profiles through use of a TOF distance of 15.5 cm. This is slightly smaller than that measured with the TOPAZ TOF characterization; however, utilization of Equation 6-12 for the ions emanating from the thruster yielded this value with a delay time of approximately 4 microseconds. Guiding and deflection plate potentials are converted into an elevation angle and energy-per-charge through the previously derived voltage relationships for TOPAZ.

6.4.3 Experimental Results and Discussion

For the cluster operation, several TOF profiles were conducted at various azimuthal angles, guiding plate, and deflection plate settings. For analysis of the data, two variables were correlated with the number of counts to generate contour plots. The counts are summed up over the dimensions not being displayed. This allows for relationship to be determined with respect to all the ions detected with TOPAZ. Measurements were conducted at plume angles of 0°, 10°, and 20° for the cluster operation, and at 0° and 10° for the single thruster operation. For single thruster operation, the lower-right thruster was operated (versus the lower-left thruster for the energy measurements in the previous chapter, see Figure 5-5). For each contour plot, the error-box is considered equivalent to the resolution of each parameter displayed. The energy-to-charge and azimuthal angle measurements have resolutions of approximately 2% and 1.3° respectively. The mass-to-charge resolution is considered to be 13% of the largest ion-species being measured – Xe⁺ at 131.3 amu – and is therefore approximately 17 amu.

6.4.3.1 Energy-To-Charge and Mass-To-Charge Measurements

By successively conducting TOF profiles for various energies, the energy-to-charge ratio can be correlated to the mass-to-charge ratio of specific ion species. For each of the plots presented, the color range is normalized with the maximum number of counts, allowing for a visual comparison of the amounts of each species with respect to each other.

Cluster Operation: 0° Plume Angle

Figure 6-13 displays a plot of the mass- and energy-to-charge relationship for the cluster operation at the 0° plume angle.

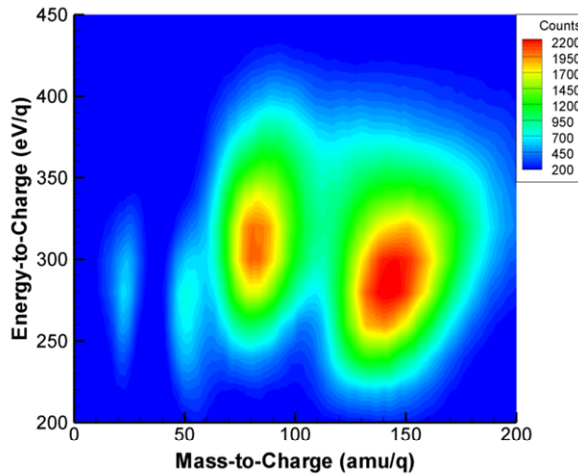


Figure 6-13: Energy-to-charge as a function of mass-per-charge for the cluster at a 0° plume angle.

Four peaks are visible in Figure 6-13. The three on the right represent Xe^{3+} , Xe^{2+} , and Xe^+ , from left-to-right. However there is a peak at approximately 30 amu. Since N_2^+ has a mass-to-charge ratio of 28 amu/q while Xe^{4+} has a ratio of 32.8 amu/q, and both are within the mass-to-charge ratio resolution, the species is indiscernible. This measurement could also possibly be a combination of both species. Manzella has documented evidence of N_2^+ emanating from the SPT-100 Hall thruster,⁶³ however King measured N^+ ions and negligible amounts of molecular-nitrogen ions.⁹⁸ Since Xe^{4+} has been detected in Hall thruster plume in small quantities,^{70,104} it is likely this is the ion species; however this conclusion is taken with caution. The first three charge-states of Xenon, however, are easily recognized due to the large mass of xenon particles. The singly-charged and triply-charged xenon ions have peak energy-to-charge ratios at approximately 280 eV; however the doubly-charged xenon has a slightly higher energy-peak at 315 eV. The overall

energy-to-charge distribution of the doubly-charged xenon is slightly higher as well. The likely cause is charge-exchange collisions which create particles with energy-to-charge ratios above the discharge voltage. Elastic collisions with other particles effectively broaden the energy distribution, since they allow for a variable amount of momentum-transfer (and therefore energy transfer) between the interacting particles.

Cluster Operation: 10° Plume Angle

Figure 6-14 displays a plot of the mass- and energy-to-charge relationship for the cluster operation at the 0° plume angle.

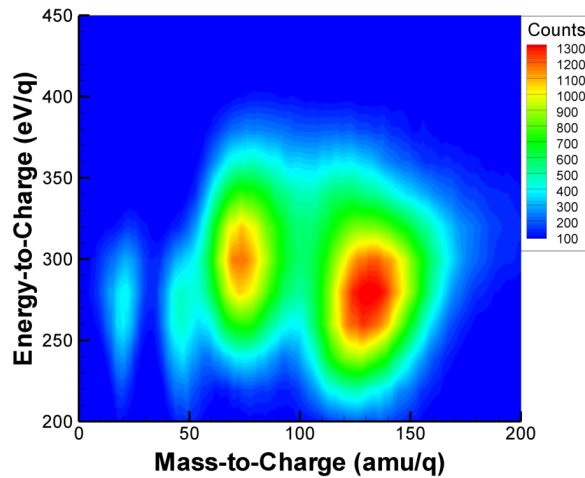


Figure 6-14: Energy-to-charge as a function of mass-per-charge for the cluster at a 10° plume angle.

The above plot displays similar energy distributions for each of the four species as with the 0° plume angle measurement. Overall the current received at this angle was significantly less. However measurements indicate a slightly higher percentage of Xe^{3+} and possibly Xe^{4+} . This agrees with previous measurements of higher concentrations of multiply-charged ions at slightly off plume angles.¹⁰⁵ Also, a similar trend of the 1st, 3rd, and 4th charge states of Xenon having peak energies slightly below the discharge voltage of 300 V, while Xe^{2+} has an energy distribution slightly higher than the discharge

voltage. It is likely Xe^{2+} ions tend to have a larger percentage of charge-exchange collisions from Xe^{3+} and Xe^{4+} ions, resulting in higher energy-to-charge ratios which results in energies with fractions above potential drop (i.e., $4/3$ and $4/2 \times$ (discharge voltage)). Collisions essentially “blur” the distribution resulting in an overall profile about this higher energy.

Cluster Operation: 20° Plume Angle

A distribution of the energy-to-charge versus the mass-to-charge ratio is shown in Figure 6-15.

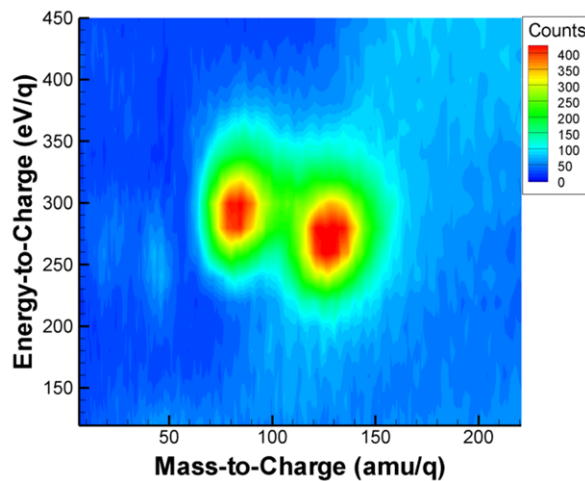


Figure 6-15: Energy-to-charge as a function of mass-per-charge for the cluster at a 20° plume angle.

A decreased transmission is noticed overall, as indicated by the maximum number of counts (400) versus the 0° (2200) and 10° (1300) plume angles. This results in a slightly larger signal-to-noise ratio for the measurements. The plot clearly indicates large quantities of Xe^+ and Xe^{2+} ; however a very small quantity of triply-charged xenon is detected, and an almost imperceptible amount of possible Xe^{4+} is measured in the plume. This data agrees with previous measurements on the well-studied SPT-100 – significant quantities of multiply-charged ions are detected at plume angles within 20°, however,

beyond this angle, the plume is composed of mostly singly-charged and some doubly-charged xenon ions.⁷⁶ The energy distributions, however, are similar to the 0° and 10° plume angles. The Xe^+ , Xe^{2+} , and Xe^{4+} ions have energy peaks slightly lower than the Xe^{2+} ions. As for the previous plume angles discussed, the Xe^{2+} could be more susceptible to CEX collisions in combination with momentum-exchange collisions resulting in an elevated energy distribution with respect to the other species of ions.

Single Thruster Operation: 0° Plume Angle

Measurements on the bottom-left thruster were conducted for 0° and 10° plume angles. Figure 6-16 displays the energy-to-charge versus the mass-to-charge for this thruster at a 0° plume angle along the cluster centerline.

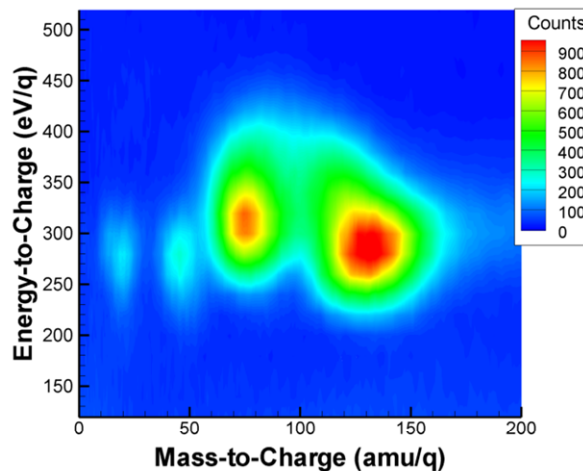


Figure 6-16: Energy-to-charge as a function of mass-per-charge for the single bottom-left thruster at a 0° plume angle.

Measurements on the single thruster yield similar species identification as with the cluster operation. The doubly-charged Xenon ions tend to have a slightly higher energy-to-charge ratio than the other species. It is interesting to note, however, a slight bifurcation exists where the Xe^{4+} is theorized to be measured. It is possible the smaller

area with the lower mass-per-charge is due to N_2^+ ions while the larger area is Xe^{4+} . This is below the mass-per-charge resolution, however, so no conclusions can be drawn.

Single Thruster Operation: 10° Plume Angle

A plot of the energy-to-charge ratio as a function of mass-to-charge is displayed in Figure 6-17 for the single thruster operation at 10°.

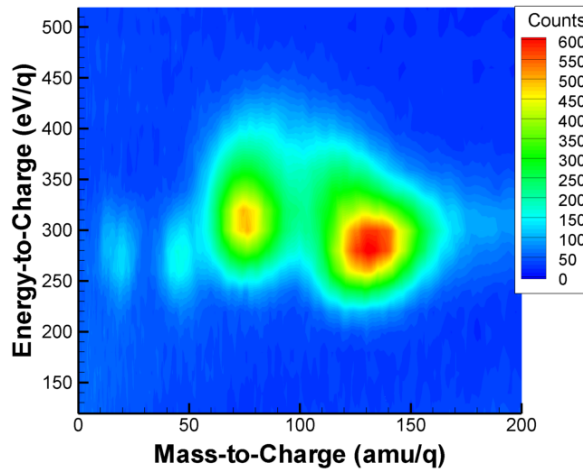


Figure 6-17: Energy-to-charge as a function of mass-per-charge for the single bottom-left thruster at a 10° plume angle.

As with the previous contour plots, each species has an energy distribution slightly below the discharge voltage except for doubly-charged xenon. In this plot, the bifurcation of the Xe^{4+} is also measured, indicating possible measurements of N_2^+ ions being ingested by the thruster and being accelerated - a result of facility effects. Another interesting measurement is the smaller percentage of Xe^{2+} measurements as compared with the cluster measurements at the 10° and 20°. Although more particles are detected with for the single-thruster measurement at 10°, versus the cluster measurement at 20°, a larger portion of doubly-charged ions is measured with the cluster. This indicates there is a higher population of doubly-charged xenon for cluster operation than for single thruster operation in the far-field plume. A possible reason for this is the use of four cathodes for

the cluster operation. Cross-pollination of electrons to the opposite discharge channels could increase the ionization rate and double ionization rates for propellant ions. Each discharge channel can receive electrons from four cathodes, resulting in a higher electron-neutral and electron-ion collision rate which generates more multiply-charged ions in the plume than with the single thruster operation.

Measurements on the azimuthal angle relation to the mass-per-charge can shed light on the trajectories of each species of propellant ion.

6.4.3.2 Azimuthal Angle and Mass-to-Charge Measurements

Measurements of the mass-per-charge as a function of azimuthal angle describe likely positions each species emanates from the thruster.

Cluster Operation: 0° Plume Angle

Figure 6-18 displays a plot of the mass-per-charge relationship with azimuthal angle for the cluster operation at 0°.

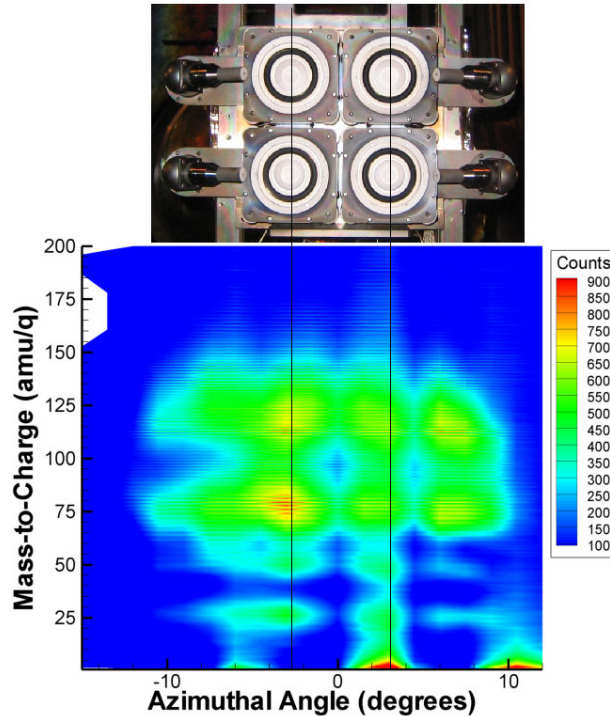


Figure 6-18: Mass-to-charge as a function of azimuthal angle for the cluster at a 0° plume angle. The cluster is pictured for azimuthal-angle reference.

The azimuthal angle has been placed on the x -axis for correlation with the thruster positions. The rows in plots above each correspond with the different mass-per-charge species identified in the previous mass-per-charge profiles. It is evident that the lower mass-to-charge ions mostly emanate from the discharge channels while the singly and doubly charged ions are detected from all parts of the thruster. The measurements indicate almost an equal amount of Xe^{2+} as with Xe^+ , however there is a slight preference for the detection of smaller mass-to-charge ratio ions, since they have a larger “window of opportunity” to cross the aperture within the pulse width. This is accounted for in the calculation of ion species fractions in a later section. When comparing the above figure to the energy-to-charge measurements with azimuthal on the cluster (see Figure 5-9), the energy-to-charge and mass-to-charge profiles can be compared with the emanating point

of the thruster. The lower energy-to-charge (175 - 300 eV) ions measured near the outsides of the cathodes correspond to singly- and doubly-charged ions, however along high energy peaks at the centerlines of the discharge channels, all charge states are measured.

Cluster Operation: 10° Plume Angle

As with the 0° plume angle, the mass-per-charge was correlated with azimuthal angle measurements at a 10° plume angle. Figure 6-19 displays this plot.

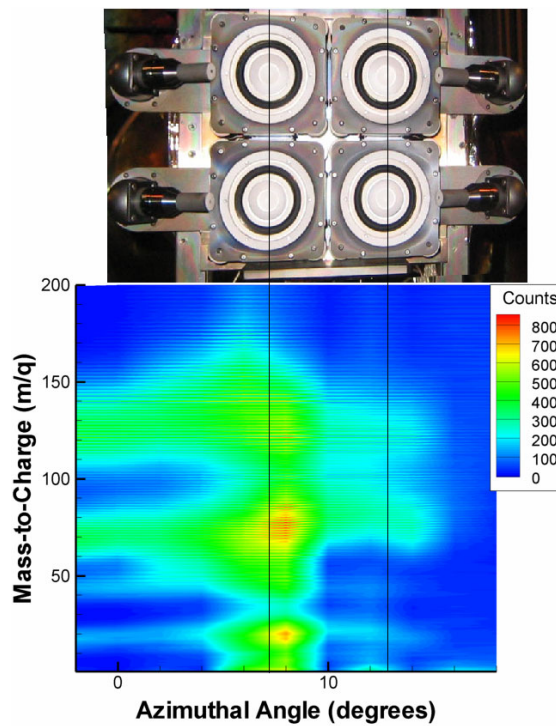


Figure 6-19: Mass-to-charge as a function of azimuthal angle for the cluster at a 10° plume angle. The cluster is pictured (and scaled for a 10° viewpoint) for azimuthal-angle reference.

The plot above shows a high dependence of which thrusters ions are detected from even at the slight plume angle of 10°. For this cluster plume angle, the left set of thrusters has an approximate individual-plume angle of 5° while the right-two thrusters

have an effective individual-plume angle of 15°. A higher amount of ions are detected from the left set of thrusters with the lower plume angle.

Unfortunately, the triply-ionized xenon ions blend in with the doubly-charged ions; however a higher detection rate of Xe^{2+} is measured at this slight angle. This agrees well with previous measurements on the SPT-100, for which measurements between 5 - 15° off the thruster plume yield multiply-charged ions at higher amounts than singly charged xenon.⁹⁸ Measurements from 9-11° from one meter downstream show evidence of charge exchange from $\text{Xe}^{4+} \rightarrow \text{Xe}^{3+}$ and $\text{Xe}^{3+} \rightarrow \text{Xe}^{2+}$ at these angles for this thruster. More information the different types of CEX collisions can be found in Ref. 98. Large amounts of $\text{Xe}^{4+}/\text{N}_2^+$ are detected from the left-two thrusters which are near this angular range. This indicates multiply-charged ions tend to be slightly “off-focus” from the thruster plane, while singly- and doubly-charged xenon ions tend to emanate from much wider range of plume angles.

Cluster Operation: 20° Plume Angle

A plot describing the mass-to-charge versus azimuthal angle is shown in Figure 6-20. A slight misalignment of -3.5° in the azimuthal angle is accounted for in the placement of the cluster with respect to the measurements.

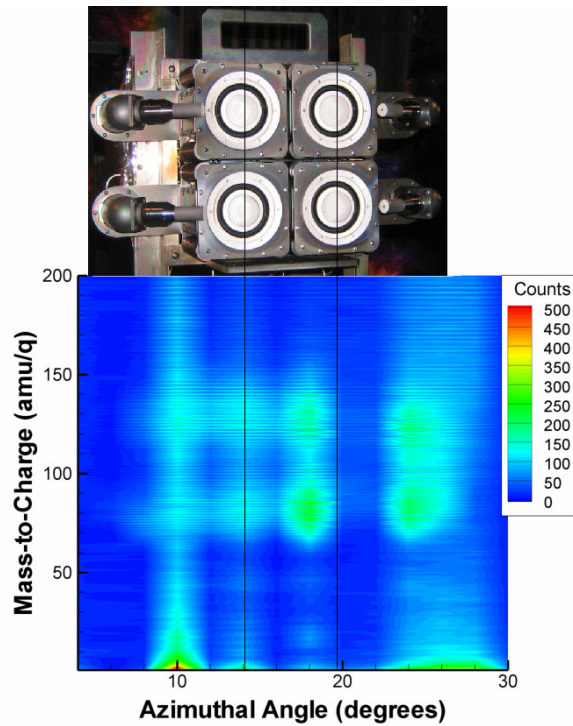


Figure 6-20: Mass-to-charge as a function of azimuthal angle for the cluster at a 20° plume angle. The cluster is pictured at a 20° for azimuthal-angle reference.

The approximate location of the thrusters with respect to the angular measurements is displayed in the above plot. Due to the decreased overall counts for the 20°, there is significant noise, however the first two charge states are measured from four areas of the thruster, the inside channels and near-cathode regions on the left and right halves of the cluster. Very slight measurements of multi-charged ions are measured from the regions near the center of the cluster, however significant noise on the outskirts prevent measurement of these ions beyond these angles.

Single Thruster Operation: 0° and 10° Plume Angles

For the single bottom-left thruster, measurements of mass-to-charge versus the azimuthal angle are displayed in Figure 6-21.

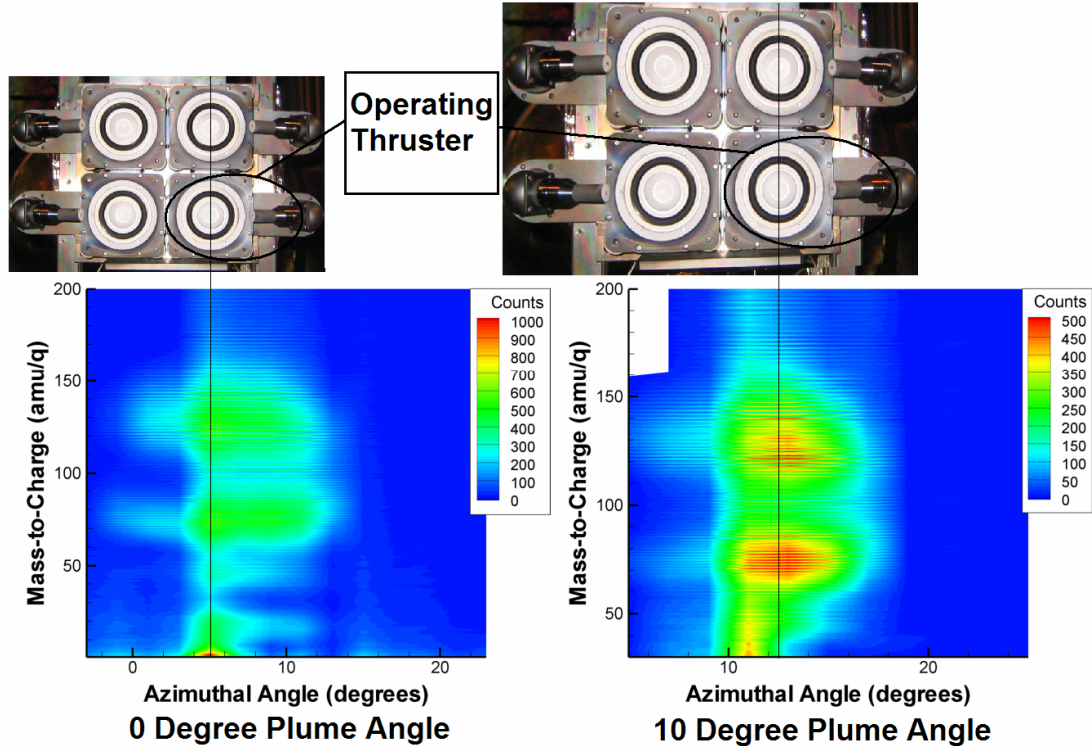


Figure 6-21: Mass-to-charge as a function of azimuthal angle for the bottom-left thruster at 0° (left) and 10° (right) plume angles. Note: Colors are respect to individual thruster condition.

The above plots indicate the first two charge states are detected for the both plume angles, however only a slight discrimination can be made for Xe^{3+} in the 0° plume angle condition. The first two charge states are detected from in front of the discharge channel and near the cathode, whereas Xe^{3+} is detected from closer to the discharge channel for the 0° plume-angle case.

6.4.3.3 Elevation Angle and Mass-To-Charge Measurements

Measurements on the cluster at the 0° plume angle yielded the detection of ions at exceedingly high guiding plate voltages up to 90 V. Since this voltage corresponds with abnormally high elevation angles, Debye shielding was concluded to have interfered with profiles in the vertical direction. The use of a grounded grid to decrease the ion density

within TOPAZ resulted in a lack of signal for time-of-flight measurements. Since the plots did not show features which could be correlated with physical properties of the thruster, this prevented quantitative measurements of the elevation angle; however, general qualitative conclusions can be drawn. Figure 6-22 displays a plot of the elevation angle versus the mass-to-charge ratio for the cluster operation at the 10° plume angle.

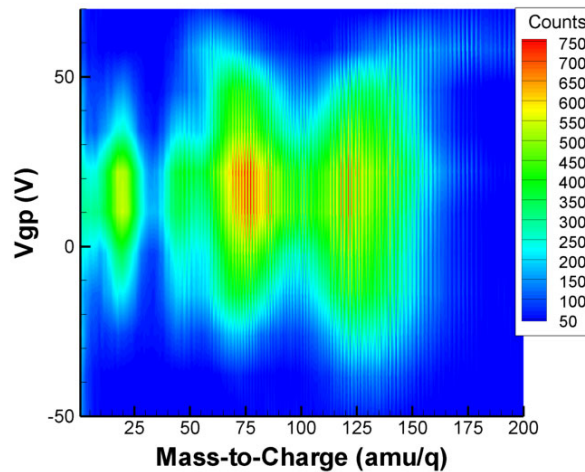


Figure 6-22: Guiding plate voltage as a function of mass-to-charge ratio for the cluster operation at a 10° plume angle.

The above plot is indicative of the guiding-plate relationship with the mass-to-charge for either the cluster or single thruster operation at the various plume angles. The first two charge states of xenon display a wider range of guiding plate voltages while Xe^{3+} and Xe^{4+} . This indicates that multi-charged xenon is limited to the vertical positions for which they emanate from the thruster, while the singly- and doubly-charged xenon are generated from a wider range of vertical positions on the thruster. This same relationship was measured in the horizontal positions as well.

6.4.3.4 Estimation of Ionization Fraction

By summing up the effective mass ranges which correspond to each charge-state an estimation of the ionization fraction can be determined as a function of the azimuthal angle. The fraction is calculated for the 0° plume angle for the cluster operation in Figure 6-23 for the first three charge-states of xenon. The error bars are assumed to be 10%, 25%, and 50% for the Xe^+ , Xe^{2+} , and Xe^{3+} charge states respectively.

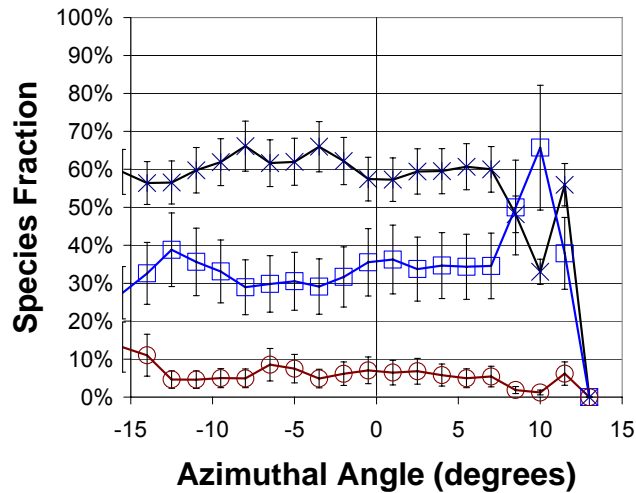


Figure 6-23: Species fraction as a function of azimuthal angle for the cluster operation at a 0° plume angle.

The above plot indicates the plume is composed of approximately 60% Xe^+ , 30-35% Xe^{2+} , and 5-10% Xe^{3+} . It is also evident that the charge fractions do not vary significantly as a function of the azimuthal angle for the cluster operation at a 0° plume angle. However an anomalous spike is measured at 10° , and is most likely due to experimental error.

A plot of the species fraction for the cluster operation at a 10° plume angle shows some slight geometry dependence on the detection of the charge states in Figure 6-24.

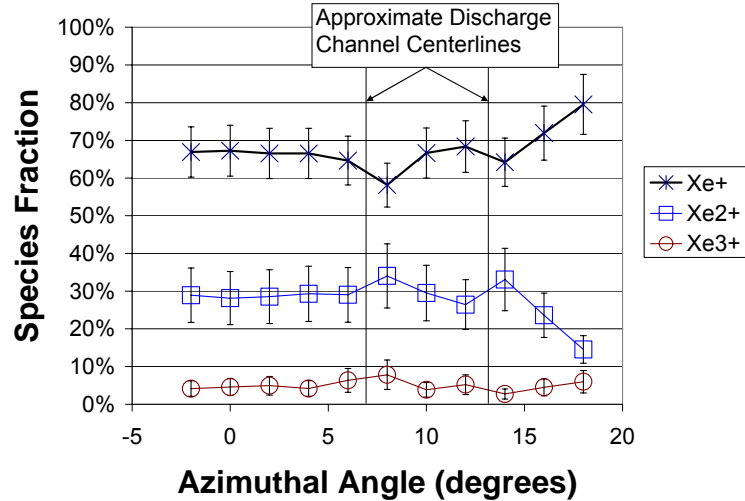


Figure 6-24: Species fraction as a function of azimuthal angle for the cluster operation at a 10° plume angle.

Along the discharge channel centerlines, there is a slight dip in the Xe^+ and an increase in Xe^{2+} . Over the left discharge channels, this coincides with the maximum Xe^{3+} fraction. As the previous measurements indicate, the production of multiply-charged ions occurs over the discharge-channel regions, and the fraction of single-charged xenon ions is lower. A possible reason is that the electrons are slightly more energetic near the discharge channel, and are therefore more likely to knock more electrons off propellant particles and create the multiple-charged ions in this region.

6.4.3.5 Axial and Radial Velocity Distribution

The following equations describe how the axial and radial velocity distributions for each species can be calculated through use of the azimuthal angle β , energy-to-charge E/q , and mass-to-charge m/q :

$$v_{radial} = -\sin(\beta) \sqrt{\frac{2(E/q)}{(m/q)}} \quad \text{Eqn. 6-13}$$

$$v_{axial} = \cos(\beta) \sqrt{\frac{2(E/q)}{(m/q)}} \quad \text{Eqn. 6-14}$$

The above calculations assume a rectilinear coordinate system. Ions traveling from the left side of the thruster with a negative azimuthal angular-trajectory have a positive radial velocity, whereas ions traveling from the right side of the thruster have a negative radial velocity. An ions moving away from the thruster has a positive axial velocity. The error bars in the first-, second-, and third-charge states are assumed to be 10%, 25%, and 50%, respectively. A plot of the radial velocity is shown in Figure 6-25.

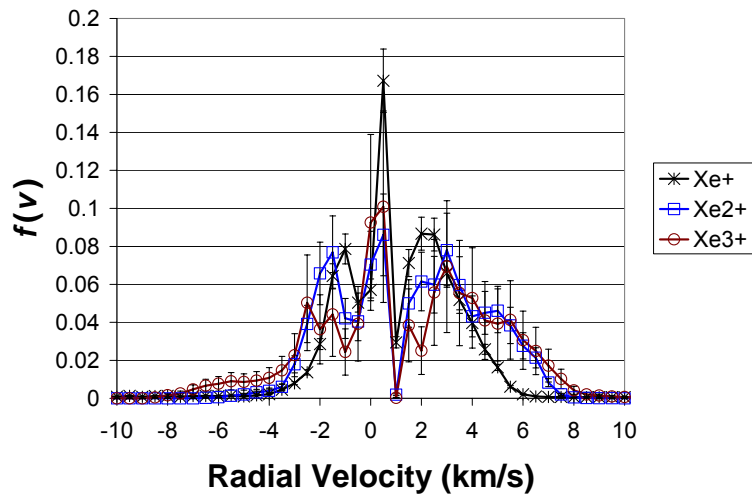


Figure 6-25: Radial velocity distribution of Xe^+ , Xe^{2+} , and Xe^{3+} from the 0° plume angle for the cluster operating condition.

The above plot is approximately symmetric (as expected) about 0 km/s. This is also the most likely radial velocity – ions moving perpendicular to the plane of the discharge channels. However two spikes are measured on each side. It is likely these correspond with measurements of ions from the left and right regions of the discharge channel near the cathodes. Since the Xe^{2+} and Xe^{3+} ions were more likely to emanate from the discharge channel centerlines (which is 2.3° off from the cluster centerline),

they are less likely to be detected from the thruster centerline. The second- and third-charge xenon ions have similar profiles, although (as shown below) Xe^{3+} , has a much higher axial velocity. This indicates the trajectory of Xe^{3+} is at slighter azimuthal angles than the doubly-charged ions, allowing for both species to have similar radial velocity distributions.

Figure 6-26 displays a plot of the axial velocity for each species.

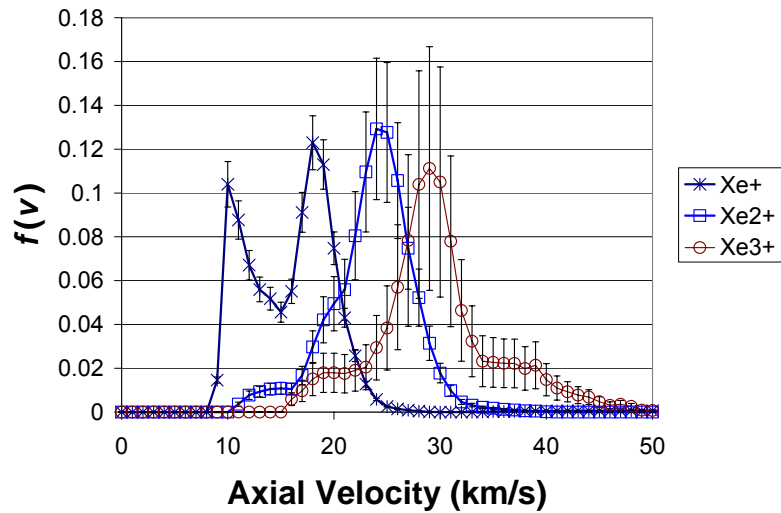


Figure 6-26: Axial velocity distribution of Xe^+ , Xe^{2+} , and Xe^{3+} from the 0° plume angle for the cluster operating condition.

Peaks with successively higher axial velocities were measured for the first, second, and third charge-states of xenon. However, it is interesting to note the double peak that is present for Xe^+ . The likely reason for this is the existence of a strong focusing effect for Xe^+ emanating from the interior regions (near the cluster centerline) of the thruster. These ions have little radial velocity, and are accelerated in a mostly axial direction. This accounts for the higher peak for Xe^+ . Singly-charged xenon ions that are detected from near the cathode, however, have lower energies as shown in the previous chapter. Since the angle of these ions also induces “cosine-losses” in the axial direction,

they have significantly lower axial velocities. The single-charged xenon ions emanating from regions near the cathodes from either side of the cluster most likely contributes to the lower peak in the velocity distribution. The Xe^{2+} and Xe^{3+} ions, however, are generated from near the discharge channel regions, and not as much from the outskirts of the cluster. Therefore, the axial velocity is not decreased by “cosine-losses” and near-cathode effects.

6.4.4 Conclusions on the Time-Of-Flight Measurements of the BHT-600 Cluster

Several interesting phenomena were identified with TOPAZ. The first three, and possibly the fourth, charge-states of xenon were measured. By varying the energy-to-charge measurements, an energy-to-charge (and hence energy through multiplication of the charge) distribution was produced for each charge-state. The second charge-state of xenon was found to have an energy distribution slightly above the discharge voltage, while the first, third, and fourth charge-states had peak energies slightly below the 300 V discharge voltage. The reason for this discrepancy is attributed to charge-exchange collisions with multi-charged xenon ions. This results in ions with fractional energies of the acceleration voltage. Another possibility is ionization (for example from a Xe^+ to a Xe^{2+}) outside of the primary acceleration region. This would result in the creation of doubly-charged ions with energies above the discharge voltage, but below twice this energy.

By profiling the azimuthal angle of ions with the mass-to-charge measurements, correlations between the likely emanation points of different species of ions was determined. The third and fourth charge-states were found to have trajectories originating from directly in front of the discharge channel, while the single- and double-charged

xenon ions had a wider horizontal distribution. Variation of the guiding plate potential indicates that a wider vertical distribution for the single- and double-charged xenon is evident as well. Measurements of the species of ions at 20° reveal a large drop in the presence of multi-charge ions for this plume angle. This reveals that although the triple- and possible quadruple-charged xenon are more likely to be measured at angles slightly off the cluster centerline, they are mostly confined to plume angles within 20° .

A calculation of the ionization fraction revealed it is mostly constant as a function of azimuthal angle for the 0° plume angle with the cluster operation, however, for the 10° plume angle, there is a slight dip in single-charged xenon and increase in doubly-charged xenon near the discharge channels.

The axial and radial velocity distribution functions were calculated for the thruster operation at a 0° plume angle. This revealed a triple-peak structure for the radial velocity distribution of each of the species. A double peak structure for the axial distribution of the single-charged xenon was measured, whereas the double and triple charge-states display single-peaked distributions.

6.5 Conclusions on the Operation of TOPAZ

Several measurement capabilities were tested with TOPAZ. Time-of-flight measurements with the instrument revealed that charge-state discrimination of the propellant ions is possible. Although TOPAZ has a fairly low mass resolution (13%) due to the instrument's geometry, the heavy mass of the xenon particles allows for easy identification of the different charge states. Properties, such as the energy and azimuthal

detection angle are easily measured, and maintain their accuracy as with the previous energy measurements on the BHT-600 cluster.

Measurements utilizing the guiding plate potential proved much more difficult. Unfortunately, significant Debye shielding prevented quantitative analysis from the data. Since the time-of-flight measurements significantly decrease the current collected by the detector, a higher signal-to-noise ratio persists than with energy measurements. This problem could be possibly alleviated with an analyzer with a small analyzer constant. A larger gap size would increase the ions detected. This in combination with a grounded grid around TOPAZ could allow for accurate elevation angle profiling, without the deleterious effects of Debye shielding.

Measurements of Xe^{4+} were inconclusive, due to the low mass resolution of the instrument. Since an $\mathbf{E} \times \mathbf{B}$ instrument can determine the population of each charge-state, this would prove a simple method of determining an overall ionization fraction measurement. However the accurate energy and azimuthal angle measurements which are capable with TOPAZ indicate the instrument functions particularly well when specific regions of the thruster are of interest, and angular correlations with the mass and energy distribution are desired.

CHAPTER 7: CONCLUSIONS

Throughout this dissertation, a top hat analyzer has been designed, characterized, and utilized for Hall thruster far-field plume diagnostics. As the trend for the development high-power/high- I_{sp} electric propulsion systems (Hall thrusters in particular) continue, the need for the ground-based characterization of these devices will grow as well. The motivation for the development of a top hat analyzer to address this need was its suitability for high-energy plasma diagnostics. However adaptations for the instrument's use in a high-density environment required some modification to the instrument's design. The capabilities of the analyzer, however, allow for previously unknown correlations in the plasma properties of the Hall thruster plume to be measured *in-situ*. Use of a top hat analyzer is therefore *recommended* for plume diagnostics if the energy-angle or mass-angle distributions of beam ions are desired.

In this chapter, the major findings on the applicability of the analyzer towards plume diagnostics are discussed. The “lessons learned” throughout the design and testing of the instrument are presented, and suggestions for future research with the analyzer as well as ideas for new designs are presented.

7.1 Design of the Analyzer for Plume Diagnostics

The top hat analyzer, as discussed in Chapter 2, has a relatively simple design procedure. Possibly the most important choice for the analyzer design was the analyzer constant. Several properties of the analyzer were found to directly correlate with this ratio of the channel radius to the channel width. Therefore, for the design of any top hat analyzer, extensive thought should be put into the choice of the analyzer constant for the instrument.

7.1.1 Choice of the Analyzer Constant

For TOPAZ, the very high analyzer constant of $K=100$ proved useful as well as detrimental to the instrument's operation. The very high energy-resolution of 2.0% (2.8% through simulations) allowed for accurate measurements of energy distributions of the plasma. However, features of the energy distribution of ions in the Hall thruster plume are rarely discerned at this detail. For example, the measurements of multiple peaks in energy-per-charge profiles of the SPT-100 Hall thruster through the Molecular Beam Mass Spectrometer (MBMS), an energy analyzer utilized for plume diagnostics by King, required resolving peaks at $4/3 \times V_{dis}$ and $3/2 \times V_{dis}$, where V_{dis} is the beam voltage of the ions (~ 300 V).⁹⁸ The difference in these two peaks is 16.7%. For an accurate portrayal of the two distributions, an energy resolution on the order of a quarter of this would suffice. This correlates with an energy resolution of 4.2%. A top hat instrument with an analyzer constant of 50 would provide this resolution. Therefore, unless future measurements in the plume yield significant detail at energy ranges smaller than this resolution, an analyzer constant above 50 is unnecessary.

The high analyzer constant of TOPAZ resulted in operation issues which might have been avoided with a larger gap distance. For example, as discussed in Chapter 5, the BHT-600 Cluster imparted a large thermal load on the instrument. The small gap distance which TOPAZ utilized magnified the effects of plate shifting at the sub-millimeter level. For smaller analyzer constants, the shifting of the deflection plate would not have been as detrimental, and possibly negligible for larger gap distances.

As Equation 3-1 states the Debye length is defined by the following equation:

$$\lambda_D = 7430 \left(\frac{kT_e}{n} \right)^{1/2} \quad \text{Eqn. 7-1}$$

This is a measure of the effective shielding due to charged particles, and at a distance of approximately $10\lambda_D$ away from a surface, the plasma has electrically shielded an object from its surroundings. The concern for the high-density environment of Hall thruster plume was the driving factor for designing TOPAZ with a high analyzer constant. However, this problem can be attacked from a different angle. If the plasma density is lowered significantly, the required shielding distances can be greatly increased. This can be done with collimated enclosures and open-area grounded mesh which does not significantly alter the properties of beam ions before they are detected. It is also important to note that artificial decreasing of the plasma density within the analyzer is fairly easy, whereas changing the analyzer constant of a top hat analyzer requires re-machining of the deflection plate.

Another reason for the use of a smaller analyzer constant is its relationship with the geometric factor. This is a measure of the overall sensitivity of the instrument, and it is proportional to $K^{-3.5}$. The small geometric factor of $3 \times 10^{-4} \text{ cm}^2 \text{ sr eV/eV}$ that resulted from the high analyzer constant prevented energy distribution measurements at plume

angles beyond 60° and mass distribution measurements beyond 20°. Utilizing an analyzer constant of 50, would increase the geometric factor by more than an order of magnitude. This would likely increase the range of plume angles for which mass distribution measurements could be made.

It is important to note that although space plasmas are much lower density as compared with Hall thruster plume (see Figure 1-7 for comparison of plasmas), the density of ambient, low-energy (i.e., unthermalized) ions is also lower. Spurious ions which interact with the detector (such as a channel electron multiplier) generate noise about the signal. Therefore, the ion current to be detected should be significantly higher than ambient ions around the detector for accurate plasma diagnostics, and the detector should be isolated as much as possible from ambient plasma particles.

7.1.2 Choice of Materials

Another design consideration is the choice of materials for the construction of the instrument. Although Delrin® has low water absorption and is easily machinable, the low melting point and large thermal expansion of this material proved detrimental to the operation of TOPAZ. For energy analyzers utilized for plume diagnostics in vacuum chambers, contamination due to water is not an issue. However, the high temperature environment requires the use of ceramics such as Macor®, Glass Mica, or Boron Nitride for parts that are not electrically conductive. Plastics, like Delrin®, are not suggested for use in Hall thruster plume diagnostics.

7.1.3 Use of the Azimuthal Angle

For all the measurements conducted with TOPAZ, only a single azimuthal position underneath the instrument was utilized, and the entire instrument was rotated to simulated different azimuthal angles. This indicates the full axisymmetric geometry of the instrument is not necessary for its operation. As opposed to space instrumentation, moving parts and rotational stages are routinely used for plume diagnostics. The following is a design for an electrostatic analyzer that would function similarly to TOPAZ.

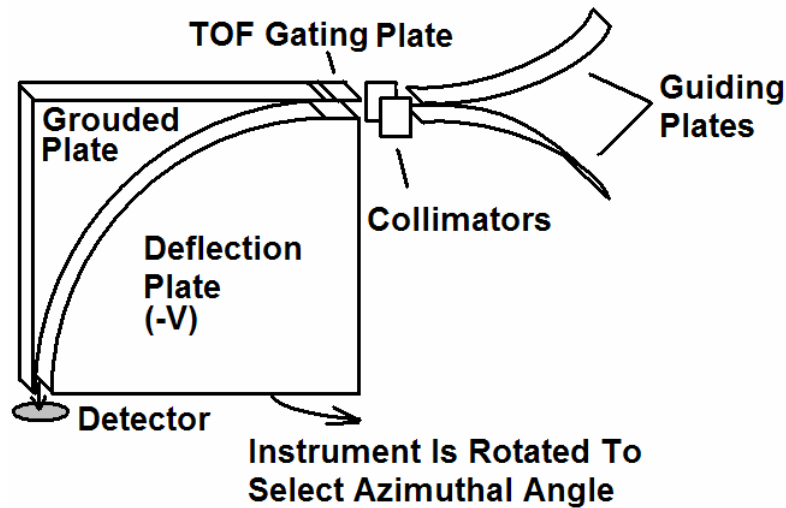


Figure 7-1: Major components of an electric sector with similar capabilities as TOPAZ.

The instrument described in Figure 7-1 would not require machining of large, axisymmetric shells for its operation. Also, the use of arbitrarily small gating plates (however, higher voltages would be required) would allow for accurate time-of-flight measurements for mass spectrometry. The deflection plate and guiding plate would be shaped similarly to the top hat analyzer cross section, and the instrument would be rotated about the central axis for azimuthal angle measurements.

However, if a simultaneous measurement of all azimuthal angles is desired for increasing the speed of measurements, then a top hat analyzer with an array of detectors situated at different azimuthal locations underneath the instrument would be required.

7.2 Measurement Capabilities

TOPAZ provided some measurement capabilities which are absent in most other plume diagnostics tools. These capabilities and their applicability towards plume diagnostics are discussed.

7.2.1 Energy-Angle Measurements

The best measurement capability which top hat analyzers have to offer (and hence TOPAZ) is the ability to profile energy-per-charge as a function of angle. Since the instrument can select a specific horizontal and vertical angle (if Debye shielding is not an issue) and energy, the energy distribution can be compared with different parts of the thruster being investigated. By measuring a specific energy and varying the azimuthal and elevation angle settings, an “image” of ions at a particular energy-to-charge ratio can be created. These two measurement possibilities are what make top hat analyzers a valuable asset for advanced plume diagnostics which conventional instruments lack.

7.2.2 Energy-Mass Measurements

Since the top hat analyzer can function with a mass-to-charge spectrometer, properties of each species of ion can be measured. This allows for individual energy-to-charge profiles of each charge-state (and hence just energy) to be measured. As measured with the BHT-600 Cluster, the second charge-state of xenon was shown to have slightly higher energies than the other charge states. Since a regular energy analyzer does not

discriminate charge, this distinction would have not been possible without the mass spectrometer.

The top hat instrument's low mass resolution was due to the geometry of the instrument. The effective gating distance varies with position over the aperture. This results in a broadening of the peaks, since ions with different TOF distances and different velocities can arrive at the detector at the same time. However, since Hall thrusters utilize propellants with heavy atomic masses, discrimination of the mass-per-charge allowed for individual charge-states to be measured.

An instrument with the energy-to-charge and mass-to-charge measurement capability could be created through a retarding potential analyzer (RPA, see Figure 2-1). By extending the distance between the collection length, and the ion retarding grid, a drift region could be utilized to measure the flight velocity of detected ions. This measurement in combination of the derivative of the collected current with respect to ion retarding voltage would provide measurements of the energy-per-charge as well as the mass-to-charge ratio.

7.2.3 Mass-Angle Measurements

Similar to the energy-angle measurement capability, the top hat analyzer allows for mass-to-charge profiles to be determined as a function of horizontal angle. This allows for the identification of what region ions of a specific charge are emanating from. As discussed in Chapter 6, multiply-charged ions were determined to propagate from the interior regions of the cluster for plume angles of 0° and 10° , while mostly single- and double- charged ions were measured around the thruster and at plume angles of 20° .

7.2.4 Ion Species Fractions and Velocity Distributions

The measurements of mass- and energy-to charge ratios along with angular measurements, allows for a calculation of each species fraction as a function of angle, as well as the axial and radial velocity distributions. These measurements give insight into how the cluster orientation of the thrusters affects the far-field plume properties.

7.3 Suggestions for Future Work

The capabilities of the top hat analyzer were showcased through measurements on the BHT-600 cluster with TOPAZ. The following are some ideas for the utilization of TOPAZ as a viable tool for advanced plume diagnostics:

- Since the axial and radial velocities were directly measured with TOPAZ, a **comparison with laser-induced fluorescence (LIF)** will help corroborate the measurements of TOPAZ. Although the energy profiles and time-of-flight measurements of TOPAZ have been compared with previous measurements on similarly powered thrusters, measurements of the velocity distribution function for each charge state in a Hall thruster cluster would support the results of TOPAZ such as the triple-peak structure measured with the singly-charge propellant ions
- **Mid-field plume diagnostics at distances up to 0.50 m** from the thruster could be conducted for possibly a wider range of plume angles. Since the plasma current would be significantly higher, TOF profiles for a wider range of plume angles could be measured for the cluster and single thruster operation. However, this

presents the caveat of a higher thermal load on the instrument. The materials now utilized in TOPAZ have a high thermal capability after the Delrin® base plate was replaced.

- **Creation of a better enclosure which decreases the plasma density, but still allows for a significant detection of ions** might allow the guiding plate to function properly in a high-density environment. Another solution to this dilemma is the re-machining of the deflection plate. A decrease in 2 mm of the radius would result in an analyzer constant of 33 for TOPAZ and yield a respectable energy resolution of 7.5%. However this would increase the overall acceptance (geometric factor) by almost 50 times. Energy measurements and time-of-flight measurements at angles beyond those currently measured with TOPAZ would be possible with the increased current and sampling rate at the detector.
- **Creation of the electric sector described in Figure 7-1 or an RPA with a TOF capability.** Either of these instruments would allow for plume-diagnostic capability similar to TOPAZ, however the simplicity of the above designs allows for optimization of the design (through modification of the devices after testing) and possibly miniaturization of the instruments. The electric sector, in particular would allow for a better mass resolution in conjunction with the angular measurement capability of TOPAZ.

REFERENCES

1. Newton, I., *The Principia: Mathematical Principles of Natural Philosophy*, 1st Ed., Trans. B. Cohen and A. Whitman, University of California Press, Berkeley, CA, 1999.
2. Jahn, R. G., *Physics of Electric Propulsion*, McGraw-Hill Book Company, New York, NY, 1968.
3. Sutton, G. P., Biblarz, O., *Rocket Propulsion Elements*, 7th Ed., John Wiley & Sons, Inc., New York, NY, 2001.
4. Stevens, R., Ross, I. M., "Preliminary Design of Earth–Mars Cyclers Using Solar Sails," *Journal of Spacecraft and Rockets*, Vol. 42, No. 1, pp. 132-137, January-February 2005.
5. Anderson, J. L., Rather, J. D. G., Powell, J. R., "Beamed Energy for Fast Space Transport," AIAA-1996-2785, 32nd AIAA/ASME/SAE/ASEE Joint Propulsion Conference and Exhibit, Buena Vista, FL, July 1-3, 1996.
6. Sanmartín, J. R., Lorenzini, E. C., "Exploration of Outer Planets Using Tethers for Power and Propulsion," *Journal of Propulsion and Power*, Vol. 21, No. 3, pp. 573-576, May-June 2005.
7. Wertz, J. R., Larson, W. J., *Space Mission Analysis and Design*, 3rd Ed., Microcosm Press, Torrance, CA, 1999.
8. Choueiri, E. Y., "A Critical History of Electric Propulsion: The First Fifty Years (1906-1956)," AIAA-2004-3334, 40th AIAA/ASME/SAE/ASEE Joint Propulsion Conference and Exhibit, Fort Lauderdale, FL, July 11-14, 2004.
9. Frisbee, R. H., "Advanced Space Propulsion for the 21st Century," *Journal of Propulsion and Power*, Vol. 19, No. 6, pp. 1129-1154, November-December 2003.
10. Langmuir, D. B., "Low-Thrust Flight: Constant Exhaust Velocity in Field-Free Space," *Space Technology*, H. Seifert, ed., John Wiley & Sons, New York, 1959.
11. Patel, P., Scheeres, D., Gallimore, A., "Maximizing Payload Mass Fractions of Spacecraft for Interplanetary Electric Propulsion Missions," *Journal of Spacecraft and Rockets*, (accepted for publication).

12. Greco, R. V., Charhut, E. E., "Resistojet Systems Manned Spacecraft Applications," AIAA 7th Electric Propulsion Conference, Williamsburg, VA, March 3-5, 1969.
13. Myers, R. M., "Overview of Major U.S. Industrial Electric Propulsion Programs," AIAA-2004-3331, 40th AIAA/ASME/SAE/ASEE Joint Propulsion Conference and Exhibit, Fort Lauderdale, FL, July 11-14, 2004.
14. Sutton, G. W., Sherman, A., *Engineering Magnetohydrodynamics*, McGraw-Hill Book Company, New York, NY, 1965.
15. Toki, K., Shimizu, Y., Kuriki, K., Kuninaka, H., "An MPD Arcjet Thruster System for Electric Propulsion Experiment (EPEX) in Space," AIAA-1994-2989, 30th AIAA/ASME/SAE/ASEE Joint Propulsion Conference, Indianapolis, IN, June 27-29, 1994.
16. Burton, R. L., Turchi, P. J., "Pulsed Plasma Thruster," *Journal of Propulsion and Power*, Vol. 14, No. 5, pp. 716-735, September-October 1998.
17. Hoskins, W. A., Rayburn, C., "Pulsed Plasma Thruster Electromagnetic Compatibility: History, Theory, and the Flight Validation on EO-1," AIAA-2003-5016, 39th AIAA/ASME/SAE/ASEE Joint Propulsion Conference and Exhibit, Huntsville, AL, July 20-23, 2003.
18. Andrenucci, M., Marcuccio, S., Genovese, A., "The Use of FEEP Systems for Micronewton Thrust Level Missions," AIAA-1993-2390, AIAA/SAE/ASME/ASEE 29th Joint Propulsion Conference and Exhibit, Monterey, CA,
19. Genovese, A., Tajmar, M., Buldrini, N., Steiger, W., "Extended Endurance Test of the Indium FEEP Microthruster," AIAA-2002-3688, 38th AIAA/ASME/SAE/ASEE Joint Propulsion Conference and Exhibit, Indianapolis, IN, July 7-10, 2002.
20. Kaufman, H. R., "The Electron-Bombardment Ion Rocket," Third Symposium on Advanced Propulsion Concepts, Cincinnati, OH, October 2-4, 1962.
21. Patterson, M. J., "Low-Isp Derated Ion Thruster Operation," AIAA-92-3203, AIAA/SAE/ASME/ASEE 28th Joint Propulsion Conference and Exhibit, Nashville, TN, July 6-8, 1992.
22. Foster, J. E., Haag, T., Kamhawi, H., Patterson, M., et al., "The High Power Electric Propulsion (HiPEP) Ion Thruster," AIAA-2004-3812, 40th AIAA/ASME/SAE/ASEE Joint Propulsion Conference and Exhibit, Fort Lauderdale, FL, July 11-14, 2004.

23. Benson, S., Patterson, M., "NASA's Evolutionary Xenon Thruster (NEXT) Phase 2 Development Status," AIAA-2005-4070, 41st AIAA/ASME/SAE/ASEE Joint Propulsion Conference and Exhibit, Tucson, AZ, July 10-13, 2006.
24. Pote, B., Hruby, V., Tedrake, R., "Performance of a Multi-Kilowatt Non-Circular Discharge Hall Thruster," AIAA-2000-3249, 36th AIAA/ASME/SAE/ASEE Joint Propulsion Conference & Exhibit, Huntsville, AL, July 16-19, 2000.
25. Hargus, W. A., Cappelli, M. A., "Development of a Linear Hall Thruster," AIAA-1998-3336, 34th AIAA/ASME/SAE/ASEE Joint Propulsion Conference and Exhibit, Cleveland, OH, July 13-15, 1998.
26. Smirnov, A., Raitses, Y., Fisch, N., "Plasma Measurements of a 100 W Cylindrical Hall Thruster," AIAA-2003-5000, 39th AIAA/ASME/SAE/ASEE Joint Propulsion Conference and Exhibit, Huntsville, AL, July 20-23, 2003.
27. Yashnov, Y. M., Koester, J. K., McVey, J. B., Britt, E. J., "Fundamental Design of Highly Effective Hall Thrusters," IEPC-99-099, 26th International Electric Propulsion Conference, Kitakyushu, Japan, October 1999.
28. Absalamov, S. K., Andreev, V. B., Colbert, T., Day, M., et al., "Measurement of plasma parameters in the stationary plasma thruster (SPT-100) plume and its effect on spacecraft components," AIAA-1992-3156, 28th AIAA/SAE/ASME/ASEE Joint Propulsion Conference and Exhibit, Nashville, TN, July 6-8, 1992.
29. Hofer, R. R., "Development and Characterization of High-Efficiency, High-Specific Impulse Xenon Hall Thrusters," Ph.D. Thesis, Dept. of Aerospace Engineering, University of Michigan, Ann Arbor, 2005.
30. Hofer, R., "Development and Characterization of High-Efficiency, High-Specific Impulse Xenon Hall Thrusters," Ph.D. Thesis, Dept. of Aerospace Engineering, University of Michigan, Ann Arbor, 2004.
31. Peterson, P. Y., Jacobson, D. T., Manzella, D. H., John, J. W., "The Performance and Wear Characterization of a High-Power High-Isp NASA Hall Thruster," AIAA-2005-4243, 41st AIAA/ASME/SAE/ASEE Joint Propulsion Conference & Exhibit, Tucson, Arizona, July 10-13, 2005.
32. Clauss, C., Day, M., Kim, V., Kondakov, Y., "Preliminary Study of Possibility to Ensure Large Enough Lifetime of SPT Operating Under Increased Powers," AIAA-97-2789, 33rd AIAA/SAE/ASME/ASEE Joint Propulsion Conference and Exhibit, Seattle, WA, July 6-9, 1997.
33. Yim, J., Keidar, M., Boyd, I. D., "An Evaluation of Sources of Erosion in Hall Thrusters," AIAA-2005-3530, 41st AIAA/ASME/SAE/ASEE Joint Propulsion Conference & Exhibit, Tucson, AZ, July 10-13, 2005.

34. Marcuccio, S., Giannelli, S., Andrenucci, M., "Attitude and Orbit Control of Small Satellites and Constellations with FEED Thrusters," IEPC-97-188, 25th Electric Propulsion Conference, Cleveland, OH, 1997.
35. Reichbach, J. G., Sedwick, R. J., Martinize-Sanchez, M., "Micropropulsion System Selection for Precision Formation Flying Satellites," 37th AIAA/ASME/SAE/ASEE Joint Propulsion Conference & Exhibit, Salt Lake City, Utah, July 8-11, 2001.
36. Oleson, S., Elliott, F., "The Electric Propulsion Segment of Prometheus 1," AIAA-2005-3888, 41st AIAA/ASME/SAE/ASEE Joint Propulsion Conference and Exhibit, Tucson, AZ, July 10-13, 2005.
37. Vhrenkamp, R. P., "Measurement of Double Charged Ions in the beam of a 30-cm Mercury Bombardment Thruster," AIAA-73-1057, AIAA 10th Electric Propulsion Conference, AIAA, October 31-November 2, 1973.
38. King, L. B., Gallimore, A. D., "Ion-Energy Diagnostics in an SPT-100 Plume from Thrust Axis to Backflow," *Journal of Propulsion and Power*, Vol. 20, No. 2, pp. 228-242, March-April 2004.
39. Randolph, T., Pencil, E., Manzella, D., "Far-Field Plume Contamination and Sputtering of the Stationary Plasma Thruster," AIAA-94-2855, 30th AIAA/ASME/SAE/ASEE Joint Propulsion Conference, Indianapolis, IN, July 27-29, 1994.
40. Kaufman, H. R., "Technology of Closed-Drift Thrusters," AIAA-83-1398, AIAA/SAE/ASME 19th Joint Propulsion Conference, Seattle, WA, June 27-29, 1983.
41. Kaufman, H. R., Robinson, R. S., Day, M. S., Haag, T. W., "End-Hall Thrusters," AIAA-90-2595, AIAA/DGLR/JSASS, Orlando, FL, July 18-20, 1990.
42. Burgrova, A. I., Yermakov, Y. A., Morozov, A. I., Yakunin, S. A., "A New Stage of Stationary Plasma Engine (SPE) Development," Anniversary Specialist Conference on Nuclear Power Engineering in Space, Obninsk, Russia, May 15-19, 1990.
43. Gulczinski, F. S., Spores, R. A., "Analysis of Hall-effect Thrusters and Ion Engines for Orbit Transfer Missions," AIAA-96-2973, 32nd AIAA/ASME/SAE/ASEE Joint Propulsion Conference, Lake Buena Vista, FL, July 1-3, 1996.
44. Spores, R. A., Spanjers, G.G., Birkan, M., Lawrence, T.J., "Overview of the USAF Electric Propulsion Program," AIAA-2001-3225, 37th AIAA/ASME/SAE/ASEE Joint Propulsion Conference and Exhibit, Salt Lake City, UT, July 8-11, 2001.

45. Dunning, J., Sankovic, J., "NASA's Electric Propulsion Program," AIAA-2000-3145, 36th AIAA/ASME/SAE/ASEE Joint Propulsion Conference & Exhibit, Huntsville, AL, July 17-19, 2000.
46. Manzella, D., Jankovsky, R., Hofer, R., "Laboratory Model 50 kW Hall Thruster," AIAA-2002-3676, 38th AIAA/ASME/SAE/ASEE Joint Propulsion Conference & Exhibit, Indianapolis, IN, July 7-10, 2002.
47. Jacobson, D. T., Jankovsky, R. S., Rawlin, V. K., Manzella, D. H., "High Voltage TAL Performance," AIAA-2001-3777, 37th AIAA/ASME/SAE/ASEE Joint Propulsion Conference & Exhibit, Salt Lake City, UT, July 8-11, 2001.
48. Gallimore, A. D., "Near- and Far-Field Characterization of Stationary Plasma Thruster Plumes," *Journal of Spacecraft and Rockets*, Vol. 38, No. 3, pp. 441-453, May-June 2001.
49. Bame, S. J., McComas, D. J., Young, D. T., Belian, R. D., "Diagnostics of Space Plasmas," *Review of Scientific Instruments*, Vol. 57, No. 8, pp. 1711-1716, August 1986.
50. Vilppola, J. H., Tanskanen, P. J., Huomo, H., Barraclough, B. L., "Simulations of the Response Function of a Plasma Ion Beam Spectrometer for the Cassini Mission to Saturn," *Review of Scientific Instruments*, Vol. 67, No. 4, pp. 1494-1501, April 1996.
51. Rayman, M. D., Lehman, D. H., "Deep Space One: NASA's First Deep-Space Technology Validation Mission," *Acta Astronautica*, Vol. 41, No. 4, pp. 289-299, 1997.
52. Nordholt, J. E., Young, D. T., Funsten, H. O., "Plasma Experiment for Planetary Exploration (PEPE) on DS1," 10.1109/AERO.2000.879327, Aerospace Conference Proceedings, Big Sky, MT,
53. Walker, M. L. R., Victor, A. L., Hofer, R. R., Gallimore, A. D., "Effect of Backpressure on Ion Current Density Measurements in Hall Thruster Plumes," *Journal of Propulsion and Power*, Vol. 21, No. 3, pp. 408-415, May-June 2005.
54. Hutchinson, I. H., *Principles of Plasma Diagnostics*, Press Syndicate of the University of Cambridge, New York, NY, 1987.
55. King, L. B., and Gallimore, A. D., "A Gridded Retarding Pressure Sensor for Ion and Neutral Particle Analysis In Flowing Plasmas," AIAA-96-2983, 32nd AIAA/ASME/SAE/ASEE Joint Propulsion Conference and Exhibit, Lake Buena Vista, FL, July 1-3, 1996.
56. Walker, M. L. R., Hofer, R. R., Gallimore, A. D., "Ion Collection in Hall Thruster Plumes," *Journal of Propulsion and Power*, Vol. 22, No. 1, pp. 205-209, January-February 2006.

57. D. Staack, Y. R., N. J. Fisch, "Shielded Electrostatic Probe for Nonperturbing Plasma Measurements in Hall Thrusters," *Review of Scientific Instruments*, Vol. 75, No. 2, pp. 393-399, February 2004.
58. Myers, R. M., "Plume Characteristics of MPD thrusters - A Preliminary Examination," AIAA-89-2832, AIAA/ASME/SAE/ASEE 25th Joint Propulsion Conference, Monterey, CA, July 10-12.
59. Domonkos, M. T., Gallimore, A. D., Bilen, S., "A Hall Probe Diagnostic for Low Density Plasma Accelerators," *Review of Scientific Instruments*, Vol. 69, No. 6, pp. 2546-2549, June 1998.
60. Rovey, J., "A Multiple-Cathode, High-Power, Rectangular Ion Thruster Discharge Chamber for Increasing Thruster Lifetime," Ph.D. Thesis, Dept. of Aerospace Engineering, University of Michigan, Ann Arbor, 2006.
61. Peterson, P. Y., Gallimore, A. D., Haas, J. M., "Experimental Investigation of a Hall Thruster Internal Magnetic Field Topography," IEPC-01-030, 27th International Electric Propulsion Conference, Pasadena, CA, October 15-19.
62. Williams, G. J., Smith, T. B., Patrick, T. A., Gallimore, A. D., "Characterization of the FMT-2 Discharge Cathode Plume," IEPC-99-104, 26th International Electric Propulsion Conference, Kitakyushu, Japan, October 17-21, 1999.
63. Manzella, D. H., "Stationary Plasma Thruster Plume Emissions," IEPC-93-097, 23rd International Electric Propulsion Conference, Seattle, WA, September 13-16, 1993.
64. Williams, G. J., Smith, T. B., Gulczinski, F. S., Beal, B. E., et al., "Laser Induced Fluorescence Measurement of Ion Velocities in the Plume of a Hall Effect Thruster," AIAA-99-2424, 35th AIAA/ASME/SAE/ASEE Joint Propulsion Conference and Exhibit, Los Angeles, CA, June 20-23, 1999.
65. Ohler, S. G., Gilchrist, B. E., Gallimore, A. D., "Nonintrusive Electron Number Density Measurements in the Plume of a 1 kW Arcjet Using a Modern Microwave Interferometer," *IEEE Transactions on Plasma Science*, Vol. 23, No. 3, pp. 428-435, June 1995.
66. Fessey, J. A., Gowers, C. W., Hugenholtz, C., "Plasma Electron Density Measurements from JET 2 mm Wave Interferometer," *Journal of Physics E*, Vol. 20, pp. 169-174, February 1987.
67. Kim, S. W., "Experimental Investigations of Plasma Parameters and Species-Dependent Ion Energy Distribution in the Plasma Exhaust Plume of a Hall Thruster," Ph.D. Thesis, Dept. of Aerospace Engineering, University of Michigan, Ann Arbor, 1999.

68. King, L. B., Gallimore, A. D., "Identifying Charge-Exchange Collision Products Within the Ion-Energy Distribution of Electrostatically Accelerated Plasmas," *Physics of Plasmas*, Vol. 6, No. 7, pp. 2936-2942, July 1999.
69. March, R. E., Hughes, R. J., Todd, J. F. J., *Quadrupole Storage Mass Spectrometry*, John Wiley & Sons, Inc., New York, 1989.
70. Linnell, J. A., Gallimore, A. D., "Efficiency Analysis of a Hall Thruster Operating with Krypton and Xenon," AIAA-2005-3683, 41st AIAA/ASME/SAE/ASEE Joint Propulsion Conference and Exhibit, Tucson, AZ, July 10-13.
71. Hofer, R., Haas, J. M., Gallimore, A. D., "Development of a 45-Degree Parallel-Plate Electrostatic Energy Analyzer for Hall Thruster Plume Studies: Preliminary Data," IEPC-99-113, 26th International Electric Propulsion Conference, Kitakyushu, Japan, October 17-21, 1999.
72. Moore, J. H., Davis, C. C., Coplan, M. A., *Building Scientific Apparatus*, 3rd Ed., Perseus Books, Cambridge, MA, 2003.
73. Smeenk, R. G., Tromp, R. M., Kersten, H. H., Boerboom, A. J. H., et al., "Angle Resolved Detection of Charged Particles with a Novel Type Toroidal Electrostatic Analyser," *Nuclear Instruments and Methods*, Vol. 195, pp. 581-586, April 15, 1982.
74. Carlson, C. W., Curtis, D. W., Paschmann, G., Michel, W., "An Instrument for Rapidly Measuring Plasma Distribution Functions with High Resolution," *Advances in Space Research*, Vol. 2, No. 7, pp. 67-70, 1983.
75. Choiniere, E., Gilchrist, B. E., "Measurement of Cross-Section Geometry Effects on Electron Collection to Long Probes in Mesosonic Flowing Plasmas," AIAA-2003-4950, 39th AIAA/ASME/SAE/ASEE Joint Propulsion Conference and Exhibit, Huntsville, AL, July 20-23, 2003.
76. Koehn, P., "The Development and Testing of the Fast Imaging Plasma Spectrometer and Its Application to the Plasma Environment at Mercury," Thesis, Dept. of Atmospheric and Space Sciences, University of Michigan, Ann Arbor, 2002.
77. Clemmons, J. H., Boehm, M. H., Paschmann, G., "Novel Measurement of the Pitch-Angle Structure of Auroral Electron Beams With a Top Hat Spectrometer," *Measurement Techniques in Space Plasmas: Particles*, R. F. Pfaff, J. E. Borovsky, and D. T. Young, eds., American Geophysical Union, Washington, DC, pp. 169-174, 1998.
78. Young, D. T., Bame, S. J., Thomsen, M. F., Martin, R. H., et al., "2- π Radian Field-of-View Toroidal Electrostatic Analyzer," *Review of Scientific Instruments*, Vol. 59, No. 5, pp. 743-751, May 1988.

79. Banks, B. A., Gaier, J. R., Hung, C.-C., Walters, P. A., et al., "Ultra High Voltage Propellant Isolators and Insulators for JIMO Ion Thrusters," AIAA-2004-3815, 40th AIAA/ASME/SAE/ASEE Joint Propulsion Conference & Exhibit, Ft. Lauderdale, FL, July 11-14th, 2004.
80. Gulczinski, F. S., "Examination of the Structure and Evolution of Ion Energy Properties of a 5 kW Class Laboratory Hall Effect Thruster at Various Operational Conditions," Ph.D. Thesis, Dept. of Aerospace Engineering, University of Michigan, Ann Arbor, MI, 1999.
81. Chen, F. F., *Introduction to Plasma Physics and Controlled Fusion*, Vol. 1: Plasma Physics, 2nd Ed., Plenum Press, New York City, NY, 1984.
82. Kruithof, A. A., "Townsend's Ionization Coefficients for Neon, Argon, Krypton and Xenon," *Physica*, Vol. 7, No. 6, pp. 519-540, June 1940.
83. Raizer, Y. P., *Gas Discharge Physics*, Springer-Verlag, Berlin, 1991.
84. Carlson, C. W., McFadden, J. P., "Design and Application of Imaging Plasma Instruments," *Measurement Techniques in Space Plasmas: Particles*, R. F. Pfaff, J. E. Borovsky, and D. T. Young, eds., American Geophysical Union, Washington, DC, pp. 125-140, 1998.
85. Gosling, J. T., Asbridge, J. R., Bame, S. J., Feldman, W. C., "Effects of Long Entrance Aperture Upon the Azimuthal Response of Spherical Section Electrostatic Analyzers," *Review of Scientific Instruments*, Vol. 49, No. 9, pp. 1260-1268, September 1978.
86. Dahl, D. A., *SIMION 3D Version 7.0 User's Manual*, Idaho National Engineering and Environmental Laboratory, Idaho Falls, ID, 2000.
87. Young, D. T., Bowman, R. P., Black, R. K., Booker, T. L., et al., "Miniaturized Optimized Smart Sensor (MOSS) for Space Plasma Diagnostics," *Measurement Techniques in Space Plasmas: Particles*, R. F. Pfaff, J. E. Borovsky, and D. T. Young, eds., American Geophysical Union, Washington, DC, pp. 313-338, 1998.
88. Crannell, C. J., Ormes, J. F., "Geometrical-Factor Determination Using a Monte Carlo Approach," *Nuclear Instruments and Methods*, Vol. 94, No. 1, pp. 179-183, June 15, 1971.
89. Sullivan, J. D., "Geometrical Factor and Directional Response of Single and Multi-Element Particle Telescopes," *Nuclear Instruments and Methods*, Vol. 95, No. 1, pp. 5-11, August 1, 1971.
90. Linder, D. R., Coates, A. J., Woodliffe, R. D., Alsop, C., et al., "The Cassini CAPS Electron Spectrometer," *Measurement Techniques in Space Plasmas: Particles*, R. F. Pfaff, J. E. Borovsky, and D. T. Young, eds., American Geophysical Union, Washington, DC, pp. 257-262, 1998.

91. Lin, R. P., Anderson, K. A., Ashford, S., Carlson, C., et al., "A Three-Dimensional Plasma and Energetic Particle Investigation for the Wind Spacecraft," *Space Science Reviews*, Vol. 71, pp. 125-153, February 1995.
92. Woodliffe, R. D., Johnstone, A. D., "The Use of Numerical Simulation in the Design of the Cluster/PEACE "Top Hat" Analyzer Electron Optics," *Measurement Techniques in Space Plasmas: Particles*, R. F. Pfaff, J. E. Borovsky, and D. T. Young, eds., American Geophysical Union, Washington, DC, pp. 263-267, 1998.
93. Norberg, O., Winningham, J. D., Lauche, H., Keith, W., et al., "The MEDUSA Electron and Ion Spectrometer and the PIA Ultraviolet Photometers on Astrid-2," *Annales Geophysicae*, Vol. 19, No. 6, pp. 593-600, November 6, 2001.
94. Dushman, S., *Scientific Foundations of Vacuum Technique*, Vol. 4, John Wiley & Sons, Inc., New York, NY, 1958.
95. Randolph, T., Kim, V., Kaufman, H., Kozubsky, K., et al., "Facility Effects on Stationary Plasma Thruster Testing," IEPC-93-093, 23rd International Electric Propulsion Conference, Seattle, WA, September 13-16, 1993.
96. Walker, M. L. R., "Effects on Facility Backpressure on the Performance and Plume of a Hall Thruster," Ph.D. Thesis, Dept. of Aerospace Engineering, University of Michigan, Ann Arbor, MI, 2005.
97. Haas, J. M., F. S. Gulczinski, I., Gallimore, A. D., Spanjers, G. G., et al., "Performance Characteristics of a 5 kW Laboratory Hall Thruster," AIAA-98-3503, 34th Joint Propulsion Conference and Exhibit, Cleveland, OH, July 12-15, 1998.
98. King, L. B., "Transport Property and Mass Spectral Measurements in the Plasma Exhaust Plume of a Hall-effect Space Propulsion System," Thesis, Dept. of Aerospace Engineering, University of Michigan, Ann Arbor, MI, 1998.
99. Beal, B. E., "Clustering of Hall Effect Thrusters for High-Power Electric Propulsion Applications," Ph.D. Thesis, Dept. of Aerospace Engineering, University of Michigan, Ann Arbor, MI, 2004.
100. Walker, M. L. R., "Effects of Facility Backpressure on the Performance and Plume of a Hall Thruster," Ph.D. Thesis, Dept. of Aerospace Engineering, University of Michigan, Ann Arbor, MI, 2005.
101. Hofer, R. R., Johnson, L. K., Goebel, D. M., Fitzgerald, D. J., "Effects of an Internally-Mounted Cathode on Hall Thruster Plume Properties," AIAA-2006-4482, 42nd AIAA/ASME/SAE/ASEE Joint Propulsion Conference & Exhibit, Sacramento, CA, July 9-12, 2006.

102. King, L. B., Gallimore, A. D., "Ion Energy Diagnostics in the Plume of an SPT-100 from Thrust Axis to Backflow Region," AIAA-98-3641, 34th AIAA/ASME/SAE/ASEE Joint Propulsion Conference and Exhibit, Cleveland, OH, July 13-15, 1998.
103. Peterson, P. Y., Gallimore, A. D., Haas, J. M., "Experimental Investigation of Hall Thruster Internal Magnetic Field Topography," AIAA-2001-3890, 37th AIAA/ASME/SAE/ASEE Joint Propulsion Conference & Exhibit, Salt Lake City, UT, July 8-11, 2001.
104. Kim, S.-W., Gallimore, A. D., "Plume Study of a 1.35 kW SPT-100 Using an ExB Probe," AIAA-99-2423, 35th AIAA/ASME/SAE/ASEE Joint Propulsion Conference, Los Angeles, CA, June 20-23, 1999.
105. King, L. B., Gallimore, A. D., "Mass Spectral Measurements in the Plume of an SPT-100 Hall Thruster," *Journal of Propulsion and Power*, Vol. 16, No. 6, November-December, 2000.